The Azimuthally Anisotropic Flow of Transverse Energy and Identified Protons and Charged Pions in 10.8 A·GeV/c Au + Au Collisions at AGS

A Dissertation Presented

by

Wen-Chen Chang

to

The Graduate School

in Partial Fulfillment of the Requirements

for the Degree of

Doctor of Philosophy

in

Physics

State University of New York
at
Stony Brook

May 1997

State University of New York
at Stony Brook

The Graduate School

Wen-Chen Chang

We, the dissertation committee for the above candidate for the Doctor of Philosophy degree, hereby recommend acceptance of the dissertation.

Johanna Stachel(advisor)
Professor of Physics

Gerald E. Brown
Professor of Physics

Thomas K. Hemmick
Associate Professor of Physics

Roy A. Lacey
Associate Professor of Chemistry

This dissertation is accepted by the Graduate School.

Graduate School

Abstract of the Dissertation

The Azimuthally Anisotropic Flow of Transverse Energy and Identified Protons and Charged Pions in 10.8 A·GeV/c Au + Au Collisions at AGS

by

Wen-Chen Chang

Doctor of Philosophy

in

Physics

State University of New York at Stony Brook

1997

The study of azimuthally anisotropic transverse flow in 10.8 A·GeV/c Au + Au collisions at the AGS, Brookhaven is presented. With the reconstruction of the reaction plane event by event, the flow signals of the transverse energy E_T and identified protons and charged pions are quantified by the Fourier moments of the azimuthal distribution with respect to the reaction plane. The Fourier moments charactering the anisotropic flow are studied as a function of rapidity(or pseudo-rapidity), transverse momentum, and centrality. The analysis shows that protons(or nucleons) exhibit a strong directed flow while pions collectively move in the opposite direction. A typical **S**-shaped distribution of the first moments (the directed flow) is observed in the rapidity space. The transverse momentum dependence of the first Fourier moment of protons suggests a picture of a transversely boosted thermal source for proton flow. We observe non-zero positive second Fourier moments charactering an elliptical event shape in the measurements of transverse energy and proton flow. This component, whose major axis is oriented in the reaction plane, is of a different orientation from the phenomena of "squeeze-out" as observed at lower energies. The centrality dependence of the azimuthally anisotropic flow consistently peaks at intermediate centralities and vanishes for very central and peripheral collisions. Comparisons with cascade models show the need to introduce either a mean filed potential for nucleons in RQMD or a energy-dependent repulsive scattering in ARC.

To my dear parents
for their caring and love...

Contents

List of Figures

List of Tables

Acknowledgements

Praise God for His love and faithfulness in giving me a dedicated period of five years and so many supportive people around. Other than the completion of the work in this thesis, I reassured myself that Jesus Christ is my savior and have an increasingly close relationship with Him.

I thank my parents, my elder brother Wen-Chien and my dear wife Ling-Hui for their constant love and support. I love you and my son Jonathan so much. The brothers and sisters in the fellowship and church, who help me go through each moment of depression and nervousness by praying for me, definitely deserve my sincere appreciation.

I am deeply indebted to my thesis advisor Johanna, Sergei Voloshin and Yingchao for their instructions in finishing up the content of my thesis. I cherish the friendship with members in E877 collaboration and thank you for help, especially Peter, Tom, Nu, Martin, Hannes, Dariusz, Rich Hutter, Byunsik, Chuan-Ming, Sergei Panitkin, Tim, Thongbay, Mark, Steph, Rich Bersch and Vlad.

Chapter 1

Introduction

Nuclear physics deals with a many body problem where the number of particles involved is much less than 10^{23} but much more than one. Heavy ion physics accessible by colliding two nuclei provides us with a unique testing ground to understand whether macroscopic and statistical concepts like temperature, energy density, entropy, chemical potential and equilibrium could be applied to nuclear systems. In other words, the so called "equation of state" (EOS) or the thermodynamics of excited nuclear matter, which characterizes the system, may be explored. Current knowledge of the EOS is restricted to a narrow region around the ground state through study of the giant monopole resonance. Ultra-relativistic heavy ion collisions, with C.M. energy per nucleon pair ($\sqrt{s}$) above 5 GeV and using heavy targets and projectiles, can extend this frontier to include systems of much higher baryon densities and excitation energy. They are a unique tool for providing insight into two of the most fundamental and important questions of QCD (Quantum Chromodynamics) vacuum structure: quark confinement and chiral symmetry breaking.

Ultra-relativistic heavy ion collisions [1, 2, 3, 4, 5, 6, 7, 8, 9] create hadronic matter with very high energy and baryon density. This highly excited system can possibly undergo a phase transition into an entirely new phase, quark-gluon-plasma (QGP), where the partons (quarks and gluons) confined in normal nuclear matter are liberated and become the relevant degrees of freedom over a macroscopic volume. On the other hand, the apparently broken chiral symmetry, manifested itself in large effective quark masses ($m_u \approx m_d \approx$ 300 MeV, $m_s \approx$ 500 MeV) at low energy density, is predicted to be largely restored with very small current quark masses ($m_u \approx m_d \approx$ 5 MeV, $m_s \approx$ 150 MeV). This state is the true perturbative vacuum of QCD where physics can been understood from the first principles of thermodynamics and QCD.

The space-time evolution of ultra-relativistic heavy ion collisions can be characterized by four stages: compression and heating, equilibration, expansion and cooling, and freeze out.

At the beginning of the reaction, two highly Lorentz-contracted nuclei collide. The longitudinal beam momentum compresses the collision zone into a region of high baryon density (at least in the present fixed target experiments) and inelastic nucleon-nucleon interactions redistribute the highly directional beam energy into other degrees of freedom, like the production of transverse momenta, thermal energy and entropy. The effectiveness of transforming beam energy into compression and heating of the participants is called "stopping power".

After a short time of about the order of 1 fm/c, the highly excited and interacting zone may reach thermal and chemical equilibrium and pass beyond the phase boundary to the state of an equilibrated QGP. Then the whole system will expand outward into the vacuum, mainly along the longitudinal direction, and cool until reaching the critical transition temperature T_c after a few fm/c. The matter then stays in the mixed phase where hadronization of the QGP takes places. In particular, if the phase transition is of first order, the lifetime of the mixed phase is expected to be long (on the order of 10 fm/c).

Finally the system returns to a strongly interacting hadronic gas and expands to such a large volume that all particles "freeze-out". Through all stages the particles "freeze-out" when their mean free path is larger than the radius of the system, and stream away to the detectors.

There are various proposed signatures to detect the possible formation of QGP in the collision. They can be categorized into two kinds of probes on various aspects of physics [11, 12]:

Probe

1. **Penetrating Probe**: particles with electro-magnetic interactions. The small interaction cross section with the medium makes it a clean and valuable tool for revealing information of the earliest and hottest stage of the evolution of the fireball. The disadvantage is the relatively small yield and large hadronic background.

   - Dilepton pair ($\eta, \rho, \omega, \phi, J/\psi \rightarrow l^+ \, l^-$)
   - Direct photon (γ)

2. **Hadronic and Strangeness Probes**: streaming out after strong or weak interactions cease. These are much more abundant particles produced and good probes for understanding thermalization, chemical equilibrium and collective motion. The final-state interaction may smear out the physics at earlier stages.

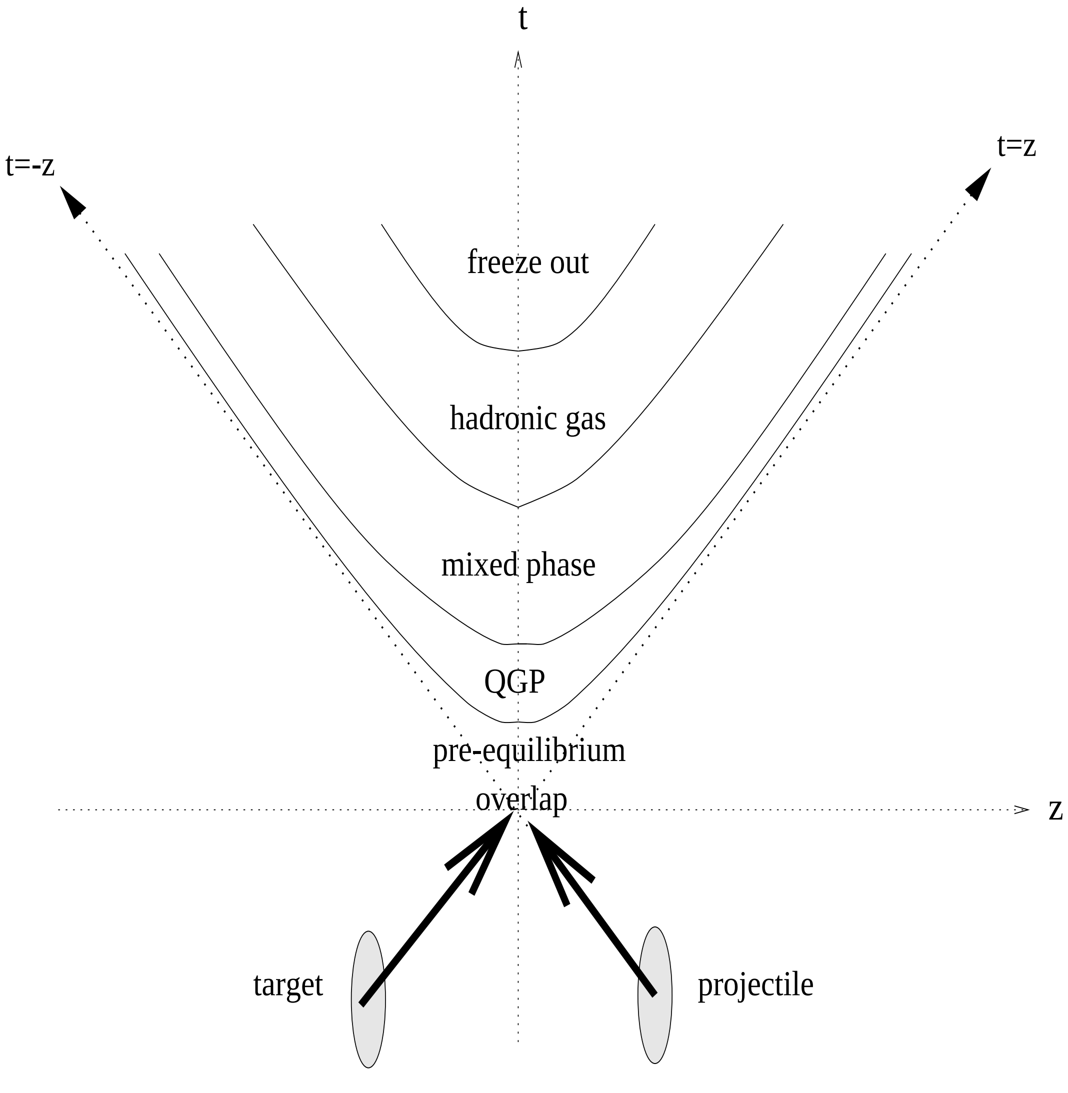

Figure 1.1: A schematic space-time history of the AA collisions in the CM system

- Nucleons (p, n, Δ, $\bar{\text{p}}$) and pions (π)
- Strange particles (K, Λ, Σ, Ξ, Ω, dibaryon H)

Aspects of Physics

1. **Thermodynamics**: transverse momentum(p_t) spectra (thermal equilibrium) and particle ratios (chemical equilibrium).
2. **Collective effects**: isotropic and anisotropic expansion.
3. **Medium effects**: modification of interaction cross section and effective mass in the nuclear medium.
4. **Size and Lifetime**: interferometry of identical or unlike particles.

All these signatures can be studied systematically as a function of the following global variables:

1. **Centrality**: collisions with different impact parameters.
2. **Beam Energy**: excitation function of signatures.
3. **Mass Number**: combination of target and projectile nuclei.
4. **Reaction Plane Orientation**: physics observed relative to the reaction plane.

Because of the small volume and short lifetime of a possible QGP and the final hadronization in the latest stage, no single proposed signature is proven to be sufficient evidence of the existence of a QGP phase. However, a complete and systematic measurement of many signatures over various dependences may provide a converging and convincing picture of nature. Any deviation from the results of a purely hadronic gas picture will be a hint of the occurrence of a QGP or new physics.

The experimental efforts started in 1978 at the BEVALAC (at Lawrence Berkeley Laboratory) and are currently being pursued from intermediate energies around a hundred MeV per nucleon (NSCL, Michigan State University and GANIL) to relativistic energies around 1 GeV per nucleon (SIS at GSI, Darmstadt) to ultra-relativistic energies (BNL AGS [10], 15 GeV/c per nucleon and CERN SPS, 200 GeV/c per nucleon). A nice review of the experiments both at AGS and SPS can be found in Ref. [13].

The experiments at the AGS show large baryon stopping in the collisions and thus effectively lead to the formation of dense hadronic matter. This thesis will focus on the signal of anisotropic flow of nucleons and pions for Au+Au nuclei colliding with beam momentum of 10.8 GeV/c per nucleon measured for different centralities by experiment E877 at the Brookhaven AGS. There will be a discussion of the physics background concerning this signature in Chapter 2. A brief introduction of the experimental setup is given in Chapter 3. A general overview of the strategy of the flow analysis is discussed in Chapter 4. In Chapter 5 the results of flow signals in transverse energy(E_T) are shown. By studying the difference between the measurements of transverse energy E_T and charged particle multiplicity(N_{ch}), the nucleon and pion flow can be disentangled around the mid-pseudorapidity region; those results are described in Chapter 6. Using the particle identification in the spectrometer, the flow properties of protons and charged pions are analyzed and results are given in Chapter 7

Conclusions and remarks will be made in the last chapter. However, I would like to emphasize that this work is just "a tiny piece of a big puzzle", not to be mistaken for a comprehensive description. Much more work is needed to develop a deep and full understanding of the underlying physics.

Chapter 2

The Physics of Collective Flow

2.1 Introduction

As was stated in the previous chapter, the primary goal of ultra-relativistic heavy ion collisions carried out at AGS and CERN is to further the understanding of the properties of hot and dense hadronic matter and to detect any signals for chiral symmetry restoration and the formation of a quark-gluon-plasma (QGP). Based on the currently available measurements, the system formed in heavy ion collisions at the AGS is found to be consistent with the picture of a thermal fireball with decoupled longitudinal and transverse expansions [14]. Because of the strong final-state interactions before freeze-out, which lead to thermalization, most of the physical information during the earlier stage of the collisions, when the highest baryon and energy densities are reached, is likely to be smeared out. However, the measurement of collective motion driven by the pressure gradient provides a diagnostic tool to study the transient pressure built up through all the stages of compression, heating and subsequent expansion.

It was first predicted using hydrodynamics [15] that the development of compressional shock waves would lead to collective flow phenomena like sideward deflection of matter in the reaction plane("side-splash" of the participants and "bounce-off" of the spectator) and an elliptical event shape with the major axis perpendicular to the reaction plane ("squeeze out" of participant at mid-rapidity). These predictions of collective flow effects received a experimental confirmation at the BEVALAC [16]. Through the conversion of thermal and compressional energy into macroscopic collective motion (flow) [17], the flow signals are also predicted to be a good probe to study the dependence of energy density ϵ , pressure P, and entropy density s, on temperature T and baryochemical potential μ_b , which is the "equation of state" (EOS).

There are two different patterns of collective flow in the transverse direction to be distinguished, "isotropic radial flow" and "azimuthally anisotropic flow". Even though there is a tempting explanation of the "squeeze-out" emission ("azimuthally anisotropic flow") by in-plane retardation of radial expansion [20] ("isotropic radial flow"), the deep connection between these two phenomena is still not understood. We will briefly discuss the progress made in understanding them in the following two sections. In the final section, we take a more macroscopic view and see what we can learn from the excitation function of flow signals.

2.2 Radial Flow

Isotropic radial flow was suggested as evidence for a blast wave from compressed nuclear matter which converts the isotropic thermal energy into a radially ordered expansion [17]: all species of particles are pushed outward by a common velocity. A straight-forward observation is the appearance of a "shoulder arm" in the p_t spectrum which results from the "soft"(low p_t) thermal energy moving into the "hard"(high p_t) collective energy component. One result is that the inverse slope parameter (T_B) fitted to the high p_t tail of the spectra is larger than the temperature of the thermal source (T) and the spectra of particles of larger mass exhibit larger values of T_B.

A static isotropic thermal source of temperature T characterized by the Maxwell-Boltzmann distribution emits particles of mass m with transverse momentum spectrum p_t at rapidity y according to,

$$E\frac{d^3N}{d^3p} \propto E\exp(-\frac{E}{T}) \tag{2.1}$$

$$= (m_t\cosh(y))\exp(-\frac{m_t\cosh(y)}{T}) \tag{2.2}$$

where $m_t = \sqrt{m^2+p_t^2}$ is the transverse mass.

If particles are emitted from the shell of a three dimensional(3-d) fireball which expands azimuthally symmetric with uniform velocity $\beta_t(r)$ [17], the relativistic transverse momentum spectrum is,

$$\frac{d^2N}{m_t dm_t dy} \propto (m_t\cosh(y))\exp(-\frac{\gamma m_t\cosh(y)}{T})\cdot [\frac{\sinh(\alpha)}{\alpha}(\gamma+\frac{T}{m_t\cosh(y)})-\frac{T}{m_t\cosh(y)}], \tag{2.3}$$

where

$$\gamma = \frac{1}{\sqrt{1-\beta_t^2}}$$
$$\alpha = \frac{\beta_t \gamma p}{T}$$

In ultra-relativistic heavy ion collisions, longitudinal and transverse expansion are most likely decoupled as schematically shown in Fig. 2.1. Then the expansion in the transverse direction is reduced to two dimensional(2-d) one, and the transverse spectrum is described by [23],

$$\frac{d^2N}{m_t dm_t dy} \propto m_t I_0(\frac{p_t \sinh(\varrho)}{T}) K_1(\frac{m_t \cosh(\varrho)}{T}), \tag{2.4}$$

where

$$I_0, K_1 \quad : \quad \text{Modified Bessel functions}$$
$$\varrho = \tanh^{-1}(\beta_t)$$

The transverse mass spectra of protons at mid-rapidity, taking into account the radial flow effect emitted from a shell of fixed radius of an isotropic 3-d and 2-d expansion, is plotted in Fig. 2.2. To get a complete spectra, a velocity profile as a function of the radius of fireball ($\beta_t(r)$) must be assumed for these two models and then integrated over the radius r.

It has been demonstrated [14, 19] that the observed mid-rapidity transverse spectra at BEVALAC, AGS, and SPS are better described by taking into account this collective component instead of a purely static thermal source. At BEVALAC energies, the first parameterization from a 3-d shock wave fit the data with $\langle\beta_t/c\rangle$=0.3 and T=0.075 GeV [19]. For the experiments above and including AGS energies, the large longitudinal expansion makes the decoupled transverse expansion describe the data better. The best fitted values are $\langle\beta_t/c\rangle$(radius-averaged velocity)=0.39-0.33 and T=0.12-0.14 GeV for Si+Pb(Au) at AGS and $\langle\beta_t/c\rangle$=0.27 and T=0.16-0.17 GeV for S+Pb at SPS [14]. The different schemes used in the fitting makes the extracted value of radial flow rather model-dependent. It should also be noted that the fitted radial flow velocity β_t is correlated with the fitted temperature T and might depend on the velocity profile ($\beta_t(r)$) assumed.

The centrality dependence of this flow signal characterized by the expansion velocity β_t is expected to be strongest for the most central collisions where greatest pressure is built up and weakest towards the peripheral end. It

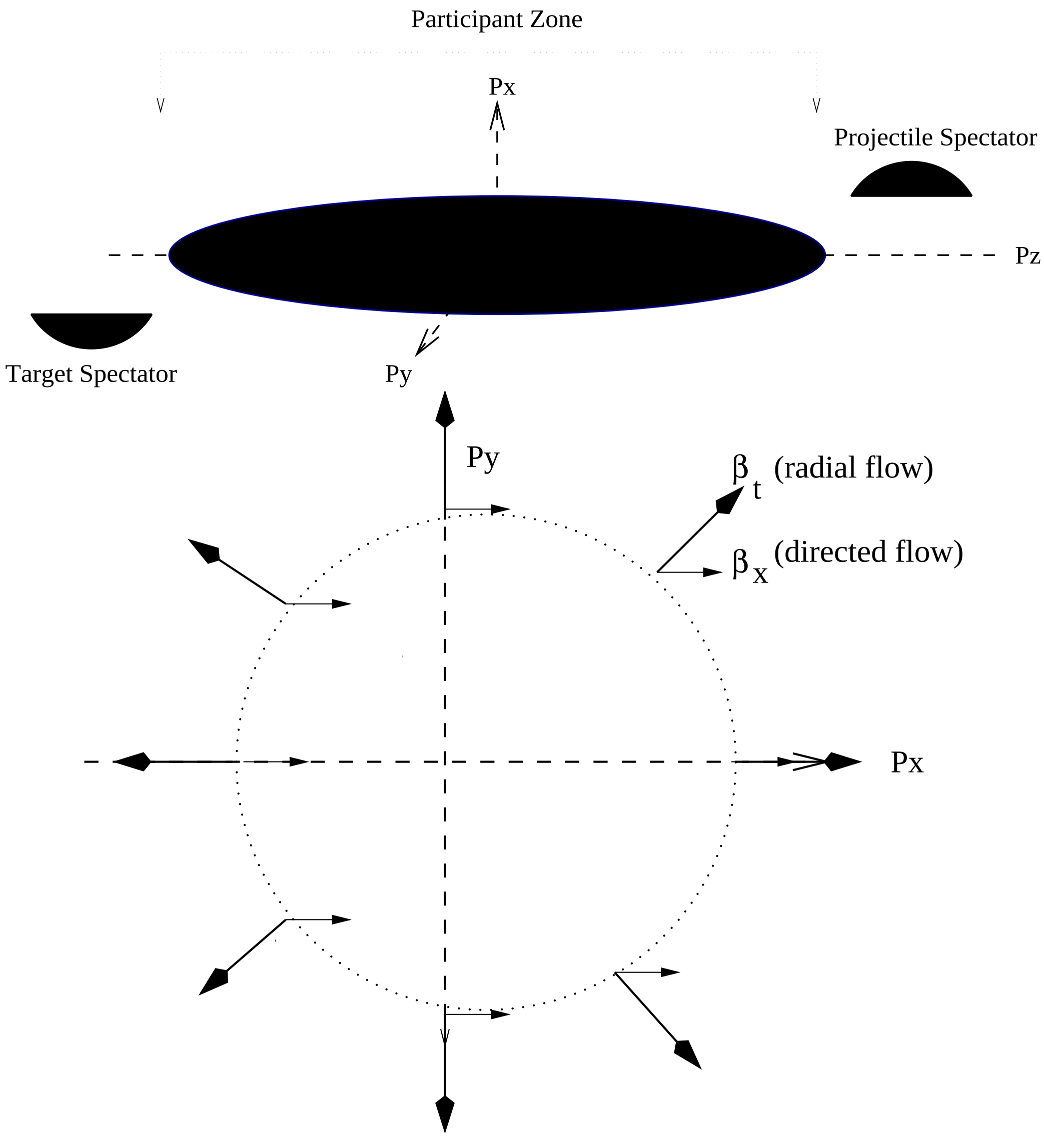

Figure 2.1: A schematic plot of the decoupled longitudinal and transverse expansion in ultra-relativistic heavy ion collisions. There are two components in the transverse expansion: isotropic and anisotropic flow. The x axis is defined as the direction of the impact parameter vector($\vec{b}$).

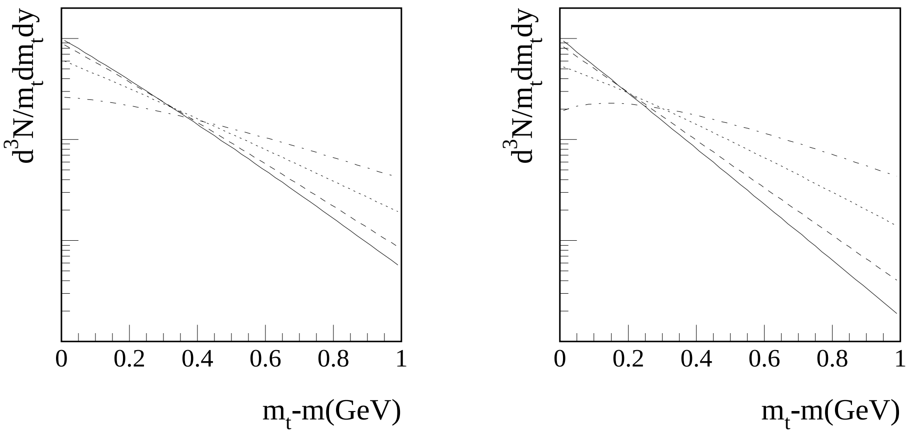

Figure 2.2: The transverse mass ($m_t = \sqrt{m^2 + p_t^2}$) spectra of protons at mid-rapidity taking into account the radial flow effect in an isotropic 3-d (left figure) and 2-d (right figure) expansion from a thermal source with T=0.15 GeV. The different curves correspond to different flow velocities β_t/c = 0(solid), 0.2(dashed), 0.4(dotted) and 0.6(dotted-dashed). Without the flow effect, the high m_t tail scales as $m_t \exp(-m_t/T)$ in the 3-d expansion and as $\sqrt{m_t} \exp(-m_t/T)$ in the case of 2-d expansion.

is quite natural to expect that this collective phenomenon carries information about the most violent collisions, where QGP is most likely to be produced, and changes of the equation of state occur. However, quite unexpectedly, at BEVALAC energies, it is shown that the radial flow signal possesses little sensitivity to the microscopic details of the transport model calculations (QMD, BUU) like nuclear compressibility and the in-medium modification of the nucleon-nucleon cross section [19, 24]. One possible explanation is that the sensitivity of this azimuthally averaged (or symmetric) part of collective motion to the EOS is weakened when thermal equilibrium is more likely reached in the most central collision and thermal pressure, instead of the pressure generated from baryon gradient, is dominating through all stages. However, there is still no fundamental understanding of this question.

2.3 Azimuthally Anisotropic Flow

The collective flow driven by the pressure gradient produces the effect of space-momentum correlations and transforms the initial azimuthal asymmetry of the colliding geometry into an asymmetry in the final transverse momentum distribution. The azimuthally anisotropic flow reaches its maximum at mid-central events and vanishes toward central and peripheral collisions.

The experimental observations of “directed flow” and “squeeze out” are well established at the BEVALAC [16], and SIS [21, 22] energies ($\sqrt{s} \approx$ 1 GeV) using the traditional methods of thrust [25], 3-d sphericity [26, 27, 28] and the most widely used transverse momentum analysis [29]. However, the requirement in these methods like large acceptance with full azimuthal coverage and momentum measurements of all tracks prohibits their application to analysis at higher energies and the experiments without the detectors like time projection chambers(TPC).

Following the original work of 2-d sphericity analysis by Ollitrault [30], a generalized method of Fourier expansion [34] on the azimuthal distribution of transverse energy measured by calorimetry was developed and used in the E877 analysis to discover side-ward collective flow in Au + Au collisions at the AGS [31]. This is the first evidence to show that this collective behavior still persists at ultra-relativistic energies. The resulting observation by E877 is a nonzero first and second moment of the azimuthal distributions. The first moment represents the directed transverse flow which can also be utilized to reconstruct the reaction plane and the positive second moment reflects an elliptical event shape with the major axis in the direction of the reaction plane which is perpendicular to the “squeeze out” measured around 1 GeV energies.

At higher collision energies, an elliptical transverse energy flow at mid-pseudo-rapidity for Pb+Pb at SPS has been reported by NA49 [37]. However the orientation of the major axis is not known yet because of a lack of ability to determine the reaction plane. In this thesis, we continue the flow analysis at AGS by studying the physics observables with respect to the reconstructed reaction plane and examining detailed flow signals of transverse energy and identified protons and pions [32, 33].

2.4 Excitation Function of Radial Flow and Directed Flow

A first-order phase transition between a hadronic gas and a quark-gluon plasma can be revealed by a drastic softening in the equation of state where more thermal energy is consumed in latent heat and the ratio of internal pressure to energy density is thus reduced. It has been predicted that a "softest point" in the equation of state, where the ratio of pressure to energy density is smallest [43], can be deduced from systematic experimental measurements through different beam energies and the observation a minimum in the flow signals [42, 44] or a maximum in the life time of the fireball [45].

There are experiments(e.g. E895, E910, and E917 etc) and theoretical calculations to map the excitation function of flow under way. Especially the E895 collaboration [46], running at intermediate AGS energies(4-8 GeV), is important in filling the gap of the excitation function between BEVALAC and AGS.

The experimental values of radial flow show an increase scaling proportional to $\log(E_{beam})$ up to about 2 GeV and saturate up to AGS energies. QMD and BUU model calculations show that the signal below 2 GeV has no dependence on the nuclear equation of state, within the sensitivity of experimental measurements [19, 24]. Models like ART [40] and URQMD [48] have similar predictions about the insensitivity of the excitation function of radial flow to any extra potential beyond the pure cascade calculations.

As for the directed flow signal, all of the model calculations show a significant dependence on the choice of EOS, making this experimental measurement very important. The maximum magnitude of $\langle p_x \rangle (y)$ has a saturation curve similar to that of radial flow, both in experimental observation [16, 32, 46] and the ARC model calculation [38]. The derivative of the flow curve at mid-rapidity has a gradual drop after 2 GeV. Part of the reason for this drop is the trivial increase of rapidity range because of higher beam momentum. But any change other than this kinematic factor can be interpreted as a variation of the EOS. The definition of directed flow used in the hydro-dynamical calculation [44] shows a "softest" point around 6 GeV with a QGP phase transition where the expansion of the collision zone is delayed by a lack of internal pressure. The experimental observation of this minimum of the excitation function would be a qualitative signal for a phase transition to QGP phase in the nuclear matter.

Finally, there is one newly proposed definition of flow: the second moment of the azimuthal distribution at mid-rapidity [39]. Since the experimental observation of the orientation of the elliptical flow changes from out-of-plane (negative second moment) at BEVALAC to in-plane (a positive second moment) at AGS (see Chapter 5), this flow signal should have a qualitative change between these two beam energies. A complete measurement of the excitation function of this signal will help us understand the strength of the early pressure and how fast it develops and further the interplay of the expansion of participants with the removal of spectators as a function of beam energy.

Chapter 3

Experimental Setup and Data Selection

3.1 Experiment E877 at AGS

As the extension of Experiment E814, Experiment E877 is a fixed target experiment at the BNL AGS for studies of the hot and dense nuclear matter produced in central collisions of 10.8 A$\times$GeV/c Au ion projectiles on nuclear targets. A schematic view of the experimental setup is depicted in Fig. 3.1. The detector system can be grouped into three subunits:

Beam definition:	BSCI, BVER, SILI
Event characterization:	TCAL, MULT, PCAL, UCAL
Particle Identification:	DC2, DC3, MWPC, TOFU, FSCI

With nearly 4π calorimeter coverage around the target, transverse energy measurements are used for global event characterizations of centrality and the determination of the reaction plane determination, a unique characteristic of E877 in the experiments at AGS. The downstream forward spectrometer provides the tracking and time-of-flight measurements of charged particles for use in particle identification. The acceptance of the spectrometer covers primarily the forward rapidities and low p_t regions(See Fig. D.2).

We will briefly give an introduction to each detector. Detailed descriptions of these detectors can be found in earlier PhD theses and publications from the E814/E877 collaboration [49, 50, 51, 52, 53, 54, 55, 56, 58].

3.1.1 Detectors for Beam definition

Beam counters (BSCI): Four plastic scintillator counters, labeled as S1, S2, S3 and S4, are used to define a counted valid beam particle by the logic of $\bar{S1} \times S2 \times \bar{S3} \times S4$ because S1 and S3 are beam veto with a hole. The signal

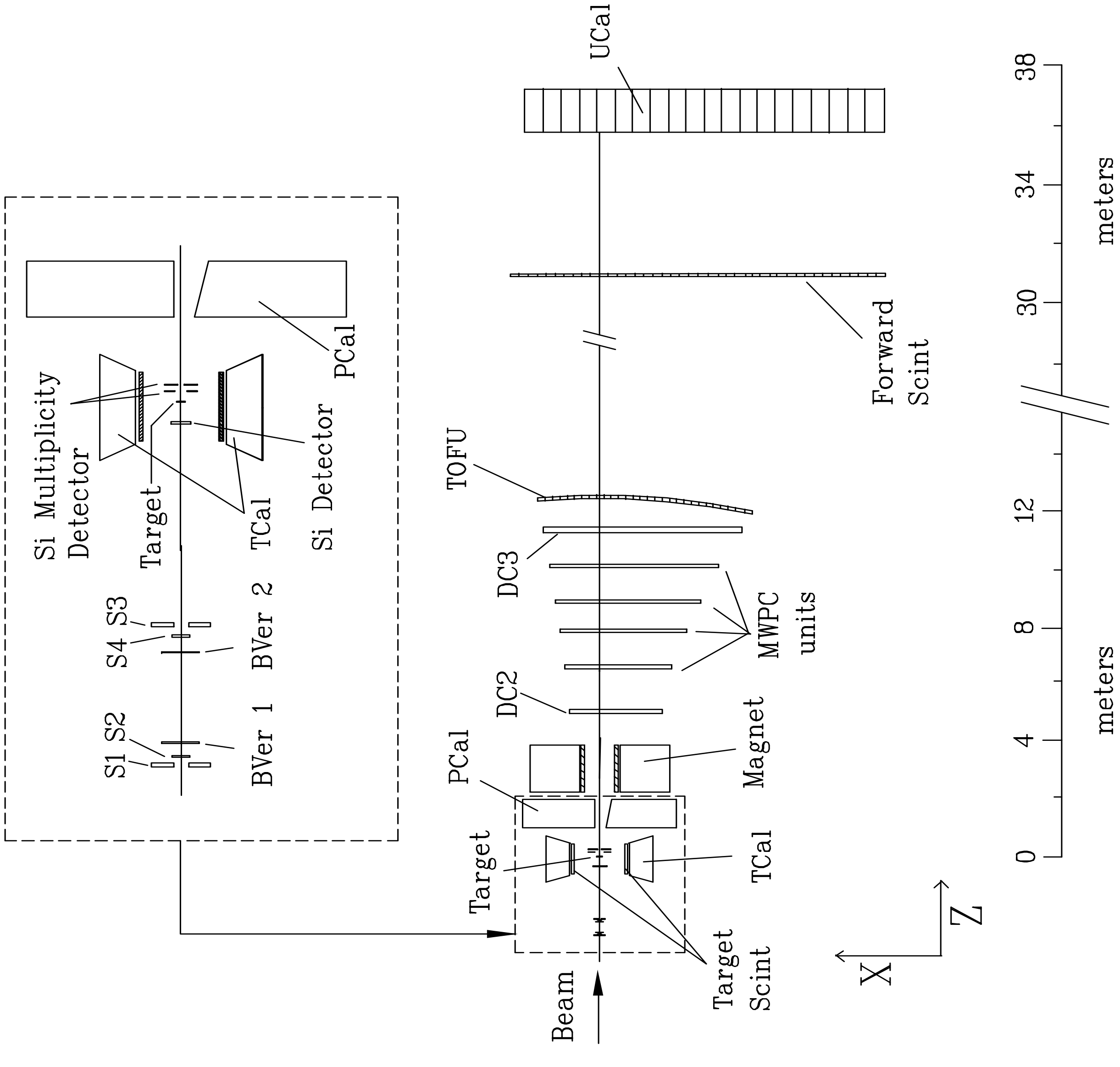

Figure 3.1: E877 setup for the 1993 run

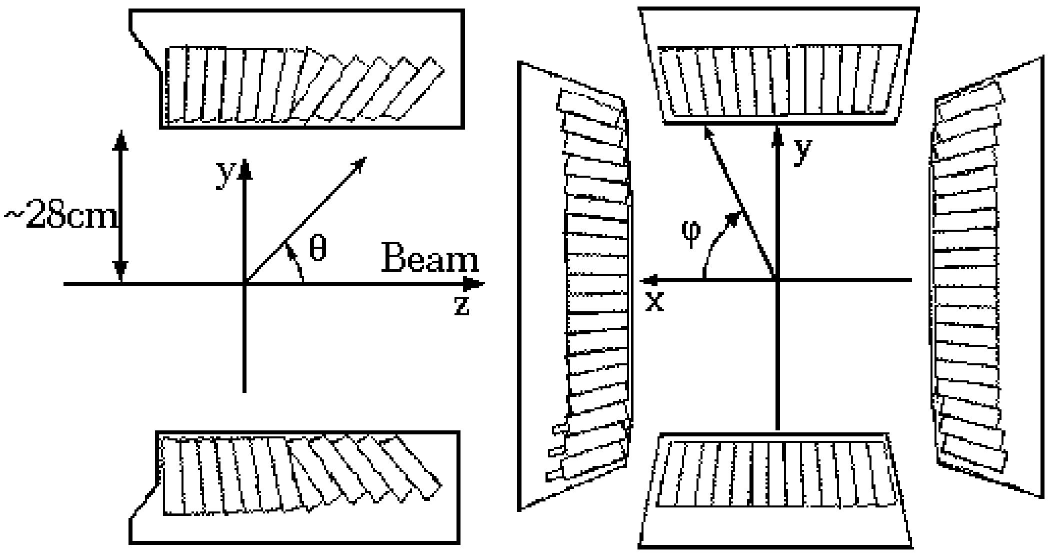

Figure 3.2: The side view (left) and end view (right) of TCAL.

on S4 provides the start time (T_0) with 35 ps resolution for the time-of-flight measurement.

Beam vertex detectors (BVER): Two silicon micro-strip detectors located between S2 and S4 are used to measure the horizontal position of the beam particle and the horizontal incident beam angle at the target position by extrapolation. It achieves a resolution of the horizontal beam position at the target of about 50 μm and the beam angle about 40 μrad.

Upstream silicon detector (SILI): A silicon semiconductor detector is placed immediately before the target and measures dE/dx of the charged particles passing through it. The measurements serve as a criterion to select beam particles with correct charge and reject any upstream interactions before the target.

3.1.2 Detectors for Event Characterization

Target calorimeter (TCAL): A calorimeter made of 832 NaI crystals with a depth of 13.8 cm, corresponding to about 5.4 radiation lengths or 0.34 hadronic interaction length, is used to measure the transverse energy (E_T) with 2π azimuthal coverage in the region of about $48° < \theta < 135°$ in polar angle and $-0.5 < \eta < 0.8$ in pseudo-rapidity. The side and end view of TCAL is shown in Fig. 3.2.

Silicon multiplicity detector (MULT): Two disks of 300 μm thick silicon of 3 inches radius segmented into 512 nearly-square pads in η and ϕ space, measure the multiplicity of charged particles over a pseudo-rapidity region $0.87 < \eta < 2.46$.

Participant calorimeter (PCAL): PCAL is a lead/iron/scintillator sampling calorimeter for measuring the transverse energy in the polar angular region $1° < \theta < 47°$, corresponding to the pseudo-rapidity range $0.83 < \eta < 4.7$, with a depth of four hadronic interaction lengths and full azimuthal coverage. It is segmented laterally into 8 radial and 16 azimuthal elements and longitudinally into 4 depth layers labeled as EM1, EM2, HD1 and HD2. The various views from the front and the lateral and the quadrant definition are shown in Fig. 3.3, 3.4.

Uranium calorimeter (UCAL): UCAL is a sampling calorimeter with uranium and iron plates as absorbers interleaved with scintillators for a total depth of about 6 interaction lengths. It is positioned furthest from the target at a distance of 35 m. It is used to measure the energy of forward particles("zero degree calorimeter"), especially neutrons, with a resolution of about $\Delta E/E \simeq 50\%/\sqrt{E}$.

In Fig. 3.5, the measurements of E_T in two calorimeters TCAL and PCAL show a strong correlation as expected; both of them provide measurements of the violence of the collision and thus define the centrality of the collisions. Fig. 3.6 is the measured distribution of $d\sigma/dE_T$. We define the centrality cut in E877 by calculating the ratio of the integral from a given E_T^0 to the top end of distribution to the geometric cross section(σ_0) [13].

The interaction probability (P_{inter}) of a good beam coming into the target of geometrical cross section σ_0 and the thickness δ_T and density ρ_T is,

$$P_{inter} = \rho_T \cdot \delta_T \cdot \sigma_0 \tag{3.1}$$

so that the complete distribution of $d\sigma/dE_T$ is constructed by taking into account the trigger down-scale factor ($DS \geq 1$), the number of defined beams (B), and the interaction probability (P_{inter}),

$$\frac{d\sigma}{dE_t} = DS\ \sigma_0 \frac{d(N_{event}/(BP_{inter}))}{dE_t}. \tag{3.2}$$

The centrality cut of events with $E_T > E_T^0$ corresponds to the selection of events with the most central interaction cross section (σ_{top}) as

$$\sigma_{top} = \int_{E_T=E_T^0}^{\infty} \frac{d\sigma}{dE_t} dE_t. \tag{3.3}$$

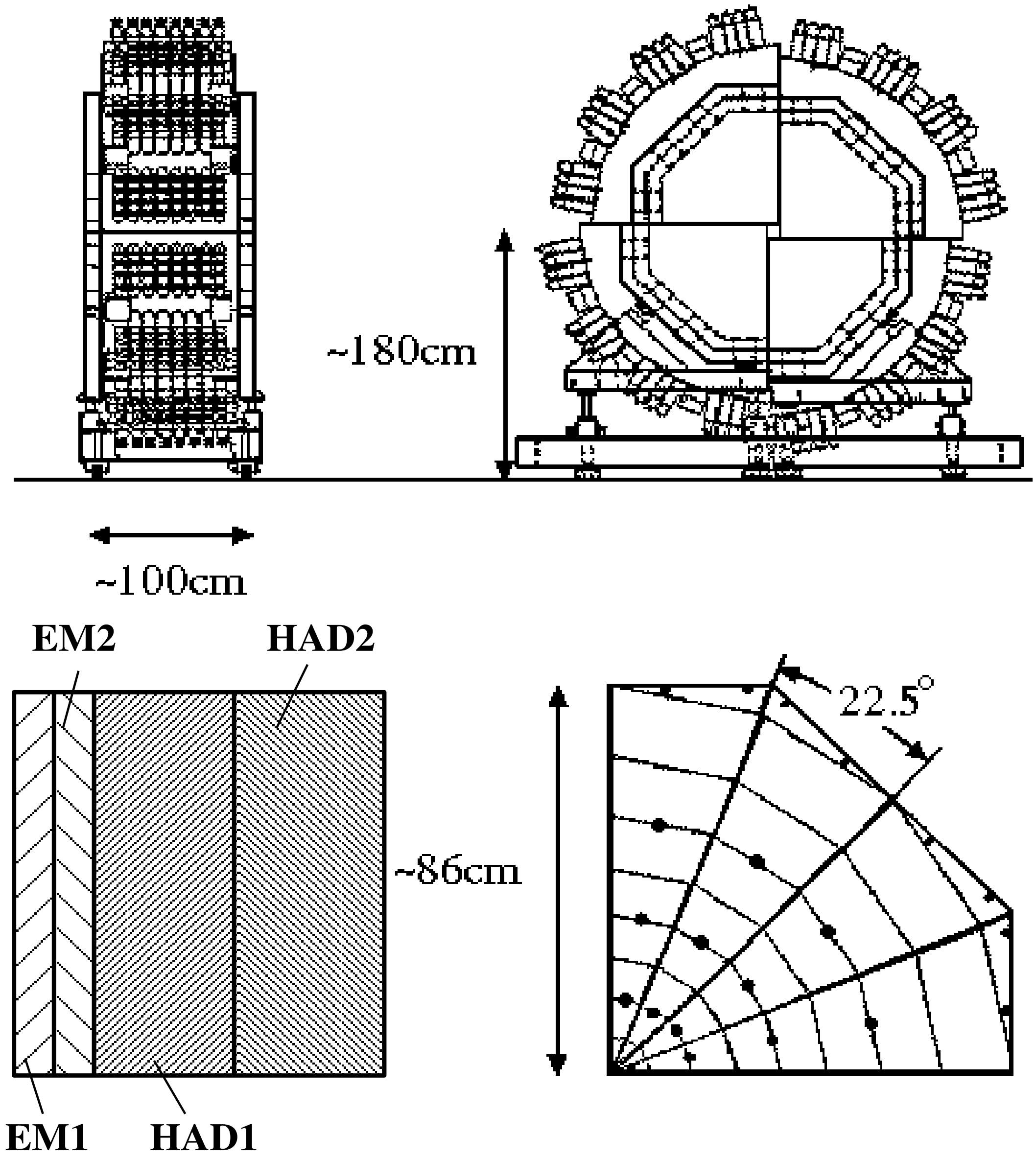

Figure 3.3: The side view (upper-left) and end view (upper-right) of PCAL, and its schematic longitudinal (lower-left) and lateral (lower-right) segmentations.

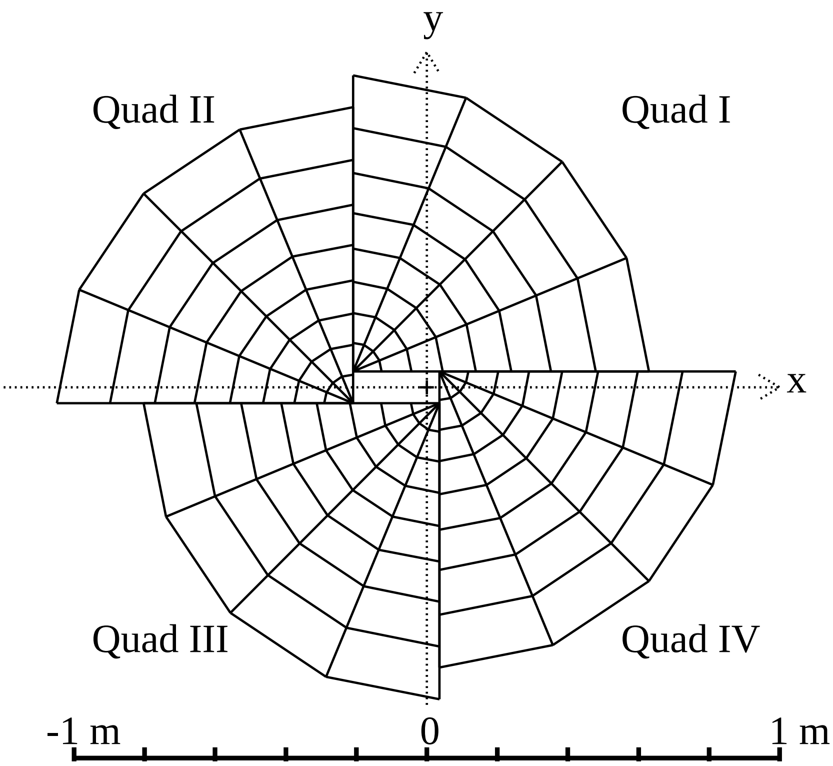

Figure 3.4: The view of PCAL from downstream in the defined lab coordinate.

The ratio of σ_{top} to the geometrical cross section σ_0 characterizes the centrality of the collision and is independent of the absolute value of σ_0. This definition can be used by different experiments so that results belonging to the same centrality cut can be compared.

Both TCAL E_T and PCAL E_T are used in the analysis and Fig. 3.7 shows the corresponding centrality for the cut of E_T^0 made on the measured E_T of both TCAL and PCAL. Due to the acceptance and energy leakage, TCAL has larger fluctuations in E_T for a given impact parameter. Therefore E_T measured by PCAL is a more sensitive quantity in selecting the most central events [55].

3.1.3 Detectors for Particle Identification

Drift chamber (DC2,3): Each drift chamber has six wire planes for horizontal position(x) measurement and one pad plane for vertical position(y) of the particles. The resolution in the x position of minimum ionizing particles is approximately 250(300) μm for DC2(DC3). Three different density regions are distinguished in the pad planes, and the associated y position resolutions of DC2(DC3) are estimated to be 2.3, 5.1 and 15.0 mm (0.3, 7.0 and 36.0 mm) for fine, medium and coarse regions. The momentum resolution is dominated by the multiple scattering and is estimated as $\delta p/p \approx 3.6\%/\beta$ for Au beam.

Multi-wire proportional chamber (MWPC1,2,3,4): The wire plane in each chamber provides the measurements of horizontal position(x) and is used for track confirmation in the tracking algorithm.

Time of flight upstream wall (TOFU): Composed of an array of 160 plastic scintillator rods aligned vertically, TOFU produces the "STOP" signal for charged particle time of flight measurements with about 85 ps resolution. The difference of arriving times in top and bottom photo tubes can be used to as an estimate of the vertical position.

Forward scintillator (FSCI): A scintillator hodoscope wall measures time of flight with 350 ps resolution. It is particularly useful for detecting anti-protons because the background from negative kaons, which decay before FSCI, will be significantly reduced.

The acceptance of the forward spectrometer is defined by the iron wedges, called the "collimator", stacked inside the central hole of the PCAL. The main acceptance of the spectrometer sits on the $-x$ horizontal side of our defined lab coordinate. A dipole magnet is placed behind the collimator and two different field configurations are set along the vertical axis: in "A" polarity positive tracks are bent toward the $+x$ direction and away from the acceptance of the spectrometer, while in "B" polarity the bending direction is opposite. The opening of the collimator is set to be smaller than the projective opening of

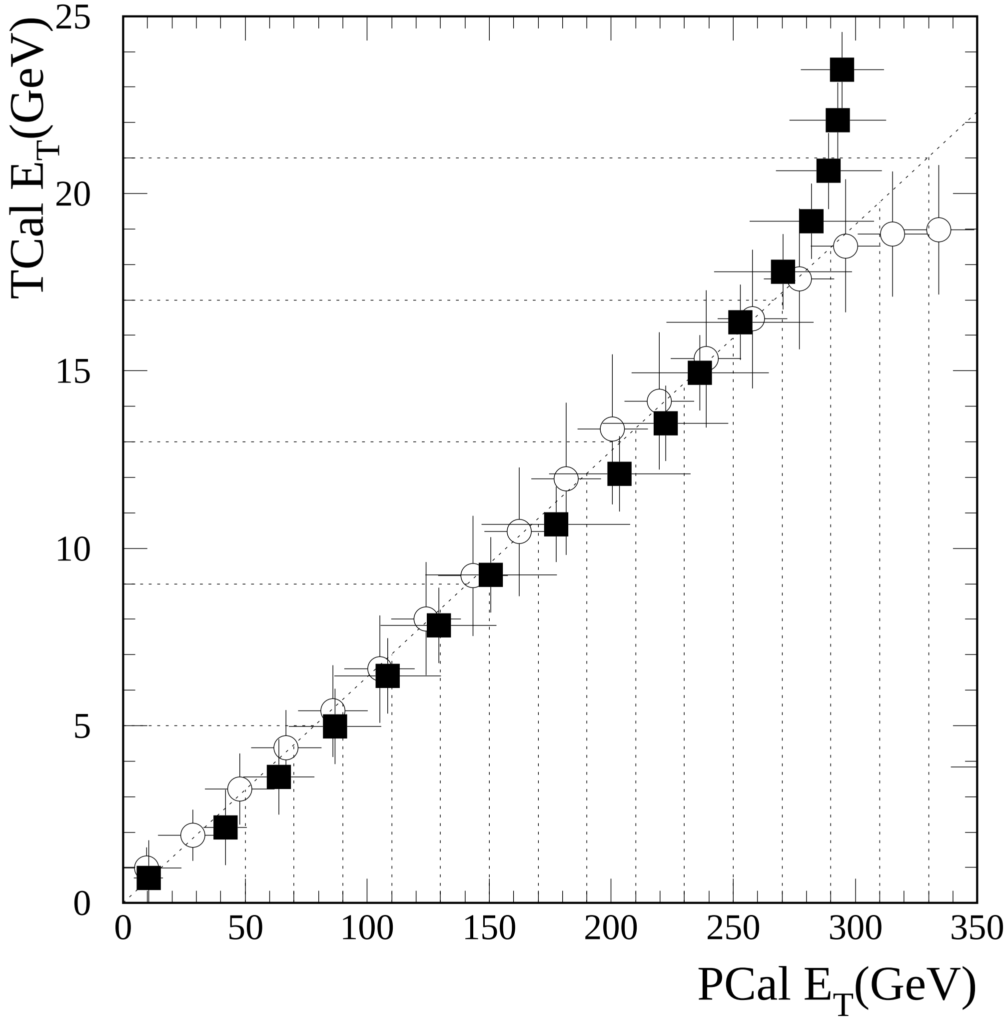

Figure 3.5: Correlation of the measured transverse energies in the two calorimeters projecting on the PCAL (open circles) and on the TCAL (solid squares) scale. The error bars indicate the width (standard deviation) of the correlation.

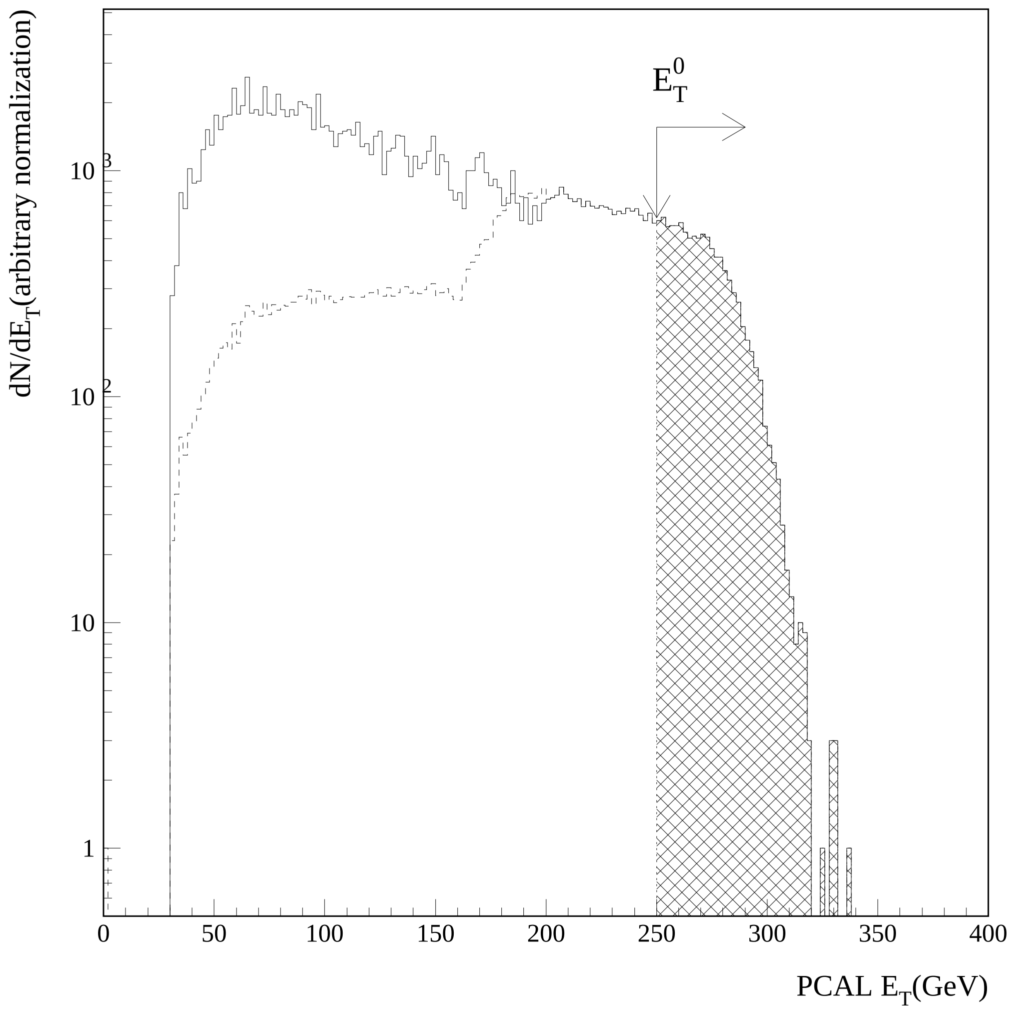

Figure 3.6: The dN/dE_T distribution and centrality definition by E_T measurements in PCAL. The solid histogram is constructed from the dashed histogram by accounting for the trigger down-scale factor (DS). The ratio of the integral over the hatched area for $E_T > E_T^0$ to the total geometrical cross section defines the corresponding centrality.

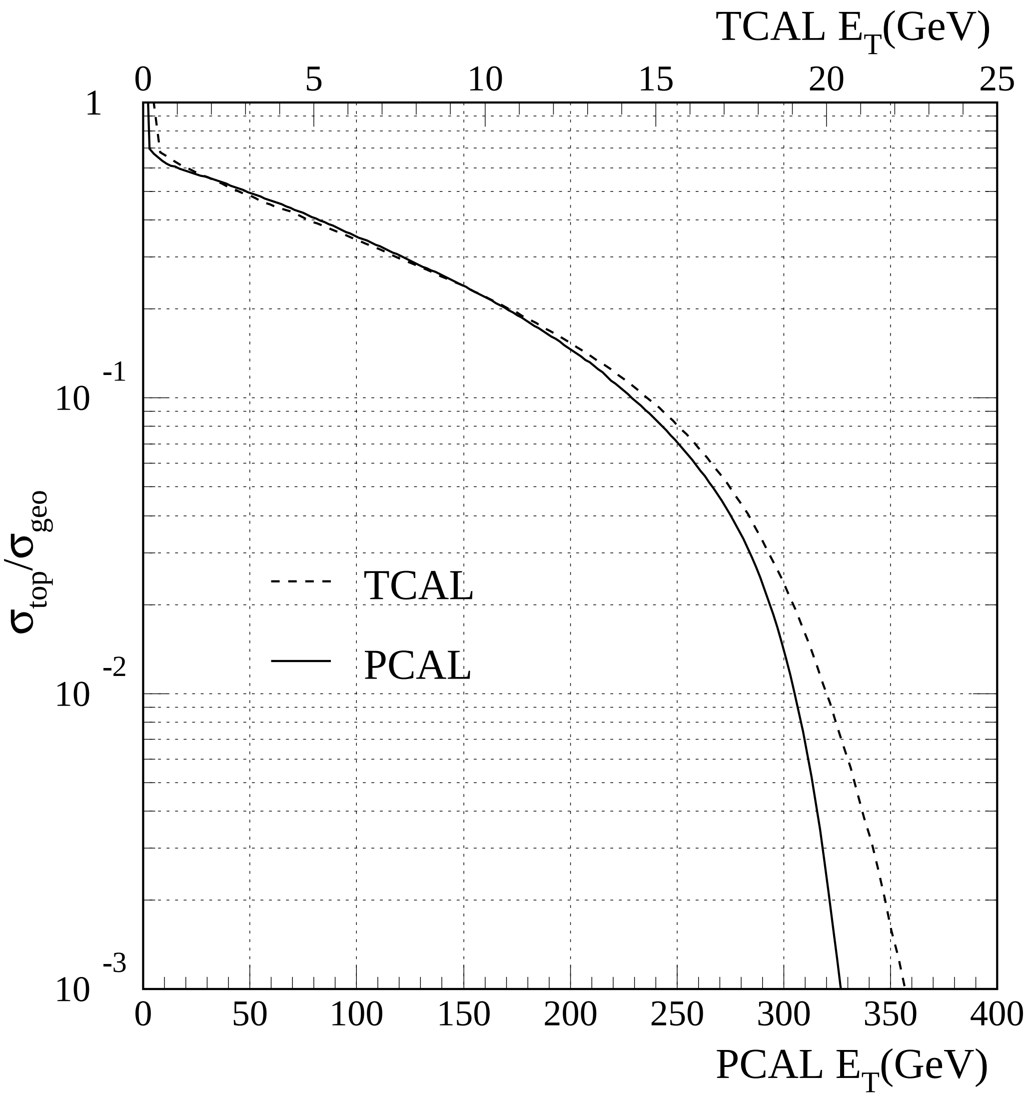

Figure 3.7: The ratio of the most central interaction cross section to the geometrical cross section as a function of corresponding E_T^0 cut on TCAL and PCAL E_T . The label of the horizontal axis at the top(bottom) of the figure is TCAL(PCAL) E_T .

Table 3.1: Second level trigger thresholds and down-scale factors.

triggers	TCAL1	TCAL2	TCAL3	PCAL1	PCAL3
threshold	270	550	1000	200	1500
σ_{top}/σ_0	30%	20%	8%	50%	10%
down-scale(A field)	10	7	1	20	1
statistics(A field)	0.4M	0.4M	0.8M	0.3M	1.2M
down-scale(B field)	10	7	1	9	1
statistics(B field)	0.4M	0.4M	1.0M	0.6M	1.6M

the magnet and has an angular acceptance of $-134 < \theta_x < 16$ mrad and $-11 < \theta_y < 1$ mrad in the lab system.

The strategy of particle identification is to calculate the mass of a particle from its measured momentum (determined by tracking and magnetic field) and time of flight. The details are described in Appendix D.

3.2 Data Collection and Good Event Definition

The data used in this thesis was collected in the Fall of 1993. During the run, beam particles passed the beam trigger, which is defined by the logic of $\bar{\mathrm{S}}1 \times \mathrm{S}2 \times \bar{\mathrm{S}}3 \times \mathrm{S}4$. The thickness of the target correspond to about 2% of a Au interaction length. A pre-trigger requires a minimal energy deposition in PCAL (about 1 GeV). A first level trigger is set to reject events where another beam particle enters the apparatus within 1 μs after the event. A second level trigger is designed to select about 50 events per spill, limited by our data acquisition system. In this trigger, analog signals from different sectors of the TCAL, PCAL, and MULT are digitized by FERA ADCs (fast analog to digital converters) to form a digital sum which is proportional to the total transverse energy (E_T). This digital sum is then compared with three levels of thresholds, keeping all the events passing the highest threshold, while only keeping a fraction of the events passing the lower thresholds by down-scaling these triggers. Table 3.1 lists down-scale factors, three thresholds and their corresponding cross sections. Since our study of centrality dependence is on narrow exclusive centrality bins, the trigger bias is only effective in a few bins and is estimated to be small.

The good event definitions in the offline analysis to eliminate double beams and upstream interactions. The various criteria and its rejection percentage are given in the following and shown schematically in Fig. 3.8:

1. A reasonable PCAL E_T range(0.08%).
2. A reasonable TCAL E_T range(8%).
3. A reasonable correlation between PCAL E_T and TCAL E_T (0.007%).
4. A reasonable correlation between PCAL E_T and UCAL E(0.02%).
5. Only one beam cluster detected in the BVER(9%).
6. Reasonable beam angle range measured by BVER(5%).
7. Reasonable sum of pulse height on BSCI2(0.2%).
8. Reasonable sum of pulse height on BSCI4(0.5%).
9. Reasonable pulse height of SILI(6%).
10. Reasonable target position measured by BVER(0.3%).
11. No blast events (the events failing the tracking procedure)(2%).

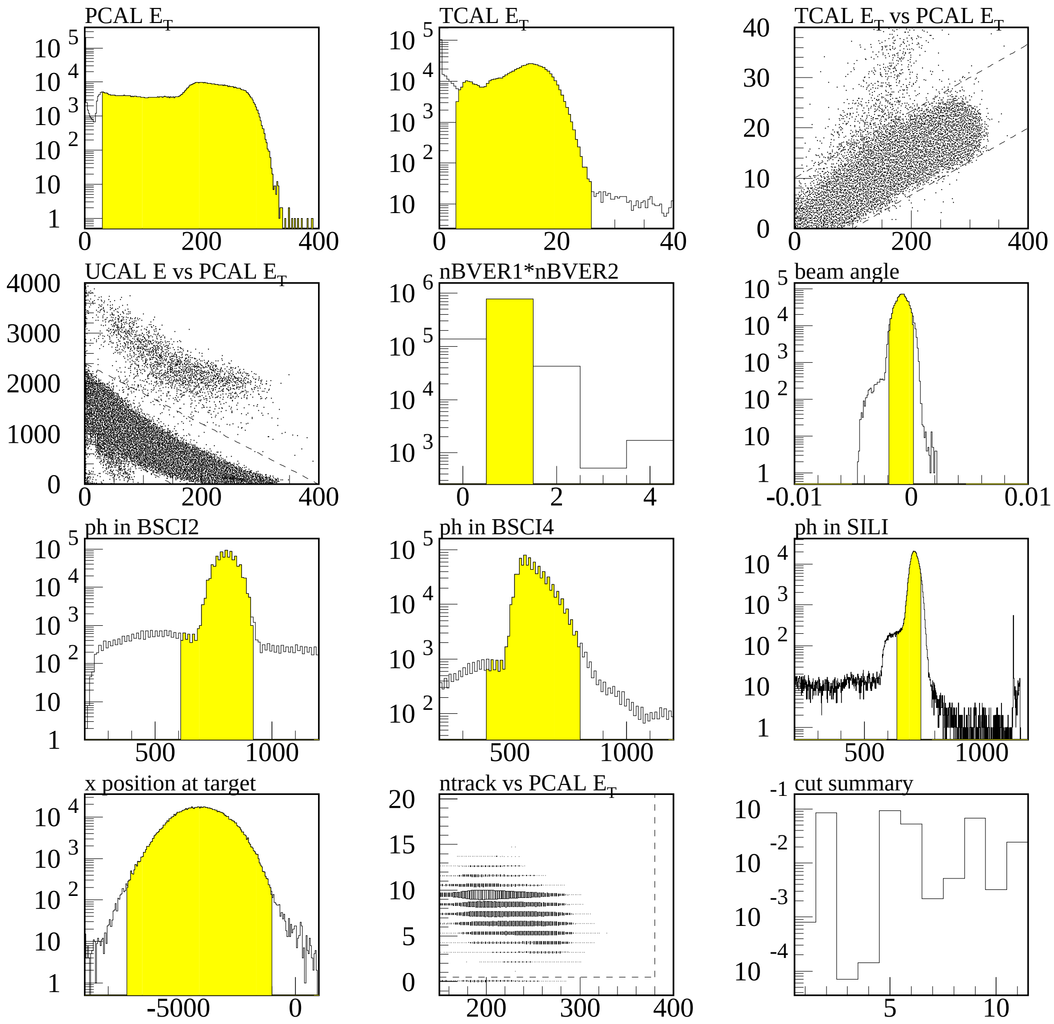

Figure 3.8: Various selection criteria of good events. The shaded area and the one enclosed with the dashed line are what are selected as good events. The last plot is a summary of the rejection rate corresponding to each criterion.

Chapter 4

Flow Analysis with Respect to the Reaction Plane

4.1 Introduction

Experiment E877 has reported the first observation of directed flow in Au + Au at AGS energies [31, 55]. This pioneering analysis performed a Fourier analysis of the azimuthal distribution of E_T event by event resulting in the observation of a maximum peak of the distribution of Fourier moments off the origin, sufficiently demonstrating directed flow [34]. The greatest advantage of this analysis is that there is no need to determine the reaction plane in the analysis and thus no need to correct for the reaction plane resolution. However, in order to distinguish a true anisotropy from statistical fluctuations and intrinsic resolution, the width of an η window has to be large enough. For practical purposes, this allowed a study of only 3 bins in our pseudo-rapidity coverage($-0.8 < \eta < 4.5$) and thereby a detailed study of the η-dependence of the flow signal is precluded.

The existence of directed flow enables us to reconstruct the reaction plane event by event so that one extra degree of freedom $\phi = \phi_{lab} - \Psi_R$, "the azimuthal angle with respect to the reaction plane", is introduced into the analysis where the azimuthal degree of freedom is usually integrated out or assumed to be azimuthally symmetric. Here ϕ_{lab} is the azimuthal angle of the detector in the lab system and Ψ_R, the determined reaction plane angle event by event. In this approach, as long as there exists a part of the detector system with full 2π azimuthal coverage which can be used to determine the reaction plane for every event, the randomness of the reaction plane orientation through all events will fill up 2π phase space of ϕ in other detectors which may have only limited azimuthal coverage (as e.g. a spectrometer). In the case of infinite statistics, the "granularity" (either η or y or p_t) of flow signals is only limited

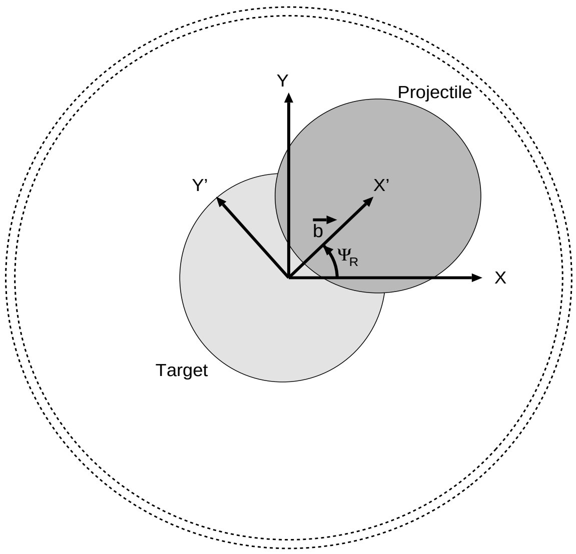

Figure 4.1: The geometry of a AA collisions

by the acceptance of detectors where the physics signals are observed. This enables us to make detailed analysis of the flow signal and set up stringent comparisons with model predictions.

4.2 The Reaction Plane

In the collision of two nuclei, the impact parameter vector $\vec{b}$ can be defined as a unit vector from the center of the target to that of the projectile and the reaction plane is defined as the one spanned by $\vec{b}$ and the beam direction (z axis). The reaction plane angle Ψ_R is the azimuthal angle between $\vec{b}$ and the x axis as shown in Fig. 4.1. In the experiment, Ψ_R is simulated as the "measured reaction plane angle" Ψ_1 from a physical measurement in any detector with 2π azimuthal coverage.

In the E877 setup, the two calorimeters TCAL and PCAL surrounding the target have full azimuthal acceptance over a wide pseudo-rapidity range ($-0.8 < \eta < 4.3$). We use the transverse energy E_T measurements in either detector to determine the reaction plane orientation using the following definitions:

Windows	TCW1	PCW2	PCW3	PCW4
η	[-0.5, 0.7]	[0.8, 1.4]	[2.0, 2.7]	[2.7, 4.5]

Table 4.1: Definition of windows in pseudo-rapidity for the determination of the reaction plane.

$$E_T = \sum_{i=1}^{N} E_T^i \tag{4.1}$$

$$E_x = \sum_{i=1}^{N} (\pm) E_T^i \cos(\phi_i^{lab}) \tag{4.2}$$

$$E_y = \sum_{i=1}^{N} (\pm) E_T^i \sin(\phi_i^{lab}) \tag{4.3}$$

$$\vec{E_T} = (E_x, E_y) \tag{4.4}$$

$$\Psi_1 = \arctan(\frac{E_y}{E_x}) \tag{4.5}$$

where i is the index of the calorimeter cell and ϕ_i^{lab} is the associated geometrical azimuthal angle in the lab system. With the assignment of $+1(-1)$ for forward(backward) calorimeter cells and the use of E_T as a weighting factor in Eq. 4.3, 4.4, the experimentally defined angle Ψ_1 is the direction of the mean E_T directed azimuthally in the forward hemisphere.

The η coverage of the two calorimeters TCAL and PCAL is divided into four windows as indicated in Table 4.1 and the gap in the window PCW2 and PCW3 is the mid-pseudorapidity where directed flow is close to zero. The reaction plane angle is independently determined in each of them for every event. One advantage in using these four independent windows is that auto-correlations can be avoided (see discussion below). Further, assuming that the directed flow is the dominating physical correlation among these windows, the reaction plane resolution of each window can be evaluated by studying the correlation of Ψ_1 obtained in different windows.

4.3 The Distribution of the Reaction Plane

Ideally, the randomness of the orientation of collision geometry should lead to a flat distribution in $dN/d\Psi_1$ over 2π or a two dimensional isotropic distribution of the directivity vector $\vec{E_T}$ around the origin [31]. However, due to imperfections in the calorimeters, such as inaccurately calibrated or dead cells, the distribution of the determined angle Ψ_1 is not flat. If the distortions are small, they can be corrected by eliminating the components of higher Fourier moments of $dN/d\Psi_1$ to make the distribution flat [55]. The correction procedure described below is performed in the sense of a "global correction", i.e. overall on the event-averaged sample of one run(about 30K events). This is justified when the defects (imperfections) of the detector are static within this sample which means that the corrections do not change as a function of time in collecting this set of data.

It consists of two steps:

1. **The shift of the origin to be the center of the distribution:**

   First, we make the mean E_x, E_y averaged over all events to be zero by implementing an appropriate shift.

$$E^o_{x,y} = \sum_{i=1}^{N} E^i_{x,y} \tag{4.6}$$

$$E'^i_x = E^i_x - E^o_x \tag{4.7}$$

$$E'^i_y = E^i_y - E^o_y. \tag{4.8}$$

   Here i is the event index for a specific event sample classified by an E_T (or centrality) range.

$$\Psi'^i_{1,raw}[-\pi, \pi] = \arctan(\frac{E'^i_y}{E'^i_x}) \tag{4.9}$$

   This leads to a new definition of the reaction plane orientation. It is important to note that the shift of the center, in essence, affects all high-order Fourier harmonics in the distribution and is only an approximation of a correction of first harmonics when the magnitude of the shift of the center is small (see Appendix A).

2. **Correction of the remaining harmonics:**

   A further corrected angle $\Psi''^i_{1,raw}$ is obtained by using the correction factor $\Delta\Psi'_{1,raw}$ defined as:

$$\Delta\Psi'^{i}_{1,raw} = \sum_n \Big(A_n \cos(n\Psi'^{i}_{1,raw}) + B_n \sin(n\Psi'^{i}_{1,raw})\Big) \quad (4.10)$$

$$\Psi''^{i}_{1,raw} = \Psi'^{i}_{1,raw} + \Delta\Psi'^{i}_{1,raw} \quad (4.11)$$

By requiring a vanishing nth Fourier moment of the new distribution, the coefficients A_n and B_n can be evaluated by the original distribution.

$$\begin{aligned}
\langle\cos(n\Psi''_{1,raw})\rangle &= 0 && (4.12)\\
&= \langle\cos(n\Psi'_{1,raw} + n\Delta\Psi'_{1,raw})\rangle && (4.13)\\
&\simeq \langle\cos(n\Psi'_{1,raw})\rangle - \langle\sin(n\Psi'_{1,raw})n\Delta\Psi'_{1,raw}\rangle && (4.14)\\
&= \langle\cos(n\Psi'_{1,raw})\rangle - n\ B_n/2 && (4.15)\\
B_n &= \frac{2}{n}\langle\cos(n\Psi'_{1,raw})\rangle && (4.16)
\end{aligned}$$

and,

$$\begin{aligned}
\langle\sin(n\Psi''_{1,raw})\rangle &= 0 && (4.17)\\
&= \langle\sin(n\Psi'_{1,raw} + n\Delta\Psi'_{1,raw})\rangle && (4.18)\\
&\simeq \langle\sin(n\Psi'_{1,raw})\rangle + \langle\cos(n\Psi'_{1,raw})n\Delta\Psi'_{1,raw}\rangle && (4.19)\\
&= \langle\sin(n\Psi'_{1,raw})\rangle + n\ A_n/2 && (4.20)\\
A_n &= \frac{-2}{n}\langle\sin(n\Psi'_{1,raw})\rangle. && (4.21)
\end{aligned}$$

This leads to,

$$\begin{aligned}
\Psi''^{i}_{1,raw} = \Psi'^{i}_{1,raw} + \sum_n \frac{2}{n}\Big(& -\langle\sin(n\Psi'_{1,raw})\rangle\cos(n\Psi'^{i}_{1,raw})\\
& +\langle\cos(n\Psi'_{1,raw})\rangle\sin(n\Psi'^{i}_{1,raw})\Big) \quad (4.22)
\end{aligned}$$

In practice, we need to implement corrections up to $n = 4$ because of the intrinsic four-fold symmetry of the calorimetry. The angle $\Psi''_{1,raw}$ gives the corrected reaction plane orientation with a flat distribution averaged over all events and is the angle used as the measured reaction plane angle and labeled as Ψ_1. The reaction plane distribution after each step of this correction procedure for the PCW3 window without centrality cuts is shown in Fig. 4.2. In practice, the non-flatness is found to be more severe for PCAL windows as compared to TCAL.

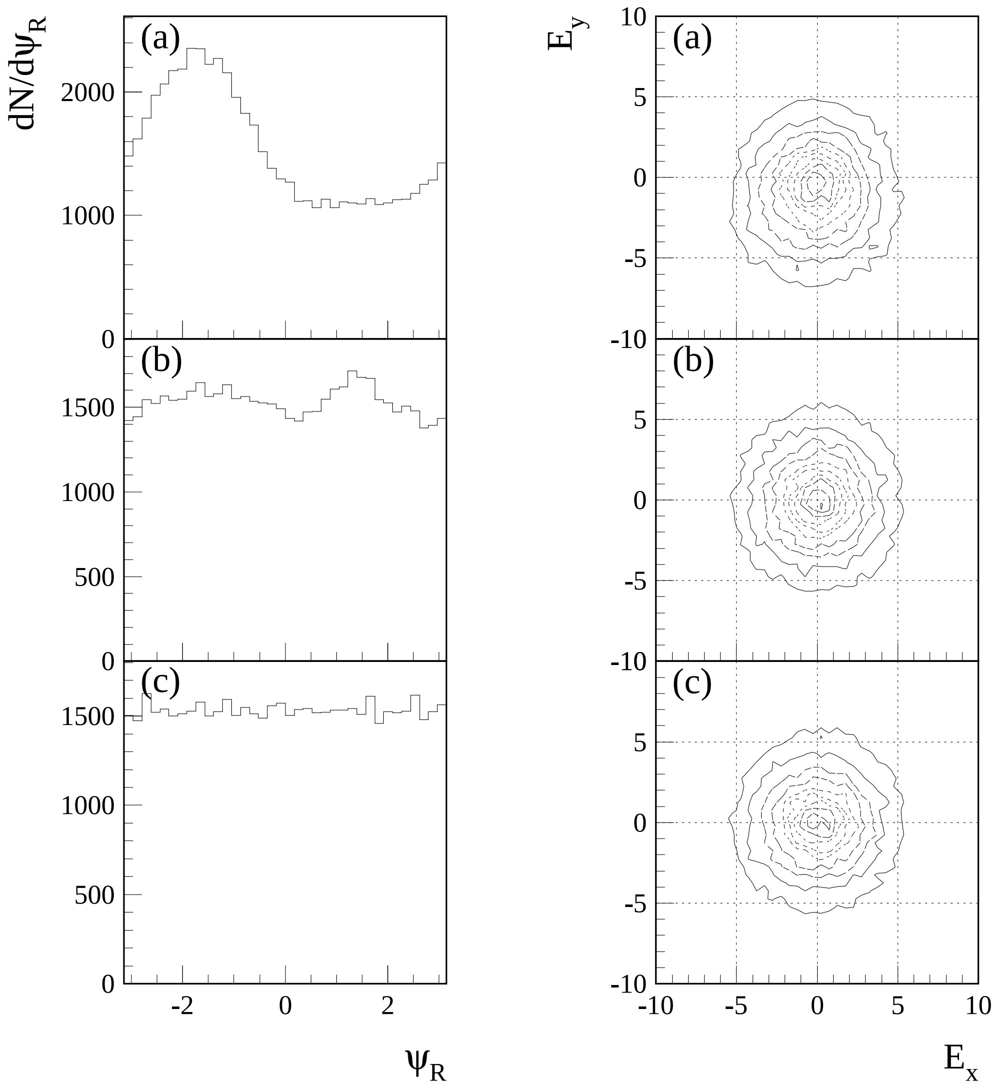

Figure 4.2: The distribution of determined reaction plane angle (left panel) and transverse energy vector $\vec{E_T}$ (right panel) in the PCW3 window without centrality cuts are shown from the uncorrected (a.), after the shift of center (b.), to the elimination of all harmonics up to n=4(c.).

4.4 The Reaction Plane Resolution

Due to finite resolution in the measured reaction plane angle Ψ_1 as compared to the true reaction plane angle Ψ_R, the measured anisotropy with respect to the reaction plane will be smaller than the true value. However, this difference can be corrected for the so called "reaction plane resolution". We explain this by the following simple example of the analysis of the anisotropy on the global variable G (e.g. charge multiplicities N_{ch} , transverse energy E_T ,...) in a certain pseudo-rapidity(η) region.

Theoretically,

$$\begin{aligned} \frac{dG}{d\phi}(\eta) &= \langle G(\eta)\rangle(1+\sum_{n=1}^{N} 2\, v_n(\eta)\cos(n\phi)), \qquad (4.23) \\ \phi &= \phi_{\mathrm{lab}} - \Psi_R \end{aligned}$$

Experimentally,

$$\begin{aligned} \frac{dG}{d\phi'}(\eta) &= \langle G(\eta)\rangle(1+\sum_{n=1}^{N} 2\, v'_n(\eta)\cos(n\phi')), \qquad (4.24) \\ \phi' &= \phi_{\mathrm{lab}} - \Psi_1 \end{aligned}$$

The relation between v_n and v'_n can be derived as,

$$\begin{aligned} v'_n &= \frac{\langle G\cos(n\phi')\rangle}{\langle G\rangle} \qquad (4.25) \\ &= \frac{\langle G\cos(n\phi)\rangle\langle\cos(n\Delta\Psi_1)\rangle}{\langle G\rangle} - \frac{\langle G\sin(n\phi)\rangle\langle\sin(n\Delta\Psi_1)\rangle}{\langle G\rangle} \qquad (4.26) \\ &= v_n\langle\cos(n\Delta\Psi_1)\rangle \qquad (4.27) \end{aligned}$$

with $\Delta\Psi_1 = \Psi_1 - \Psi_R$. The term $\langle\sin n\Delta\Psi_1\rangle$ vanishes because of the symmetry distribution around $\Psi_R = 0$ in our colliding system of Au + Au.

Therefore, we can unfold the finite resolution for the Fourier moments by dividing the measured Fourier moments by the event-averaged mean cosine value of the difference between Ψ_R and Ψ_1 [34],

$$\begin{aligned} v_n(\eta) &= \frac{v'_n(\eta)}{\langle\cos n(\Psi_1 - \Psi_R)\rangle} \qquad (4.28) \\ &= \frac{v'_n(\eta)}{\langle\cos(n\Delta\Psi_1)\rangle}. \qquad (4.29) \end{aligned}$$

And the reaction plane resolution of the nth moment of flow signal can be quantified as $\langle \cos\ n(\Psi_1 - \Psi_R)\rangle$, where the bracket means that the event-averaged quantity is used. The following discussion about how to calculate $\cos n(\Psi_1 - \Psi_R)\rangle$ is for the first moment (n=1) only and can be generalized to higher moments.

If the angle Ψ_1 is determined in three(or more) independent windows for each event and we assume that the directed flow is the dominating physical correlation among them, the reaction plane resolution for each window i ($\langle \cos(\Psi_1^i - \Psi_R)\rangle$) can be calculated by studying the correlation of Ψ_1 determined in different windows ($\langle \cos(\Psi_1^i - \Psi_1^j)\rangle$).

$$
\begin{aligned}
\cos(\Psi_1^i - \Psi_1^j) &= \cos((\Psi_1^i - \Psi_R) - (\Psi_1^j - \Psi_R)) &\quad (4.30)\\
&= \cos(\Psi_1^i - \Psi_R)\cos(\Psi_1^j - \Psi_R) \\
&\quad + \sin(\Psi_1^i - \Psi_R)\sin(\Psi_1^j - \Psi_R) &\quad (4.31)
\end{aligned}
$$

If we take the event-average on both sides of Eq. 4.31 and, with the above assumption, separate the event average of the product of terms in different windows, we can get

$$
\begin{aligned}
\langle\cos(\Psi_1^i - \Psi_1^j)\rangle &= \langle\cos(\Psi_1^i - \Psi_R)\cos(\Psi_1^j - \Psi_R)\rangle \\
&\quad + \langle\sin(\Psi_1^i - \Psi_R)\sin(\Psi_1^j - \Psi_R)\rangle &\quad (4.32)\\
&= \langle\cos(\Psi_1^i - \Psi_R)\rangle\langle\cos(\Psi_1^j - \Psi_R)\rangle\rangle \\
&\quad + \langle\sin(\Psi_1^i - \Psi_R)\rangle\langle\sin(\Psi_1^j - \Psi_R)\rangle &\quad (4.33)\\
&= \langle\cos(\Psi_1^i - \Psi_R)\rangle\langle\cos(\Psi_1^j - \Psi_R)\rangle. &\quad (4.34)
\end{aligned}
$$

The second term on the right hand side of Eq.4.34 vanishes because of the symmetry of the colliding system (Au + Au) with respect to the reaction plane.

Therefore, when the correlation between any two windows is known, the resolution of one specific window is expressed as

$$
\mid\langle\cos(\Psi_1^i - \Psi_R)\rangle\mid = \sqrt{\frac{\langle\cos(\Psi_1^i - \Psi_1^j)\rangle\langle\cos(\Psi_1^i - \Psi_1^k)\rangle}{\langle\cos(\Psi_1^j - \Psi_1^k)\rangle}}. \qquad (4.35)
$$

One complication includes understanding how the non-uniformity of the distribution of the reaction plane angle in each window will affect the correlation value $\langle\cos(\Psi_1^i - \Psi_1^j)\rangle$. To understand this question, we study the correlation between different windows in two ways. The first is the direct calculation of $\langle\cos(\Psi_1^i - \Psi_1^j)\rangle$ event by event. The second is to define a normalized function of angle correlation as

$$\frac{dP}{d\Delta\Psi_1^{ij}} = \frac{\frac{dN}{d\Delta\Psi_1^{ij}}|_{\text{same event}}}{\frac{dN}{d\Delta\Psi_1^{ij}}|_{\text{mixed event}}} \tag{4.36}$$

where $\Delta\Psi_1^{ij} = \Psi_1^i - \Psi_1^j$.

The "mixed event" label means that the Ψ_1^i , Ψ_1^j are randomly selected from events of the same event class. The entries of the "mixed event" sample are copiously generated in order to define a smooth background shape. Then the resolution is evaluated by means of the probability function

$$\langle\cos(\Psi_1^i - \Psi_1^j)\rangle = \frac{\int \frac{dP}{d\Delta\Psi_1^{ij}} \cos(\Psi_1^i - \Psi_1^j)\, d\Delta\Psi_1^{ij}}{\int \frac{dP}{d\Delta\Psi_1^{ij}}\, d\Delta\Psi_1^{ij}}. \tag{4.37}$$

Thereby, we expect the effect of the non-uniformity of individual distributions in Ψ_1^i, Ψ_1^j on the $\langle\cos(\Psi_1^i - \Psi_1^j)\rangle$ to be removed. We find that the difference between these two approaches is small, typically 5 % or less for all four pseudo-rapidity windows. For the following analysis the values resulting from the second approach have been used. The resolutions for these four windows of the first two Fourier moments are shown in Fig. 4.3 where also the difference between these two approaches can be seen.

4.5 The Residual Non-flatness in the Reaction Plane Distribution

In this section, we discuss how any residual non-flatness of the reaction plane propagates into the flow signal and how to subtract the effect. In reality, there exists of the order of 0.3% of the first harmonic after the global correction.

Consider one part of the detector, located at a fixed azimuthal angle ϕ in the lab system. The first Fourier moment v_1^{obs} (before correction for the reaction plane resolution) of the azimuthal distribution observed by it is evaluated as:

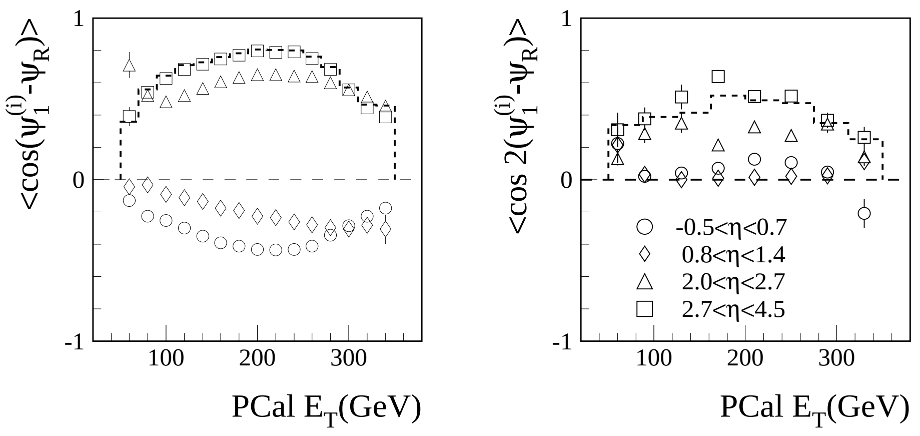

Figure 4.3: The correction to the first moment v_1 (left) and the second moment v_2 (right) due to the finite resolution of the reaction plane angle measurement in four different bins of pseudo-rapidity. Dotted line: correction factors for the most forward pseudo-rapidity bin obtained without normalizing to the "mixed event" distribution (see text).

$$v_1^{obs} = \frac{\int \frac{dN}{d(\phi - \Psi_1)} \cos(\phi - \Psi_1) P(\Psi_1) d\Psi_1}{\int \frac{dN}{d(\phi - \Psi_1)} P(\Psi_1) d\Psi_1}, \tag{4.38}$$

where $dN/d(\phi - \Psi_1)$ is the observed azimuthal distribution of the physical quantity. Extra weights such as E_T and N_{ch} can be applied to the distribution in the cases of the calorimeter and charged multiplicity detector.

To the first order, the azimuthal distribution is

$$dN/d(\phi - \Psi_1) \simeq N_0(1 + 2v_1^{true} \cos(\phi - \Psi_1)). \tag{4.39}$$

In Eq. 4.38 $P(\Psi_1)$ is the probability distribution of the reaction plane angle which ideally should be flat, but in practice always has small finite anisotropy. Assume this non-flatness can be approximated by

$$P(\Psi_1) \simeq P_0(1 + 2a_1 \cos(\Psi_1) + 2b_1 \sin(\Psi_1)). \tag{4.40}$$

We assume that v_1^{true}, a_1, and $b_1 \ll 1$. Then in first order approximation, v_1^{true} can be recovered from v_1^{obs}:

$$
\begin{aligned}
v_1^{obs} &= \int (1 + 2v_1^{true}\cos(\phi - \Psi_1) + 2a_1\cos(\Psi_1) + 2b_1\sin(\Psi_1))\cos(\phi - \Psi_1)d\Psi_1 \\
&= v_1^{true} + a_1\cos(\phi) + b_1\sin(\phi). \qquad (4.41)
\end{aligned}
$$

Averaging over the acceptance of the overall detector, we get

$$
\begin{aligned}
v_1^{true} &= v_1^{obs} - (a_1\langle\cos(\phi)\rangle + b_1\langle\sin(\phi)\rangle) \\
&= v_1^{obs} - v_1^{bkgr}. \qquad (4.42)
\end{aligned}
$$

This correction formula can be easily generalized for flow signals of higher moment v_n^{true}.

The correction v_1^{bkgr} vanishes if either Ψ_1 is flat ($a_1 = b_1 = 0$), or the acceptance of the detector is constant over the full 2π azimuthal angle range as is the case in our flow analysis of global variables measured in MULT, TCAL and PCAL. However, in our measurement of the flow signals of identified particles, this correction needs to be taken into account because of the finite azimuthal coverage of the forward spectrometer.

We demonstrate the effect in the measurement of $v_1(p_t)$ of protons at rapidity $2.8 < y < 3.0$ with the centrality cut $200 <$ PCAL$E_T < 230$ GeV in the spectrometer in Fig. 4.4. The averaged values $\langle\cos(\phi)\rangle$ and $\langle\sin(\phi)\rangle$ of the acceptance of protons in the spectrometer are plotted as the left two figures and the right most plot is the evaluation of the corresponding background of the flow signal $v_1(p_t)$ due to the residual non-flatness of the reaction plane distribution.

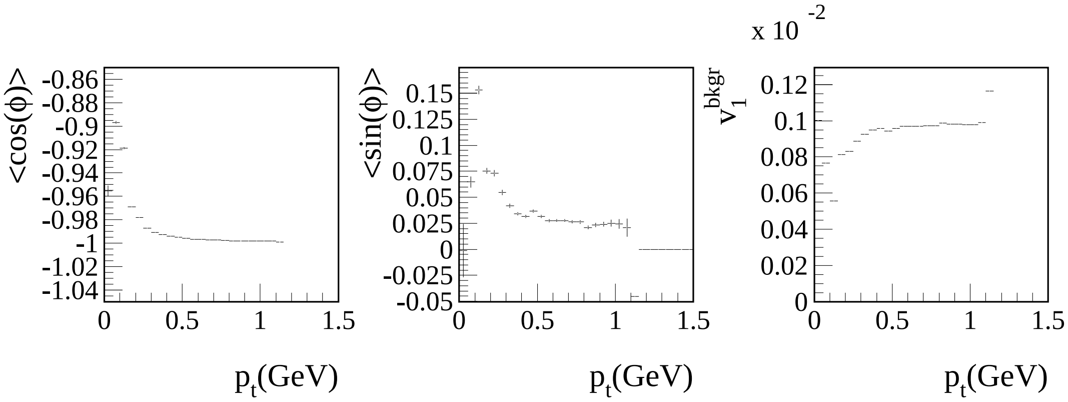

Figure 4.4: From left to right, the plot of $\langle\cos(\phi)\rangle(p_t)$ and $\langle\sin(\phi)\rangle(p_t)$ and the background of the flow signal $v_1(p_t)$. See text for a detailed description.

Chapter 5

Transverse Energy Flow

In this chapter, we discuss the flow signal observed in the E_T measurement by the calorimeters TCAL and PCAL. An overview of the analysis is given in the first section. Due to the shower spread in the calorimeter, the effective value of η of each tower needs a calibration; this procedure will be explained in the second section. In the final section, we present the results and discuss the observations.

5.1 The Strategy of the Analysis

For each cell of the calorimeters (TCAL and PCAL), we construct the azimuthal distribution with respect to the reaction plane of deposited transverse energy E_T for all events. There are four sets of the distributions which correspond to different choices of the orientation of the reaction plane determined in four windows. The question of avoiding the auto-correlations will be discussed later.

Therefore

$$\frac{dE_T}{d\phi'}(\eta_i) = \sum_{j=1}^{N} \frac{dE_T^j}{d(\phi_i^{\mathrm{lab}} - \Psi_1^j)} \tag{5.1}$$

where i is the index of towers and j enumerates different events.

Then we group cells, after excluding those channels known to be dead or poorly calibrated, into different η bins and construct the event shape of E_T over the pseudo-rapidity space η, i.e.

$$\frac{dE_T}{d\phi' d\eta} = \sum_i \frac{dE_T}{d\phi'}(\eta_i). \tag{5.2}$$

In each η slice, the azimuthal distribution can be expanded in terms of its Fourier components,

$$\frac{dE_T}{d\phi'}|_{\eta,\mathrm{centrality}} = \frac{\langle E_T\rangle}{2\pi} + \frac{1}{\pi}\sum_{n=1}^{\infty}(a_n\cos(n\phi') + b_n\sin(n\phi')) \tag{5.3}$$

$$a_n = \int_{\phi'=0}^{\phi'=2\pi}\frac{dE_T}{d\phi'}\cos(n\phi')d\phi' \tag{5.4}$$

$$b_n = \int_{\phi'=0}^{\phi'=2\pi}\frac{dE_T}{d\phi'}\sin(n\phi')d\phi'. \tag{5.5}$$

Because of the mirror symmetry of the reaction plane, the coefficients b_n should be equal to the zero. Therefore, we quantify the flow effect by v'_n, i.e. normalized a_n, and use the deviation b_n of from zero as an estimate of its error.

$$\frac{dE_T}{d\phi'}|_{\eta,\mathrm{centrality}} = v_0\left(1 + \sum_i 2v'_n\cos(n\phi')\right) \tag{5.6}$$

$$v'_0 = \frac{\langle E_T\rangle}{2\pi} \tag{5.7}$$

$$v'_n(n>0) = \frac{a_n}{\langle E_T\rangle} \tag{5.8}$$

$$\delta v'_n(n>0) = \frac{|b_n|}{\langle E_T\rangle} \tag{5.9}$$

The final step is to correct for the reaction plane resolution as described in the previous chapter.

$$v_n(\eta) = \frac{v'_n}{\langle\cos(n\Delta\Psi_1)\rangle} \tag{5.10}$$

5.2 The Calibration of η for the PCAL Towers

Because the particles impinging on the PCAL cause a shower spreading in the depth and laterally in the calorimeter, the η value corresponding to the geometrical center of each tower is usually not the mean η of the particles which deposit energy in this tower. By feeding the output of event generators (a simple fireball model described at Appendix B, and RQMD), which reproduces the pseudo-rapidity distribution of transverse energy ($dE_T/d\eta$), into a GEANT simulation of the PCAL with a simplified parameterization of the spread of hadronic showers (PROPHET) [52], we get the distribution of particles depositing energy in each cell. Then we take the mean η of particles contributing to a tower weighted with the deposited energy, as the new η characterizing the tower. This quantity is plotted in Fig. 5.1 versus the η corresponding to the geometrical center of a tower. In the smaller η region ($\eta < 3$), the mean η of depositing particles will be underestimated by the geometrical center of tower because the gradient of deposited energy shower is toward larger η. In the most forward region, only shower spread from particles of smaller η towards larger η(small polar angle) is possible so that the geometrical η will be an overestimate. The calibrated new η values of the towers are not sensitive to our choices of different event generators or different centralities (2%, 10%) within 2% (Fig. 5.2). Thus we conclude that this calibration procedure has little model and centrality dependence.

Another approach is to utilize the method of a response matrix in similar to that used to obtain the (azimuthally integrated) transverse energy distribution $dE_t/d\eta$ [52]. By inputting a parameterization of flow signals of particles as a function of η, and using the distribution of particles coming into each tower as the response matrix, we fit the measured flow signal as a function of η of the geometrical center for each tower. This method unfolds the flow signal of particles depositing energy similar to the results of redefining the η value of a tower. As can be seen in Fig. 5.3, this method is more powerful in revealing the detailed structure of flow in the most forward η region where the shower spread is over many towers, and there is a lack of resolution of η in the towers. Otherwise, these two approaches are in principle equivalent and indeed we get similar results from them. In practice, we use the first approach of reassigning an effective η to each tower when we group the distributions into various η bins in Eq. 5.2.

5.3 Collective Flow of Transverse Energy

In Fig. 5.4, the event shape of E_T production is displayed with respect to the reaction plane (determined in the windows where the autocorrelations do not exist) for the centrality bin of 10-15% of the geometric cross section. The direction of the anisotropy varies with pseudo-rapidity(η). As shown in the various η slices, the direction of the transverse energy vector shifts from $\phi' = \pi$ in the backward η bins to $\phi' = 0$ at forward η. In the mid-η bin ($\eta = 2.0$), an obvious two-fold symmetry, i.e. non-zero second Fourier component, is observed. The back-to-back correlation of forward and backward η is a necessary characteristic of directed flow. Because energy leakage of the TCAL

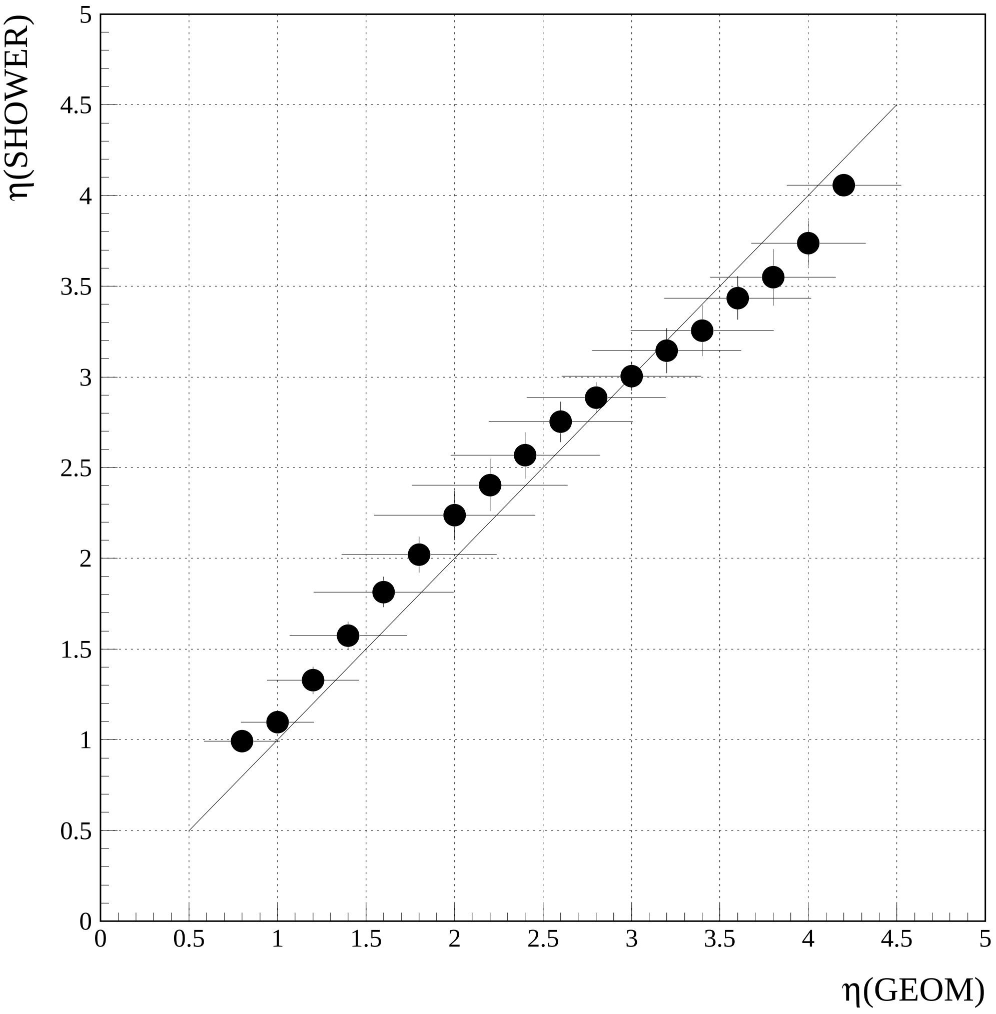

Figure 5.1: The correlation of redefined effective η and the geometrical η of the PCAL towers. The vertical error bars represent the uncertainty of the re-calibrated η from the finite width in the distribution of the η of the deposited particles which is the horizontal error bars. The input of events are from RQMD with a cut on the top 2% centrality.

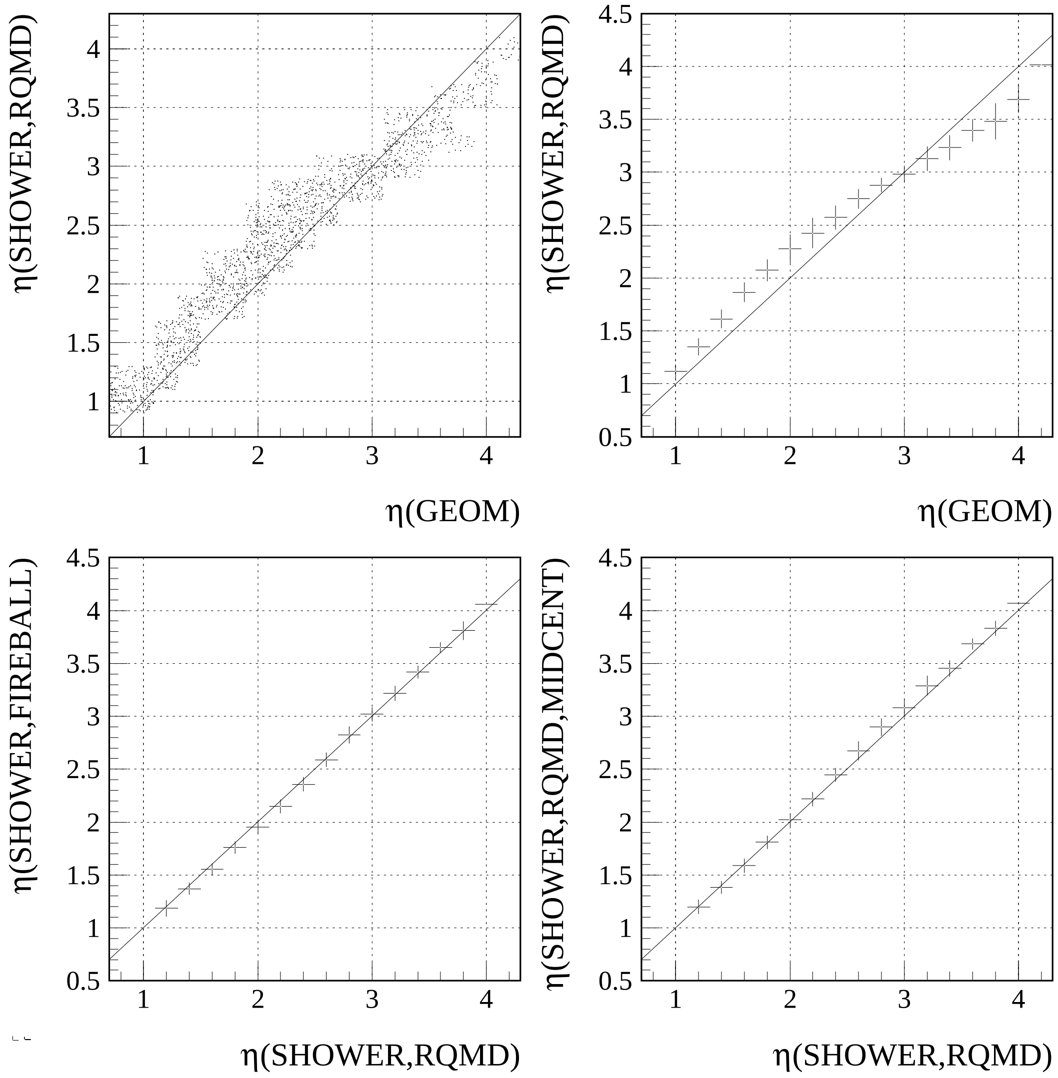

Figure 5.2: Plots of the correlations between redefined effective η determined by two different models(fireball model and RQMD) as event generators and two different centralities(the most central 2% and 10%) versus the geometrical η of the PCAL towers.

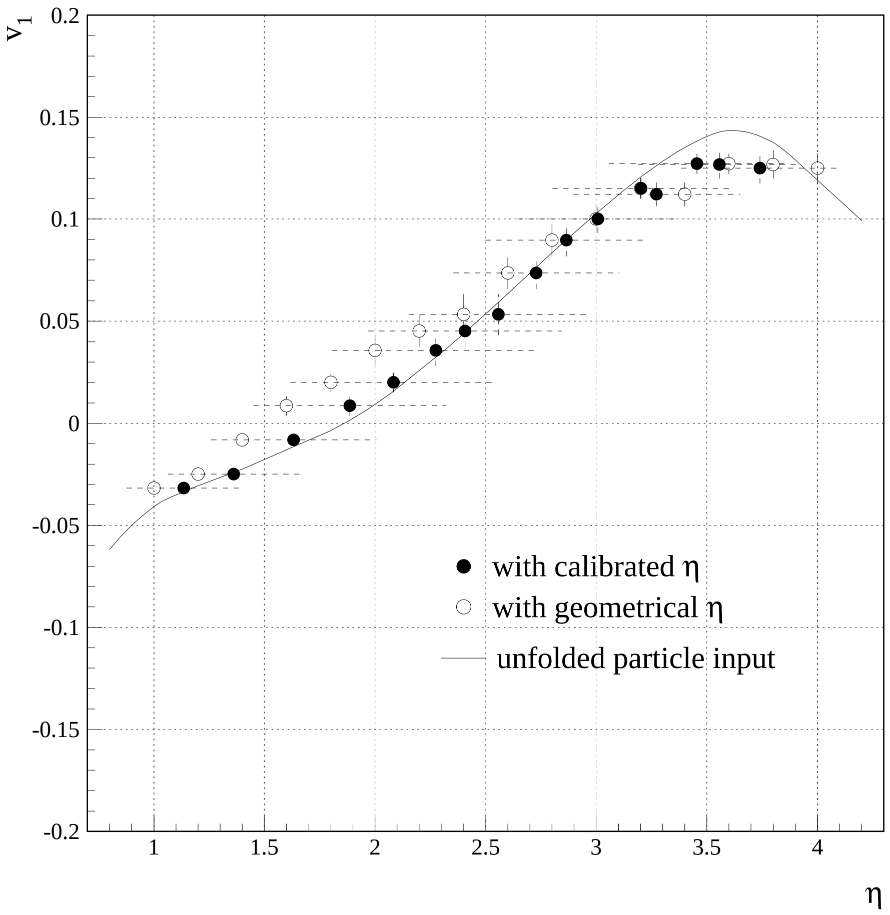

Figure 5.3: A comparison of two approaches in determining the $v_1(\eta)$ of particles. The solid symbols are the signals obtained using the re-calibrated η. The horizontal error bars represent the width in the distribution of the η of the deposited particles. The smooth curve is the unfolded flow signal of particles by the response matrix method(see text). For comparison the flow signal as a function of the η of the geometrical center of PCAL towers is shown as well(open symbols).

leads to a measured E_T scale about a factor of two below the true value [49], the E_T observed in the most backward direction is not shown in this plot.

A systematic study of the directed flow signal is performed by calculating the Fourier moments at different η and centrality bins and subsequently correcting the corresponding reaction plane resolution, shown in Fig. 5.5. The different symbols represent results obtained using the reaction plane determined in different pseudo-rapidity windows. The auto-correlation effect is obvious; it causes the flow signal to acquire a false enhancement if the reaction plane is also determined within the same pseudo-rapidity region. This is shown only for illustrative purposes and in general only the reaction planes determined in a non-overlapping η region have been used (see below). The analysis is reasonably good: after the resolution correction, similar flow signals are obtained by using the reaction plane orientations determined in different windows, even though the corresponding resolution corrections could be different by a factor of 2. The signals observed using the PCW2 window behaves differently from the other three due to the fact that it sits closest to mid-pseudorapidity where the directed flow signal used to determine the reaction plane is weakest. Therefore, in the analysis we exclude all flow signals using the reaction plane determined in this window.

The first and second moments of the azimuthal distribution, after removing the data points where the auto-correlation exists and averaging over the signals from different windows, are shown in Fig. 5.6(5.7) as a function of η at different centralities. The errors shown include statistical and systematic errors due to the values observed in different windows. In order to correct for any asymmetries caused by interactions other than in the target, we also evaluate the anisotropy coefficients from special target-out runs. It is found that only the first two most peripheral centrality bins are affected and the absolute correction to $v_1(v_2)$ is of the order of 0.005(0.001).

The centrality dependence of both the first(v_1) and second(v_2) moments is systematic: the flow signals increases from peripheral towards central collisions and reaches a maximum at mid-centrality and then diminishes towards the most central collisions. This centrality dependence is demonstrated in Fig. 5.8 for the moment v_2 at mid-η. The first moment v_1, identified as the directed flow component, shows the typical **S**-shape as a function of pseudo-rapidity. The location of the zero-crossing at η = 1.9 - 2.0 does not depend significantly on centrality except for the two most peripheral bins where more forward values are observed. The lack of a symmetry with respect to mid-η is not surprising. The flow signal is a mixture of two main components, nucleon and pion, which have different pseudo-rapidity distributions and possibly different individual flow signals. The second moment, v_2, is of almost constant positive value

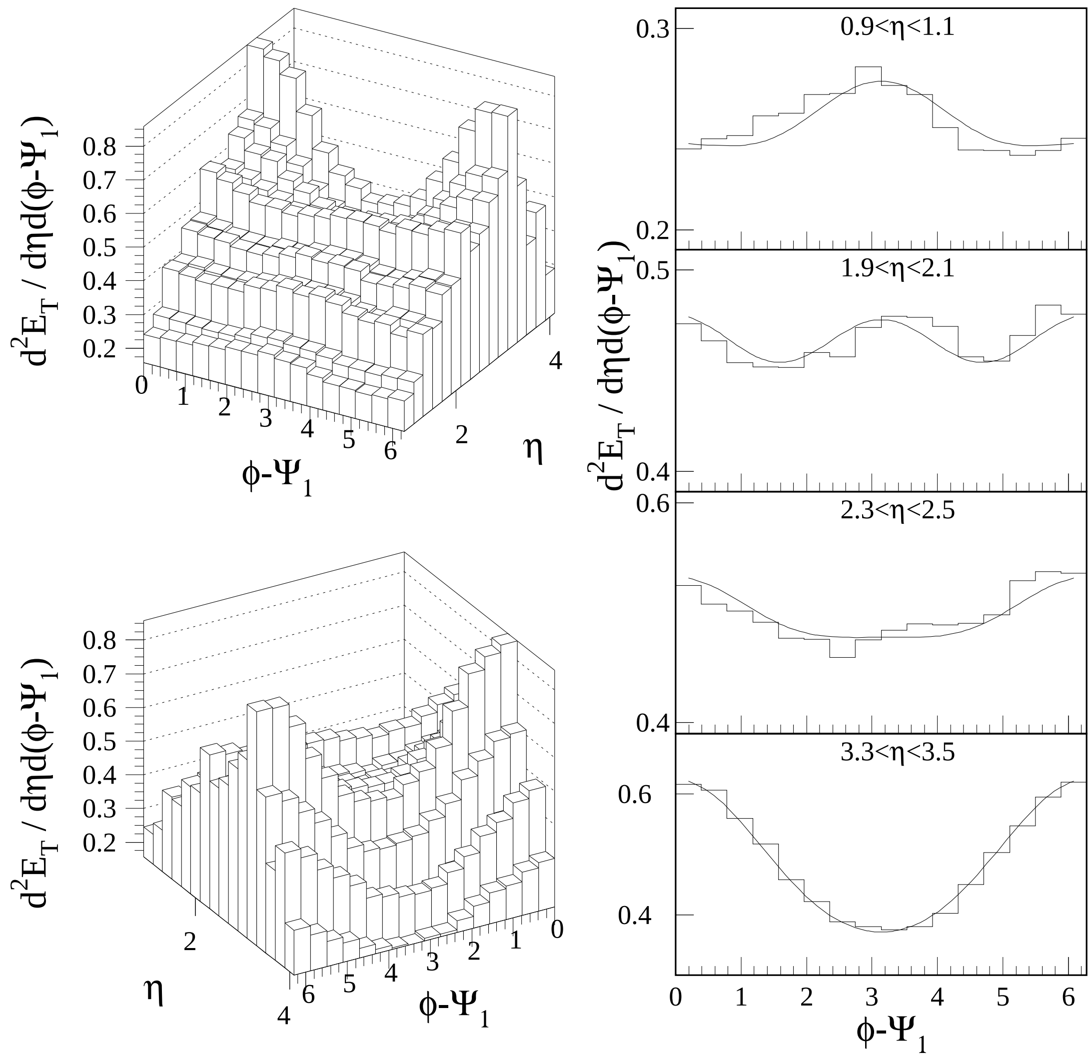

Figure 5.4: Left: Double differential transverse energy distributions for the intermediate PCAL centrality bin. Right: Four pseudo-rapidity bins of the same distribution. The solid lines are fitted curves with Fourier coefficients v_0, v_1, v_2. The E_T shown in all the plots are of arbitrary units.

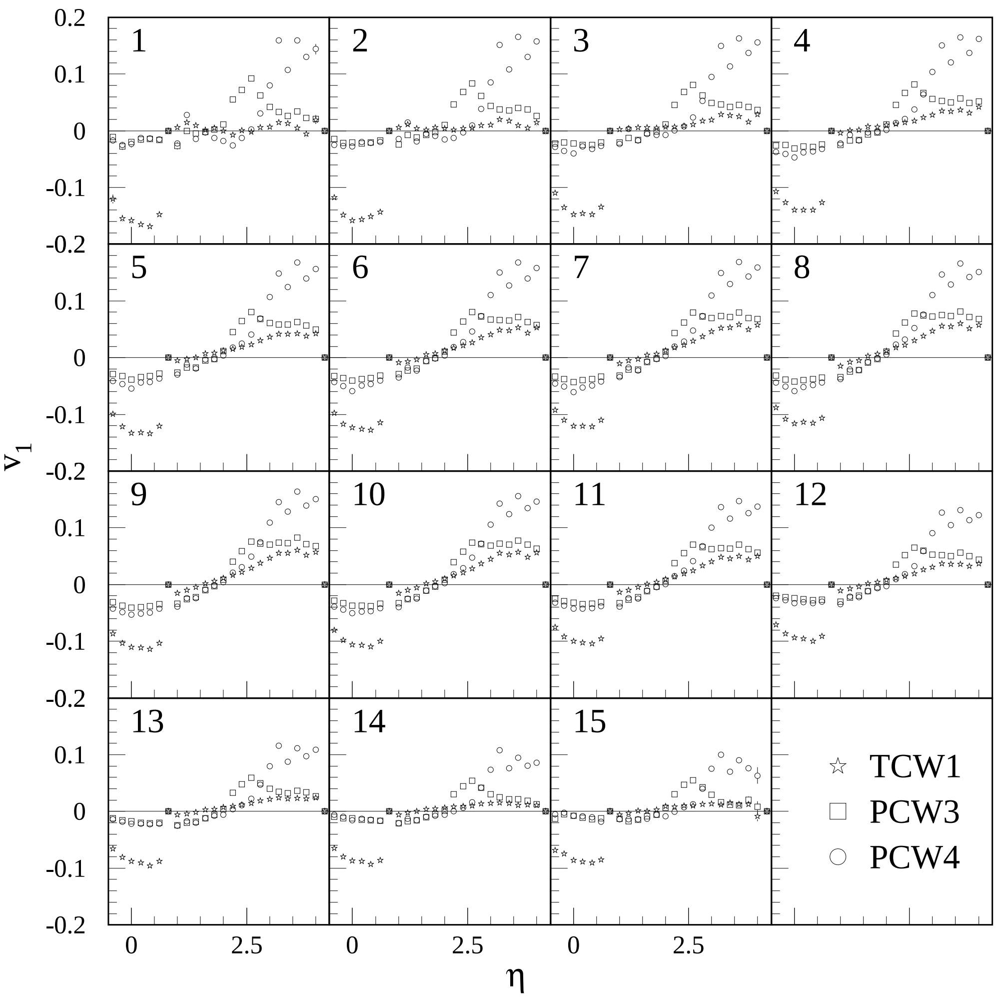

Figure 5.5: The $v_1(\eta)$ of E_T for different PCAL centralities (see Fig. 4.3 for definitions of E_T bins) observed by using the reaction plane determined in the windows of TCW1, PCW3 and PCW4 (see text). An auto-correlation appears when the η bin of v_1 overlaps with the windows where the reaction plane angle is determined.

over a wide η range and the observation of independence of pseudo-rapidity is the same as what was observed in the experiments at BEVALAC [16]. The positive values of v_2 indicate an elliptical event shape with the major axis lying along the reaction plane, which differs from the "squeeze out" (of the reaction plane) observed at lower beam energies [16]. This different event shape may be interpreted as a consequence of an expansion from the almond-like shape participants with less absorption effects from the spectators which move away from the collision zone faster in the time scale of building up of the internal pressure at larger beam energy [39]. The details of how this qualitative change of the elliptical event shape varies with the increasing beam energy will be studied with the RQMD model in Chapter 8. Finally, in Fig. 5.9, we take three large pseudo-rapidity windows used in our previous analysis of event-by-event Fourier decomposition [31] and compare the present results with the previous analysis. The data agree well in the first moments. The deviation at the second moments is possibly due to the assumption in the original analysis that all the moments are of the same fluctuation so that the values were obtained by fitting simultaneously with one common factor of fluctuation.

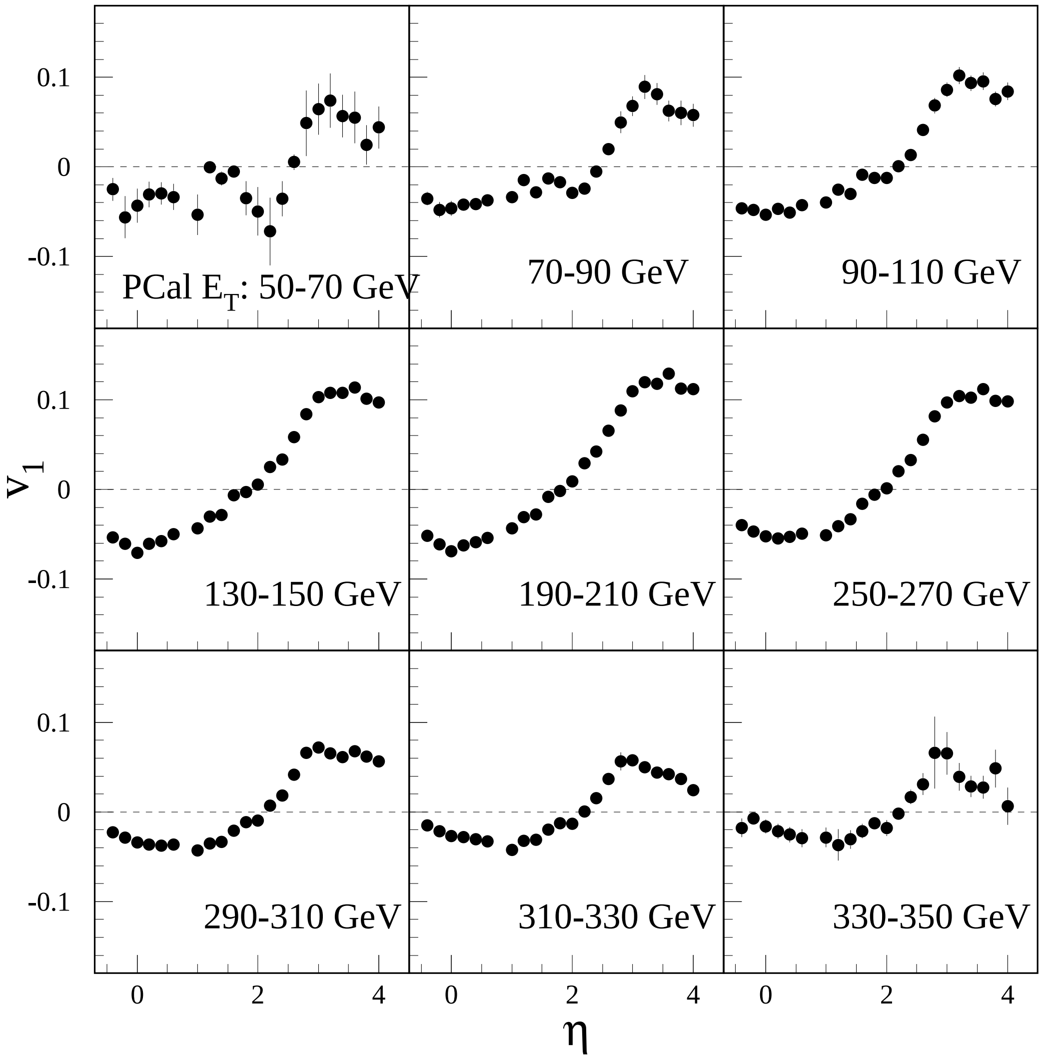

Figure 5.6: The first Fourier moment v_1 of the azimuthal distribution of E_T production with respect to the reaction plane as a function of η for different centralities characterized by PCAL E_T bins. The data are corrected for the reaction plane resolution.

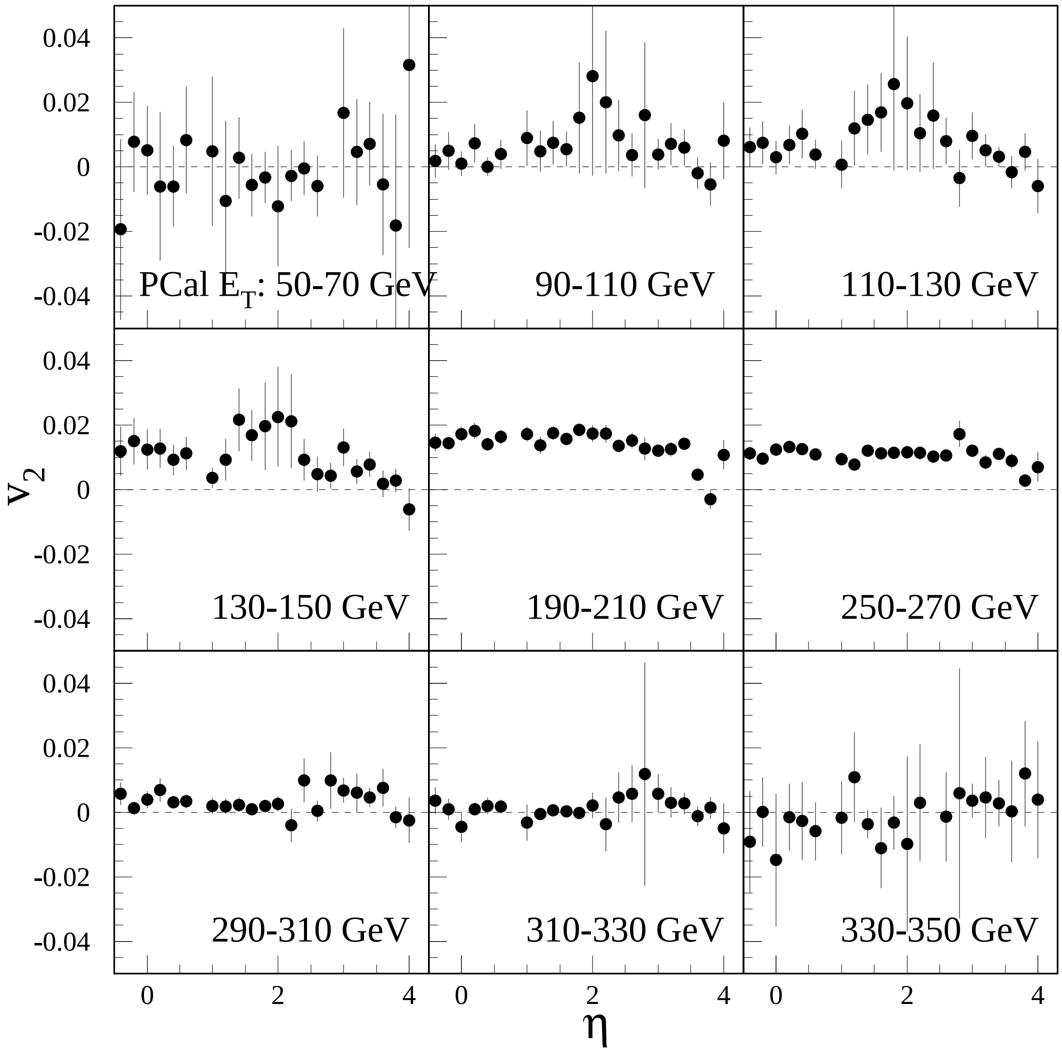

Figure 5.7: The second Fourier moment v_2 of the azimuthal distribution of E_T production with respect to the reaction plane as a function of η for different centralities characterized by PCAL E_T bins. The data are corrected for the reaction plane resolution.

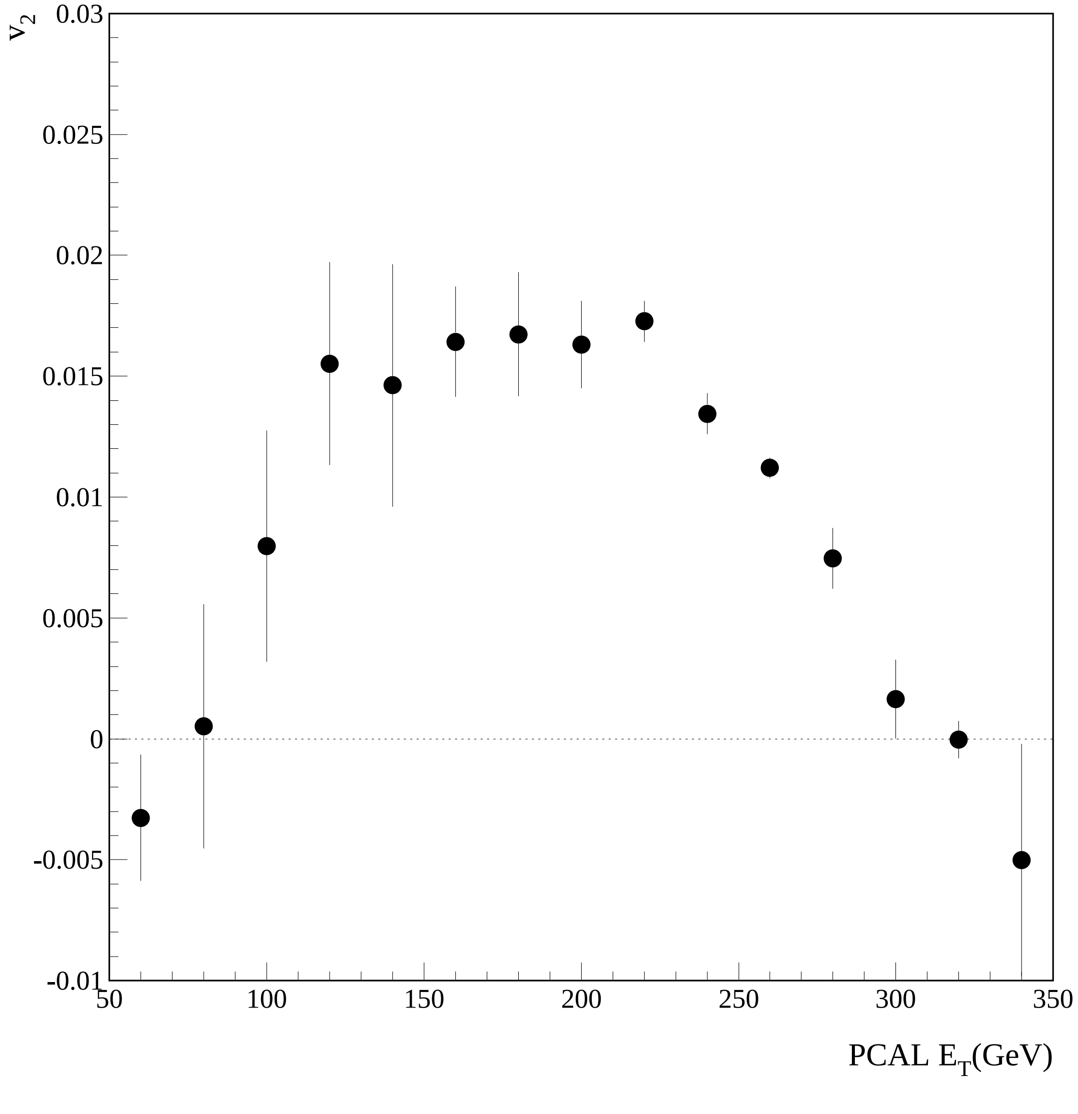

Figure 5.8: The centrality dependence of the second Fourier moment (v_2) of E_T flow at $1.5 < \eta < 2.5$ characterized by PCAL E_T .

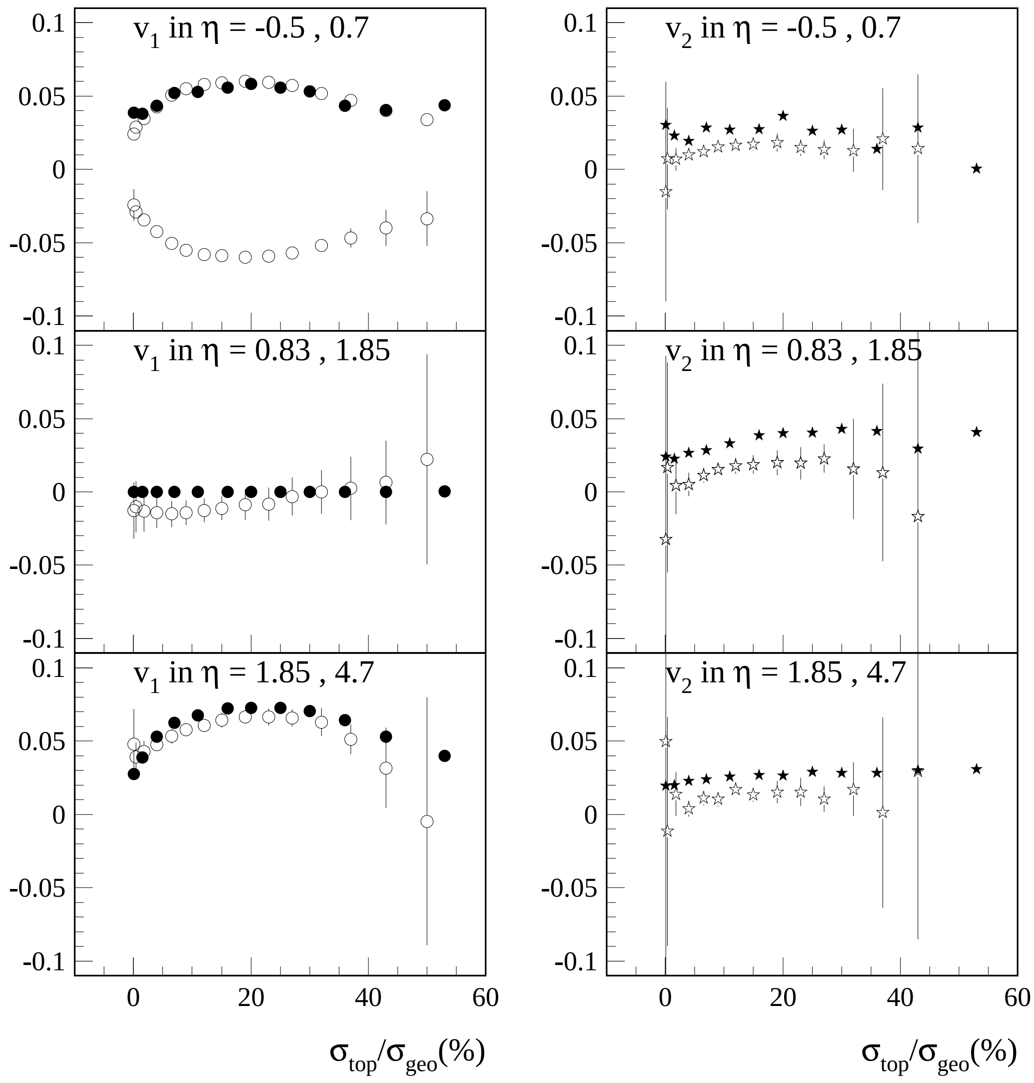

Figure 5.9: Measured Fourier moments in the analysis of Ref. [31](solid symbols) and current analysis(open symbols) in three η windows. The difference in the beam energies in the two analysis is taken into account by comparing them in terms of centrality percentage of the geometric cross section.

Chapter 6

Disentanglement of Nucleon and Pion Flow

In the measurement of transverse energy E_T , there is no distinction between the energy deposited by either a nucleon or a pion. However, in a simultaneous analysis on the flow signals of charged particle multiplicity ($v_1^{N_{ch}}$) and $v_1^{E_T}$, we observe a clear difference between $v_1^{E_T}$ and $v_1^{N_{ch}}$ in the same η region. This difference can be attributed to several factors. First, contributions of nucleons and pions (the two main components at freeze-out at AGS energy) to the E_T and N_{ch} measurements are different as are the pseudo-rapidity distributions. In the E_T case, all species of nucleons and pions deposit energy while only the charged particles contribute in the N_{ch} measurement. At the same time, nucleons and pions may have different collective flow behavior both in magnitude and even in direction. The last and most subtle point is that, even for a single species of charged particles, $v_1^{N_{ch}}$ is sensitive to the asymmetry of particle emission whereas $v_1^{E_T}$ is determined by the transverse energy asymmetry.

So by utilizing the differences between these two flow signals ($v_1^{E_T}$ and $v_1^{N_{ch}}$) and considering only nucleons and pions, we propose the following procedure of disentangling the nucleon and pion flow signals from each other in the mid-η region, where no particle identification is available in our experiment.

Considering the azimuthal distribution of E_T as a function of η and centrality, the sum of contributions from nucleons(n) and pions(π) is given by

$$\frac{dE_T}{d\phi} = \langle E_T\rangle(1 + 2v_1^{E_T}\cos\phi) \tag{6.1}$$

$$= \frac{dE_T}{d\phi}\mid_n + \frac{dE_T}{d\phi}\mid_\pi \tag{6.2}$$

$$= \langle E_T^n\rangle(1 + 2v_1^{E_T,n}\cos\phi) + \langle E_T^\pi\rangle(1 + 2v_1^{E_T,\pi}\cos\phi) \tag{6.3}$$

$$= \quad (\langle E_T^n \rangle + \langle E_T^\pi \rangle)(1 + 2\frac{\langle E_T^n \rangle v_1^{E_T,n} + \langle E_T^\pi \rangle v_1^{E_T,\pi}}{\langle E_T^n \rangle + \langle E_T^\pi \rangle} \cos\phi) \qquad (6.4)$$

and is similarly given by the measurement of charged multiplicity at the same η region

$$\begin{aligned} \frac{dN_{ch}}{d\phi} &= \langle N_{ch} \rangle (1 + 2v_1^{N_{ch}} \cos\phi) && (6.5) \\ &= \frac{dN_{ch}}{d\phi}\mid_n + \frac{dN_{ch}}{d\phi}\mid_\pi && (6.6) \\ &= \langle N_{ch}^n \rangle (1 + 2v_1^{N_{ch},n} \cos\phi) + \langle N_{ch}^\pi \rangle (1 + 2v_1^{N_{ch},\pi} \cos\phi) && (6.7) \\ &= (\langle N_{ch}^n \rangle + \langle N_{ch}^\pi \rangle)(1 + 2\frac{\langle N_{ch}^n \rangle v_1^{N_{ch},n} + \langle N_{ch}^\pi \rangle v_1^{N_{ch},\pi}}{\langle N_{ch}^n \rangle + \langle N_{ch}^\pi \rangle} \cos\phi). && (6.8) \end{aligned}$$

Here the mean is defined as an average over the azimuthal angle ϕ.

So,

$$\begin{aligned} v_1^{E_T} &= \frac{\langle E_T^n \rangle v_1^{E_T,n} + \langle E_T^\pi \rangle v_1^{E_T,\pi}}{\langle E_T^n \rangle + \langle E_T^\pi \rangle} \\ &= a_1 v_1^{E_T,n} + a_2 v_1^{E_T,\pi} && (6.9) \end{aligned}$$

and,

$$\begin{aligned} v_1^{N_{ch}} &= \frac{\langle N_{ch}^n \rangle v_1^{N_{ch},n} + \langle N_{ch}^\pi \rangle v_1^{N_{ch},\pi}}{\langle N_{ch}^n \rangle + \langle N_{ch}^\pi \rangle} \\ &= b_1 v_1^{N_{ch},n} + b_2 v_1^{N_{ch},\pi} && (6.10) \end{aligned}$$

where $v_1^{E_T}$ and $v_1^{N_{ch}}$ are directly measured in the experiment, and a_1 and a_2(b_1 and b_2) are the separate ratios of $\langle E_T^n \rangle$ and $\langle E_T^\pi \rangle$ ($\langle N_{ch}^n \rangle$ and $\langle N_{ch}^\pi \rangle$) for nucleons and pions to the total $\langle E_T \rangle$ ($\langle N_{ch} \rangle$) for a given pseudo-rapidity.

In order to get v_1^n and v_1^π, a few assumptions are needed:

- a_1 and a_2(b_1 and b_2) need the input of the pseudo-rapidity distribution which can be obtained by either mapping from the experimentally-measured rapidity and transverse momentum distributions of protons and charged pions (see Appendix C) or from the predictions of RQMD. The former has the advantage that only experimental data are used, i.e. there is no model dependence. However the measured distributions, although covering the complete phase space, are only available for relatively central collisions. Using the distributions from a model, has the advantage that the proper centrality cut can be applied albeit at the expense of a model-dependent results. The spread of the results due to these two different input distributions is considered as part of the systematic error.

- We assume isospin symmetry in the flow signal, so $v_1^{E_T,n} = v_1^{E_T,proton}$ and $v_1^{E_T,\pi} = v_1^{E_T,charged\ \pi}$. This assumption is found to be reasonable in the RQMD model.

- If we assume the distribution of transverse energy directivity vectors ($\vec{E_T}$), which we use to determine the reaction plane orientation, is a 2-d Gaussian distribution with a slightly shifted center from the origin, for any given species of particles (either nucleon or pion)

$$\frac{dN}{d\vec{E_T}} = \frac{1}{\pi\sigma}\exp\left(-\frac{(\vec{E_T} - \vec{E_T}^0)^2}{\sigma^2}\right),\ |\vec{E_T}^0| \ll \sigma, \tag{6.11}$$

leads to

$$\begin{aligned} v_1^N &= \frac{\int \cos\phi \frac{dN}{d\vec{E_T}} d\vec{E_T}}{\int \frac{dN}{d\vec{E_T}} d\vec{E_T}} & (6.12)\\ &= \frac{|\vec{E_T}^0|\langle|\vec{E_T}|\rangle}{\sigma^2} & (6.13)\\ v_1^{E_T} &= \frac{\int |\vec{E_T}|\cos\phi \frac{dN}{d\vec{E_T}} d\vec{E_T}}{\int |\vec{E_T}| \frac{dN}{d\vec{E_T}} d\vec{E_T}} & (6.14)\\ &= \frac{|\vec{E_T}^0|\langle|\vec{E_T}|^2\rangle}{\langle|\vec{E_T}|\rangle\sigma^2} & (6.15)\end{aligned}$$

where $\langle x\rangle$ means the evaluation of the mean with a 2-d Gaussian probability distribution.

So the ratio of $v_1^{E_T}$ to v_1^N becomes

$$\frac{v_1^{E_T}}{v_1^N} = \frac{\langle|\vec{E_T}|^2\rangle}{\langle|\vec{E_T}|\rangle^2} = \frac{4}{\pi}. \tag{6.16}$$

$v_1^{E_T}/v_1^N$	RQMD 2.3 cascade mode	RQMD 2.3 mean field mode
nucleon	1.398	0.986
pion	1.154	0.854

Table 6.1: Fit of $v_1^{E_T}/v_1^N$ of nucleons and pions in different modes of RQMD(version 2.3) by a constant at the pseudo-rapidity range $0 < \eta < 4$.

We also extracted these ratios for nucleons and pions from RQMD by fitting a constant to the distribution $v_1^{E_T}/v_1^N$ (Table 6.1 and Fig. 6.1). The uncertainty in the results of disentangled nucleon and pion flow results due to the different choices in $4/\pi$ and RQMD-defined ratios are considered as part of the systematic error.

Now the number of unknown quantities in the Eq. 6.9 and, 6.10 are reduced to two, $v_1^{E_T}$ of the nucleons and pions, which can be uniquely determined with two linear equations. The results at mid-centrality, where the directed flow is strongest, are shown in Fig. 6.2. The nucleons exhibit a strong directed flow signal while pions show an opposite but much weaker signal. The error bars shown are the systematic errors in the disentangled due to the assumptions and the uncertainties in the input; on average they are about relative 15% and 50% error for nucleons and pions respectively.

Also shown in Fig. 6.2 is the flow signal predicted by the RQMD model (version 2.3) with and without nuclear mean field potentials. In RQMD, the proton flow is enhanced but still underestimates the data in the region $1.8 < \eta < 2.5$ if a repulsive nucleon mean field potential is included. However, the pion flow is reduced by this mechanism. It appears that the nucleon flow signal is stronger than predicted by either mode of RQMD, while within the errors the pion flow agrees with the prediction by the model running in both cascade and mean field modes. We will make the comparison of the flow signals of identified particles at forward rapidity in the next chapter. The discrepancy is also very obvious if one looks at the comparison of measured $v_1^{E_T}$ and $v_1^{N_{ch}}$ with the equivalent quantities from RQMD shown in Fig. 6.3. In cascade mode, RQMD underestimates the nucleon flow so much that in the backward η, where the distribution of pions gradually dominates over that of nucleons, it predicts a positive value of $v_1^{E_T}$ and $v_1^{N_{ch}}$, qualitatively different from the experimental observation. The agreement is better when the nucleon flow is enhanced by turning on the repulsive mean field potential.

Fig. 6.4 shows the comparison for the second moments $v_2^{E_T}(\eta)$ in the centrality range of 9-13 %. The effect of a mean field potential reduces the strength of the positive v_2 in the cascade mode. In Chapter 8, there will be a discussion about why the enhancement of nucleon directed flow by the mean field potential will result in smaller values of v_2.

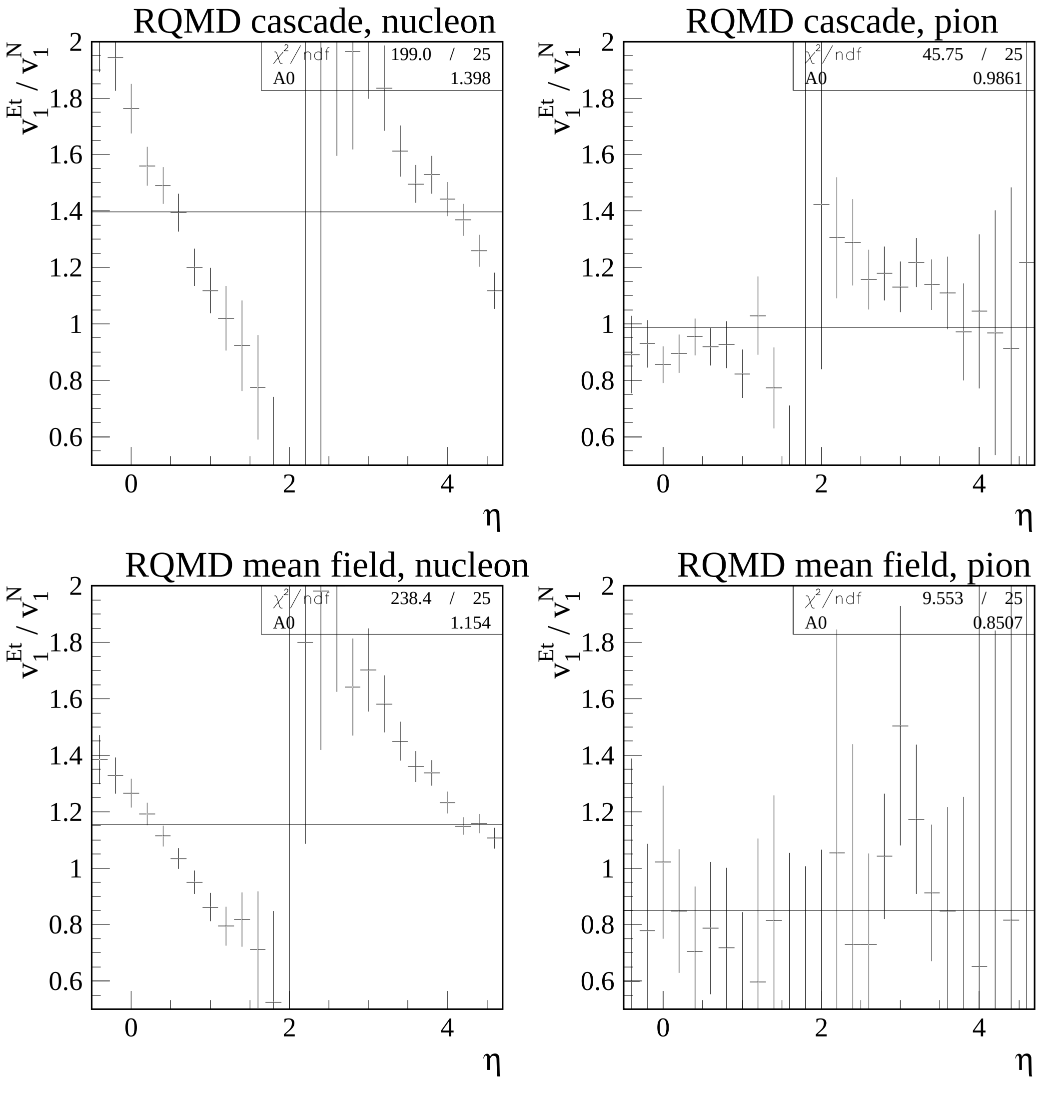

Figure 6.1: The ratio $v_1^{E_T}/v_1^N$ of nucleons and pions from RQMD(version 2.3) together with the fit by a pseudo-rapidity independent constant (the solid line).

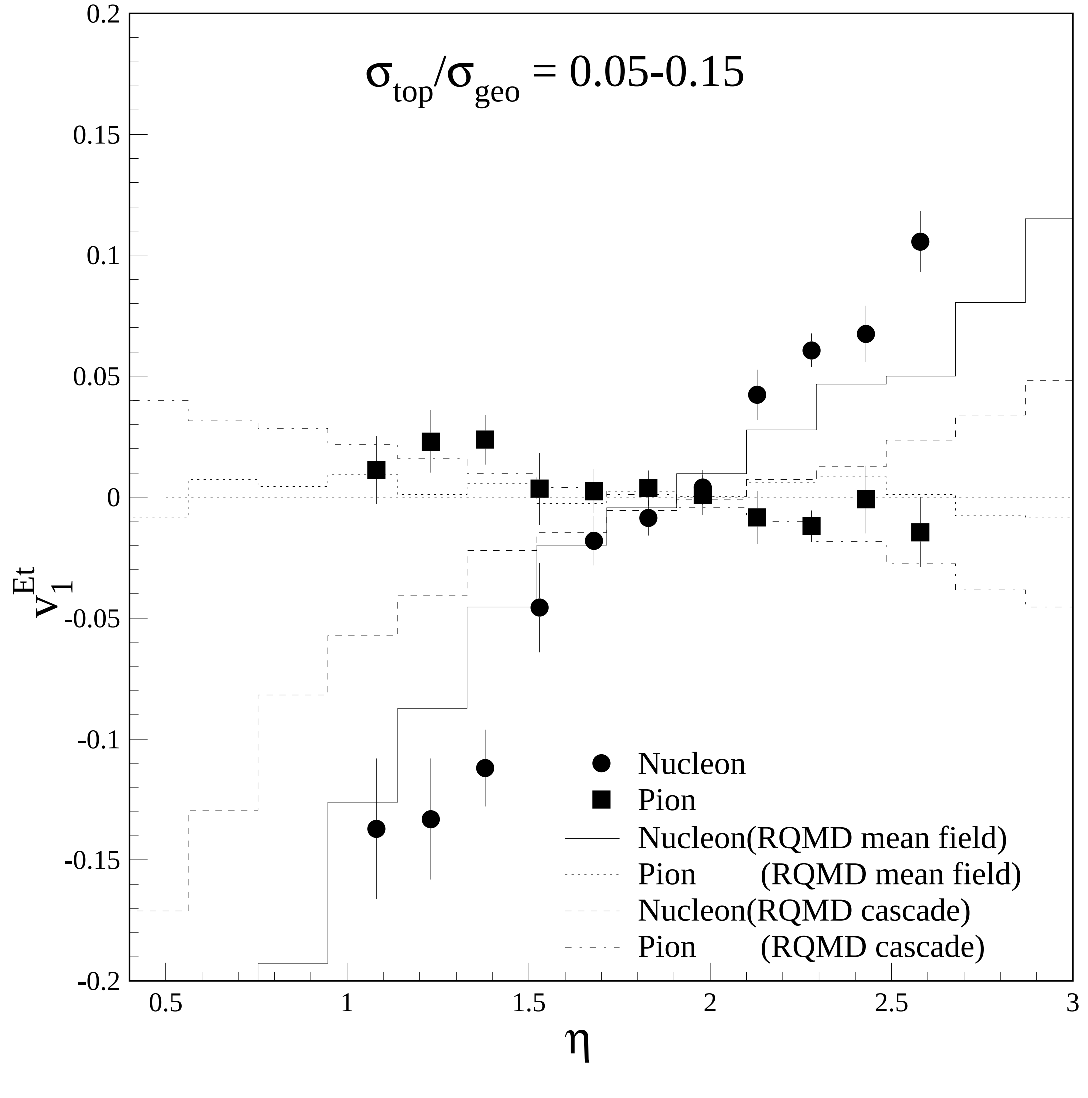

Figure 6.2: Decomposition of the flow parameters $v_1^{E_T}$ of nucleons and pions (solid symbols) and comparison to the extracted parameters from RQMD(version 2.3) in the cascade and mean field modes (lines) for the centrality bin 5-15 %.

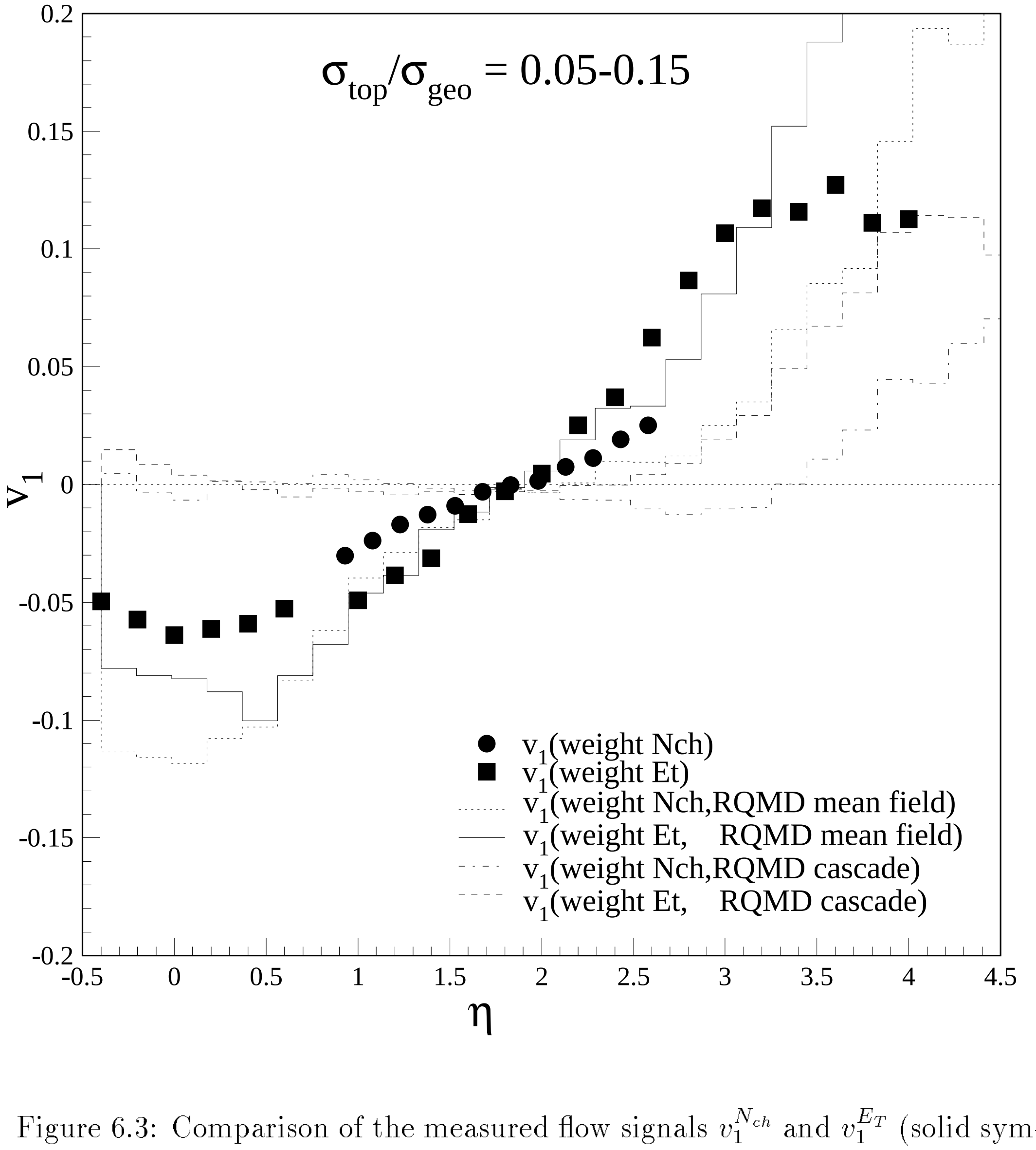

Figure 6.3: Comparison of the measured flow signals $v_1^{N_{ch}}$ and $v_1^{E_T}$ (solid symbols) for the centrality range 5-15 %. Also shown are the equivalent parameters extracted from RQMD(version 2.3) events in the cascade and mean field modes.

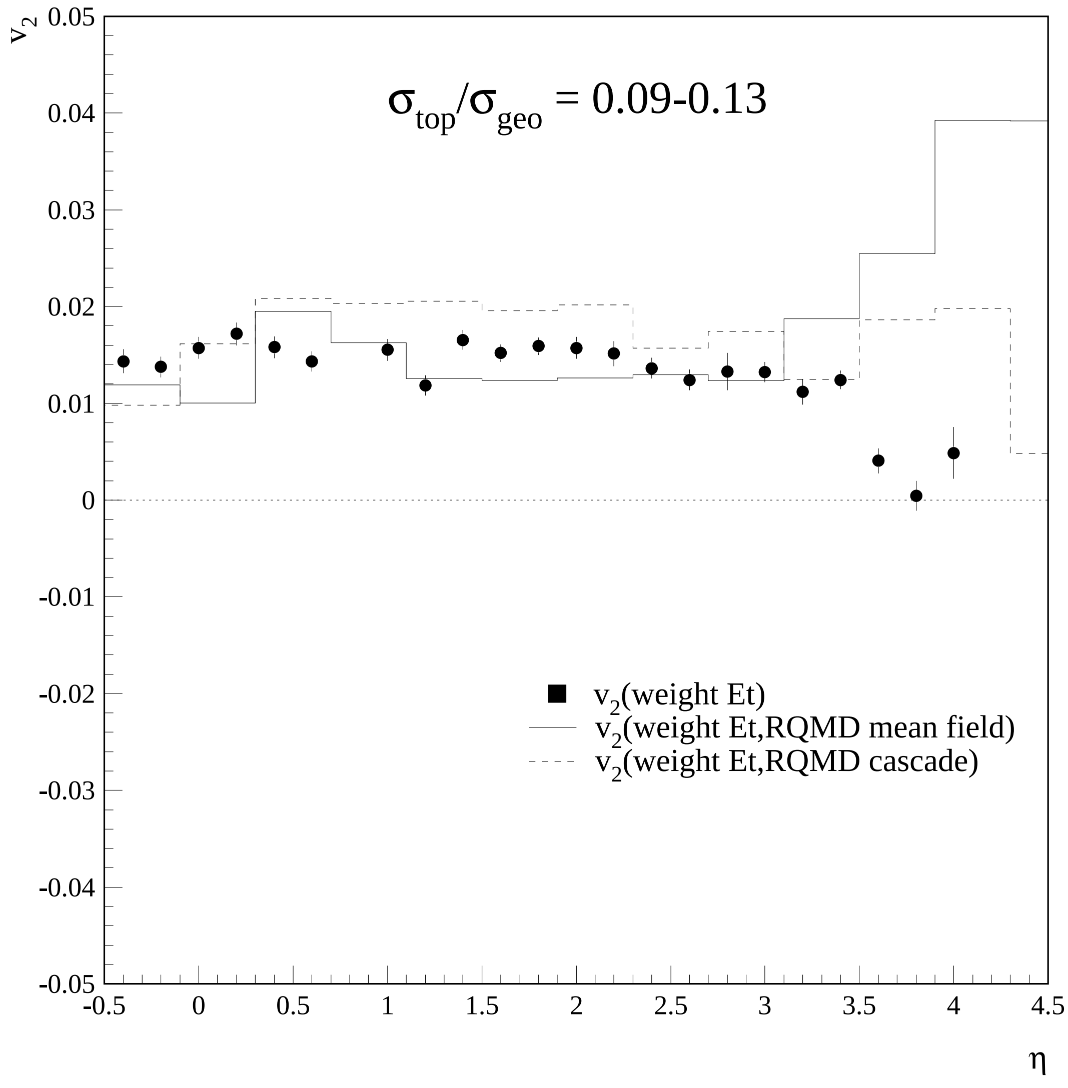

Figure 6.4: Comparison of the measured flow signals $v_2^{E_T}$ (solid symbols) for the centrality range 9-13 %. Also shown are the equivalent parameters extracted from the events of model RQMD (version 2.3) in the cascade and mean field modes.

Chapter 7

Flow of Identified Particles

7.1 Introduction

In this chapter we apply a similar strategy of analysis to measurements on the downstream spectrometer so that the triple differential multiplicities $d^3N\ /\ (dp'_x\ dp'_y\ dy)$ of identified protons and charged pions are reconstructed for the use of studying their flow properties. Here and below we denote with a prime the values in the coordinate system redefined by the reaction plane event by event. For example, the azimuthal angle in this system we denote as $\phi' = \phi - \Psi_R$, where Ψ_R is the reaction plane angle in the laboratory fixed frame.

First we will briefly describe the analysis procedures. Some of the technical details are put in the Appendix D. We then present the results of triple differential multiplicities and related flow signals extracted from them. Among the results shown, the Fourier analysis of the particle azimuthal distributions as a function of transverse momentum is to a large extent independent from the uncertainties in spectrometer efficiency and the detector acceptance. Different flow scenarios are discussed from the point of view of the observed dependence of flow signals on the transverse momentum (p_t) of the particles. Finally, we include the measurements with our estimates of proton and pion flow from charged multiplicity and transverse energy flow as discussed in the previous chapter, and make a comparison with the predictions from two theoretical models RQMD 2.3 [39] and ARC [38].

7.2 Structure of the Analysis

We study the azimuthal anisotropy of particle production by means of Fourier analysis, i.e. the rapidity, transverse momentum, and centrality dependence of Fourier coefficients v_n in the decomposition of the azimuthal distribution with respect to the reaction plane:

$$E\frac{d^3N}{d^3p'} = \frac{d^3N}{p_t dp_t dy d\phi'} \tag{7.1}$$

$$= \frac{1}{2\pi}\frac{d^2N}{p_t dp_t dy}(1+\sum_{n=1}^{\infty} 2v_n\cos(n\phi')). \tag{7.2}$$

In each event the reaction plane angle is determined by the direction of mean transverse energy flow in the TCAL and PCAL as discussed before, and the transverse coordinate system is redefined to make the reaction plane as the new $x-z$ plane. Since the coverage of the calorimeters, used for the reaction plane determination, does not overlap with the spectrometer coverage, we are free from problems related to auto-correlations in the flow analysis of identified particles. The transverse momentums components p_x and p_y of identified particles in each event are mapped into the new coordinate system and the particle distributions are determined with respect to the reaction plane. We have full 2π acceptance in the spectrometer only for very limited p_t range ($p_t \leq 100$ MeV), but the triple differential multiplicity is constructed in full by means of the random orientation of the reaction plane angle over 2π.

In the E877 setup, charged particles emitted in the forward direction and passing through the collimator ($-134 < \theta_x < 16$ mrad, $-11 < \theta_y < 11$ mrad) are analyzed by the magnetic spectrometer. Tracks are reconstructed by the hits in two high resolution drift chambers (DC2 and DC3) and four multi-wire proportional chambers (MWPC). The average momentum resolution is $\Delta p/p \approx 4\%$ in the momentum range considered which is dominated by multiple scattering. A time-of-flight hodoscope located behind the tracking chambers and 12 m from the target, provides the time of flight with approximately 85 ps resolution. The details of the particle identification as well as the correction for the tracking efficiency due to the spectrometer occupancy and the detector geometrical acceptance are discussed in Appendix D and Ref. [57].

7.3 Experimental Results

7.3.1 Triple Differential Cross Sections

In Fig. 7.1, contour plots are shown of the triple differential multiplicities of protons and charged pions measured with respect to the reaction plane in the rapidity slice $3.0 < y < 3.1$ for protons and $3.1 < y < 3.2$ for charged pions.

The overall shift of the proton distribution towards positive p_x is evident. Charged pions are slightly shifted in the opposite direction (negative p_x). The distributions shown are not corrected for the reaction plane resolution.

7.3.2 Directed Flow

From the 2-d distributions (in p_t, ϕ' or p_x, p_y) of the triple differential multiplicity of identified particles, the anisotropy can be observed by three kinds of signals, $v_n(p_t, y)$, $T_B(\phi', y)$, and $\langle p_x \rangle(y)$ as:

- *Fourier Moments* $v_n(p_t, y)$,

$$\frac{dN}{d\phi}(p_t, y) \propto (1 + \sum_{n=1}^{N} v_n \cos(n\phi)) \tag{7.3}$$

- *Inverse slope parameter* $T_B(\phi', y)$,

$$\frac{dN}{p_t dp_t}(\phi', y) = \frac{dN}{m_t dm_t}(\phi', y) \propto m_t \exp(-\frac{m_t}{T_B}) \tag{7.4}$$

- *Mean transverse momentum projected in the direction of the reaction plane* $\langle p_x \rangle(y)$,

$$\frac{1}{N_0} \int \frac{d^3N}{dp'_x dp'_y dy}(p'_x) dp'_x dp'_y = \langle p'_x \rangle \tag{7.5}$$

$v_1(p_t, y)$

We quantify the directed flow by v_1, the first coefficient in Fourier decomposition of the azimuthal particle distribution in Eq. 7.3. Compared with $\langle p_x \rangle(y)$ which is one single integral value of the entire 2-d spectrum at each rapidity, $v_1(p_t, y)$ is more informative and helps to distinguish different flow scenarios as discussed in the next section.

The coefficient v_1 is analyzed as a function of transverse momentum for different rapidity bins and centrality bins of the collision. Four centrality regions, selected according to PCAL E_T: $150 < E_T < 200$, $200 < E_T < 230$, $230 < E_T < 270$, and $E_T > 270$ GeV, correspond to (see Fig. 3.7) $\sigma_{top}/\sigma_{geo}$ values of approximately 23–13%, 13–9%, 9–4%, and <4%, respectively.

The results of the directed flow signal v_1, corrected for the reaction plane resolution, are presented in Fig. 7.2–7.4 for protons and charged pions. The systematic errors are estimated to be about 4% by the Fourier coefficients of

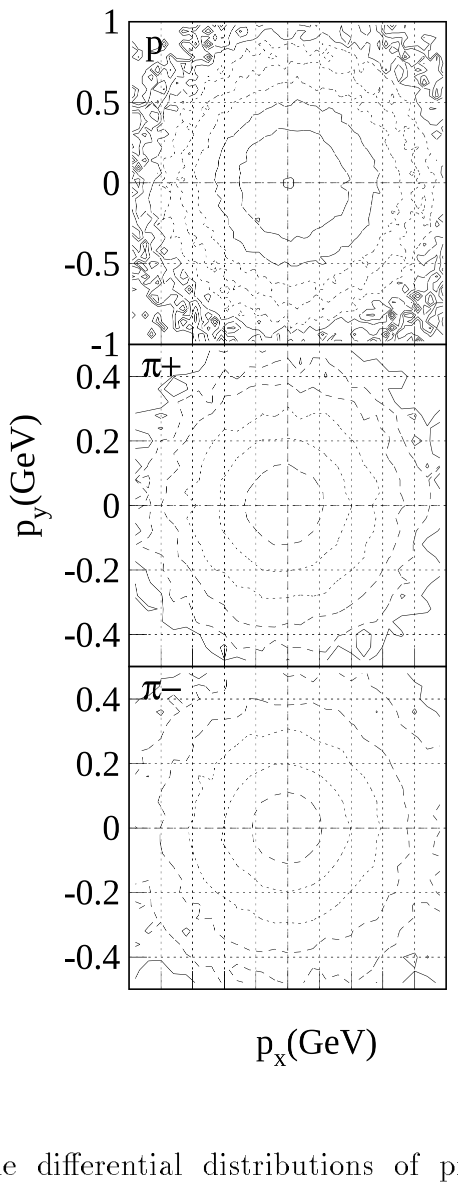

Figure 7.1: Triple differential distributions of protons(top), positive pions(middle) and negative pions(bottom) (rapidity bin $3.0 < y < 3.1$(protons), $3.1 < y < 3.2$(pions)) without correction for the reaction plane resolution.

the $\sin(\phi')$ term which in principle should be zero because of the symmetry. The error bars shown include both statistical and systematic error. The production of protons has a very strong correlation with the orientation of the reaction plane. The magnitude of the anisotropy coefficient v_1 has an almost linear p_t dependence at low and intermediate p_t but seems to saturate towards the higher p_t. In the lowest centrality and very small transverse momentum regions, protons have a tendency to flow in the opposite direction, i.e. negative values of v_1 are observed. This could be an indication of interference with the transverse isotropic expansion [35]. The high statistics data from the 1994 and 1995 runs by E877 will be able to test this idea more precisely.

Positive and negative pions behave quite similarly but different from protons. Both of them exhibit a small "anti-flow" with respect to protons, i.e. the v_1 coefficients have the opposite sign. There is no significant p_t dependence as seen for protons and an average of v_1 is about -0.03. Positive pions of smaller p_t seem to have a larger azimuthal anisotropy than negative pions. This apparent different p_t dependence of the directed flow signals of protons and pions suggests that they might have different mechanisms of developing the collective motion.

The centrality dependence of all flow signals is pronounced and the same as what we observe in the flow of E_T . The coefficients v_1 of pions have the tendency to become more positive toward central collisions. This could be a sign of less absorption from the nucleon spectators and more resonance contribution (see discussion below).

Independent of the flow scenario, $v_1(p_t)$ must vanish at $p_t = 0$, due to the requirement of continuity of the spectra at the origin from all directions. This fact can be used for an estimate of the systematic error in the results of the analysis.

$\underline{T_B(\phi', y)}$

Anisotropic flow can be also characterized by the inverse slope parameter of p_t spectra of particles emitted at different azimuthal angles. We extract this slope by fitting the spectra in the high p_t region ($p_t > 0.3$GeV) by a thermal (Boltzmann) distribution with inverse slope parameter T_B, which shows a dependence on the azimuthal angle ϕ':

$$\frac{d^3N}{p_t\, dp_t\, dy\, d\phi'} = N_0(y)\, m_t \exp(-\frac{m_t}{T_B(\phi')}) \tag{7.6}$$

In Fig. 7.5–7.7, we show the slice of the m_t spectra of protons at different azimuthal angles ϕ', centralities and one specific rapidity rapidity bin. Only

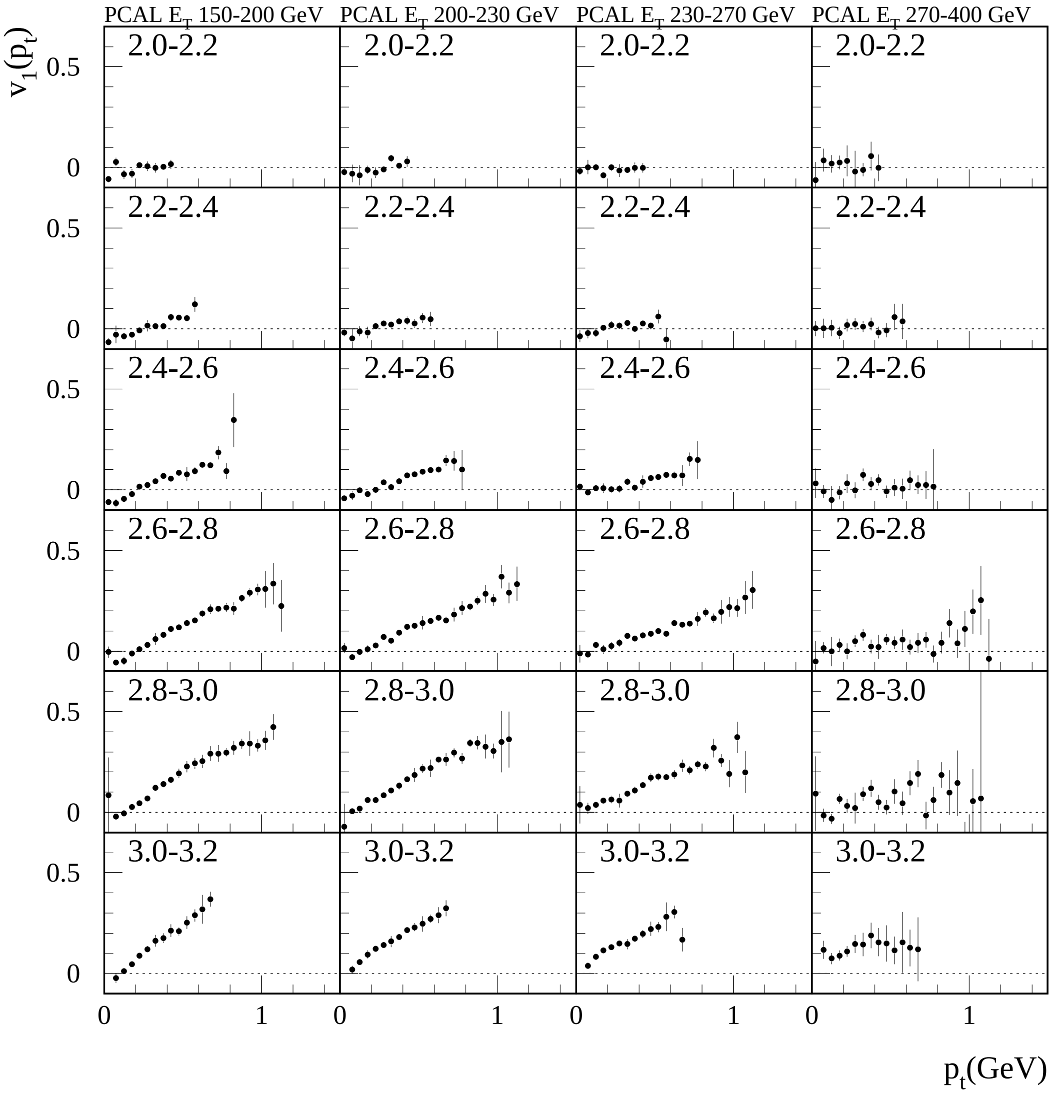

Figure 7.2: The direct flow signal $v_1(p_t)$ of protons for various rapidity bins, starting with $1.6 < y < 2.0$, and for four centrality bins as labeled on top.

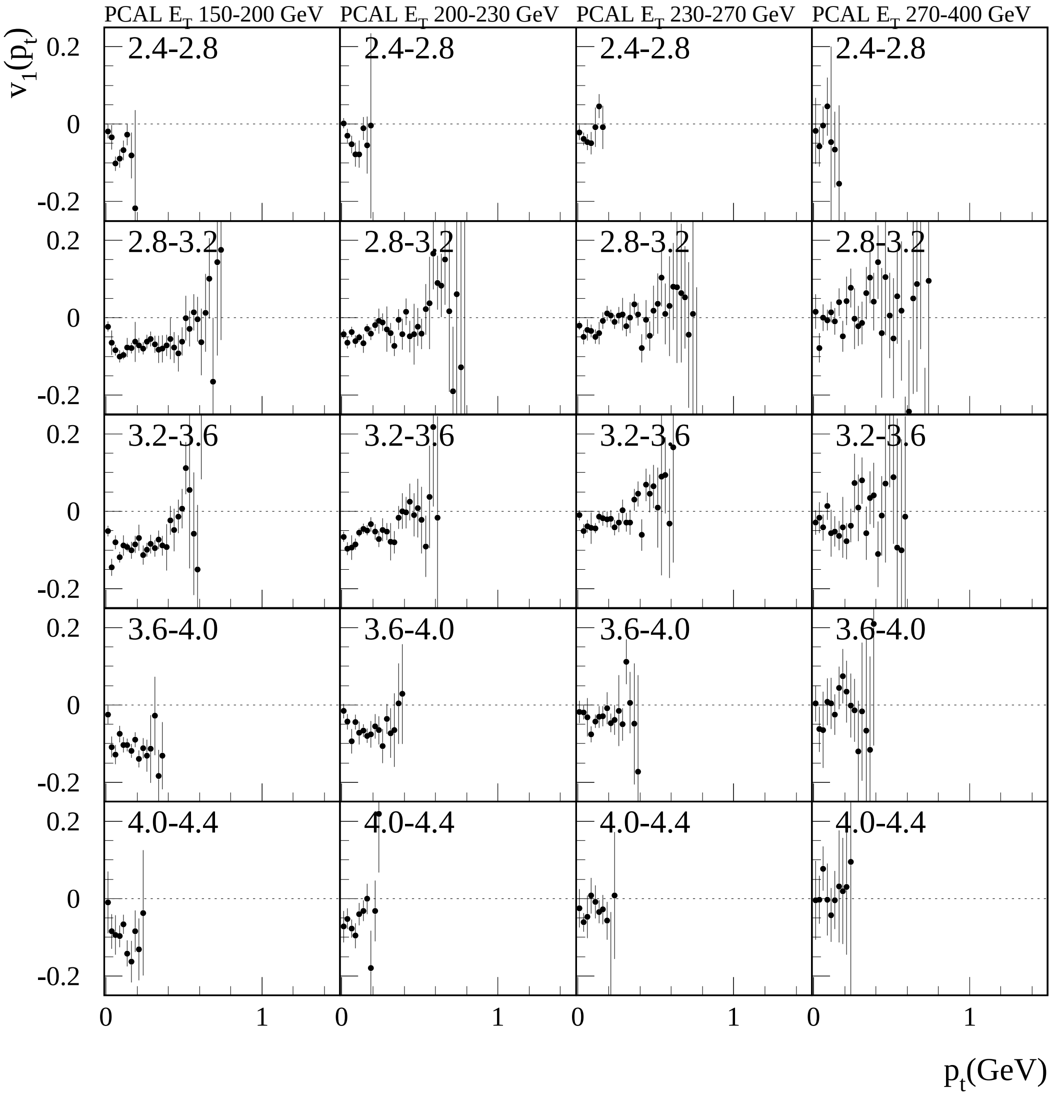

Figure 7.3: The direct flow signal $v_1(p_t)$ of positive pions for various rapidity bins, starting with $2.4 < y < 2.8$, and for four centrality bins as labeled on top.

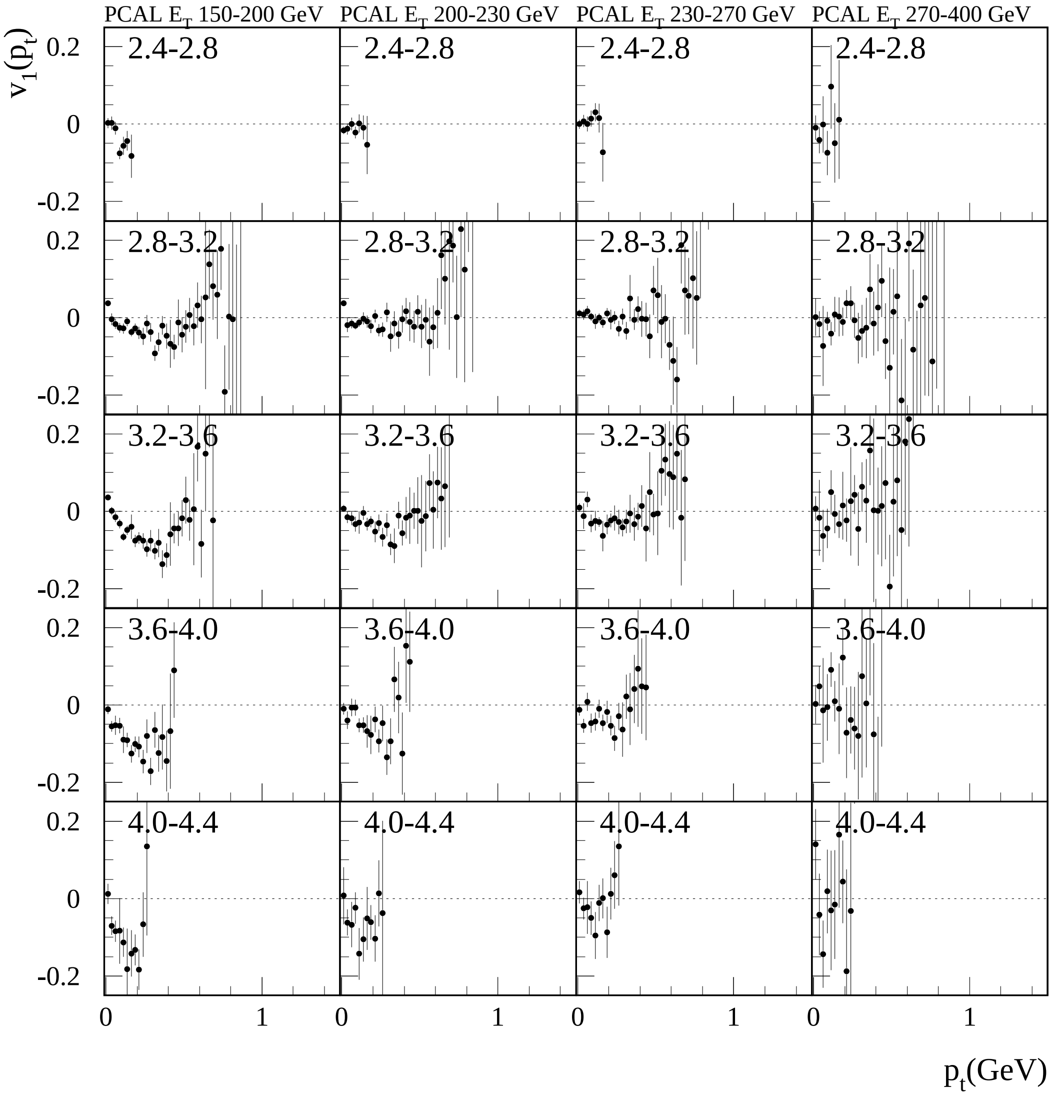

Figure 7.4: The direct flow signal $v_1(p_t)$ of negative pions for various rapidity bins, starting with $2.4 < y < 2.8$, and for four centrality bins as labeled on top.

protons are analyzed in this signal and a reflected symmetry of spectra with respect to $\phi' = 0$ is assumed because of limited statistics. Four bins are used for the region of $\phi' = [0, \pi]$. There exists a strong azimuthal dependence of T_B. For example, in the high p_t regions, proton yields at the same p_t bin are different by one order of magnitude from $\phi' = \pi$ to $\phi' = 0$ for mid-central events. The fitted inverse slope parameter T_B are shown in Fig. 7.8. If we fit this distribution by $\langle T_B \rangle (1 + 2\, a\, \cos(\phi'))$, the mean value $\langle T_B \rangle$ turns out to be very close to the fitted T_B from the ϕ' integrated spectra. This agreement is true only when the directed flow is small, otherwise this effect will distort the ϕ integrated spectra to be of non-Boltzmann shape. So in our case, $\langle T_B \rangle$ is mainly determined by the transverse isotropic flow and the longitudinal expansion [14], and the directed flow generates the azimuthal dependence with respect to the orientation of the reaction plane.

$\underline{\langle p_x \rangle (y)}$

This is the most widely used signature of the directed flow. The simplicity is that it is one single value for each rapidity bin. However, more detailed information gets concealed in the integral and it suffers from the acceptance of the experiment. In Fig. 7.9, we show the measured results of $\langle p_x \rangle (y)$ after the correction for the reaction plane resolution and the evaluation of the average is within the experimental acceptance (see Appendix D). The rapid decrease of $\langle p_x \rangle$ towards mid-rapidity reflects the quickly narrowing p_t acceptance.

In order to get the $\langle p_x \rangle (y)$ for all p_t, we need to make an extrapolation by assuming a parameterization of the triple differential distributions at a fixed rapidity $(d^2N/dp'_x dp'_y)$ and performing fitting procedures to extract $\langle p_x \rangle (y)$ over the full acceptance.

$$\begin{aligned}
\langle p_x \rangle &= \frac{1}{N_0} \int \frac{d^2N}{dp'_x dp'_y} (p'_x)(dp'_x dp'_y) && (7.7) \\
&= \frac{1}{N_0} \int \frac{d^2N}{p_t dp_t d\phi'} (p_t \cdot \cos(\phi'))(p_t dp_t d\phi') && (7.8) \\
&= \frac{1}{N'_0} \int \frac{dN'}{dp_t} (v_1(p_t) \cdot p_t) dp_t && (7.9)
\end{aligned}$$

There are two functional forms to parameterize $d^2N/dp'_x dp'_y$ in each rapidity bin:

$$d^2N/dp'_x dp'_y \quad \propto \quad m_t \exp\left(-\frac{\sqrt{(p'_x - p^0_x)^2 + p'^2_y + m^2}}{T_B}\right) \qquad (7.10)$$

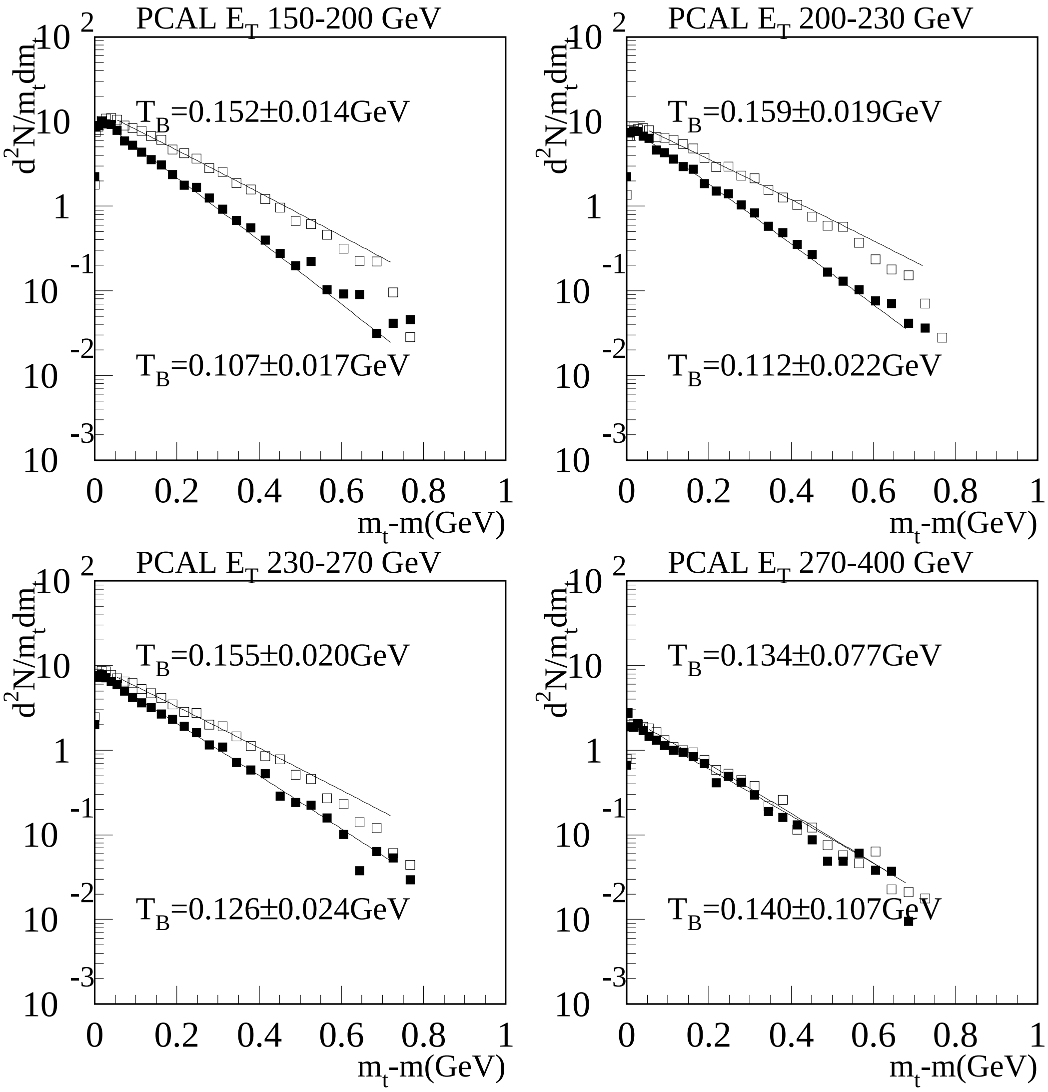

Figure 7.5: The azimuthal dependence of transverse spectra for protons at $2.8 < y < 2.9$. The four plots are at different centralities labeled by PCAL E_T. The solid and open symbols represent the spectra for the slices $3\pi/4 < \phi' < 5\pi/4$, and $-\pi/4 < \phi' < \pi/4$, respectively.

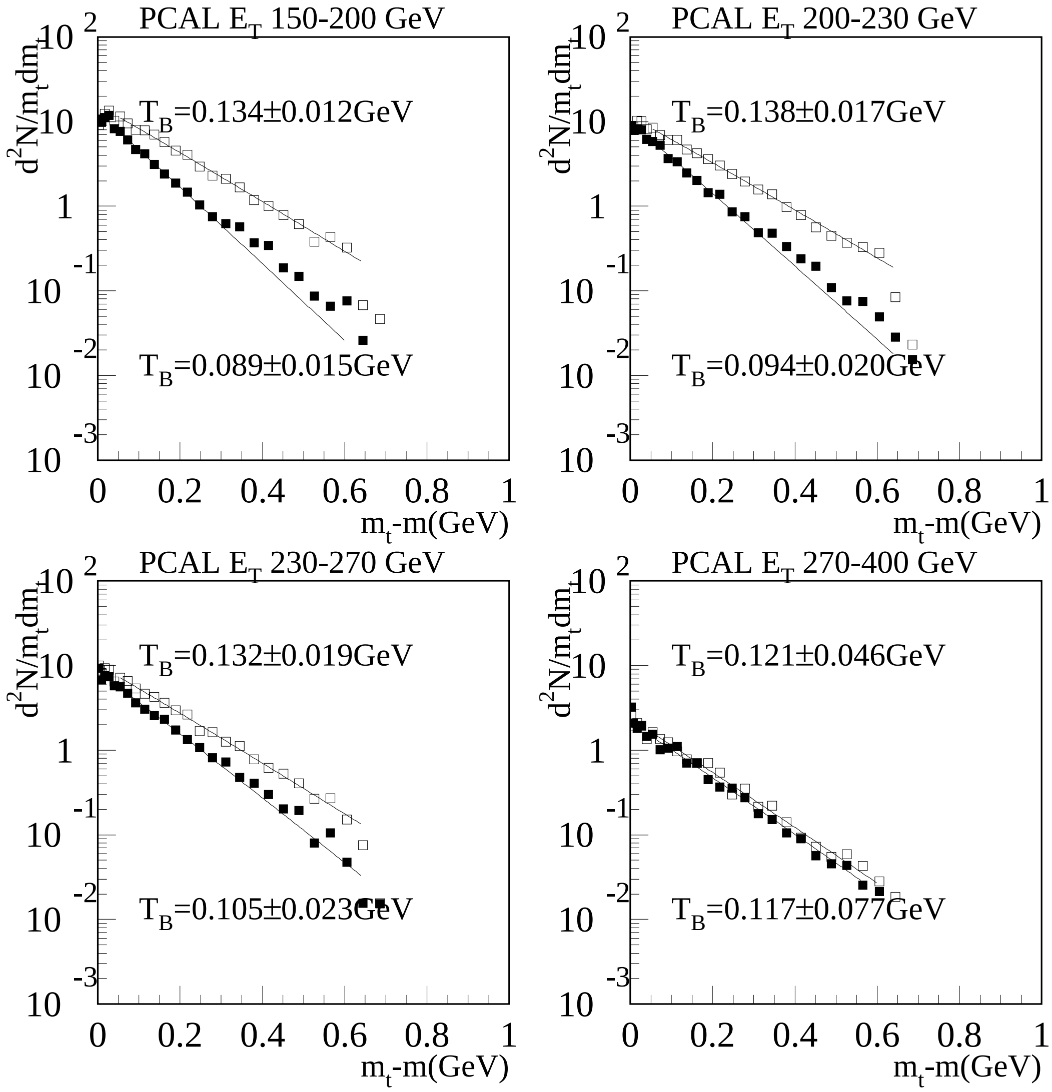

Figure 7.6: The azimuthal dependence of transverse spectra for protons at $2.9 < y < 3.0$. The four plots are at different centralities labeled by PCAL E_T. The solid and open symbols represent the spectra for the slices $3\pi/4 < \phi' < 5\pi/4$, and $-\pi/4 < \phi' < \pi/4$, respectively.

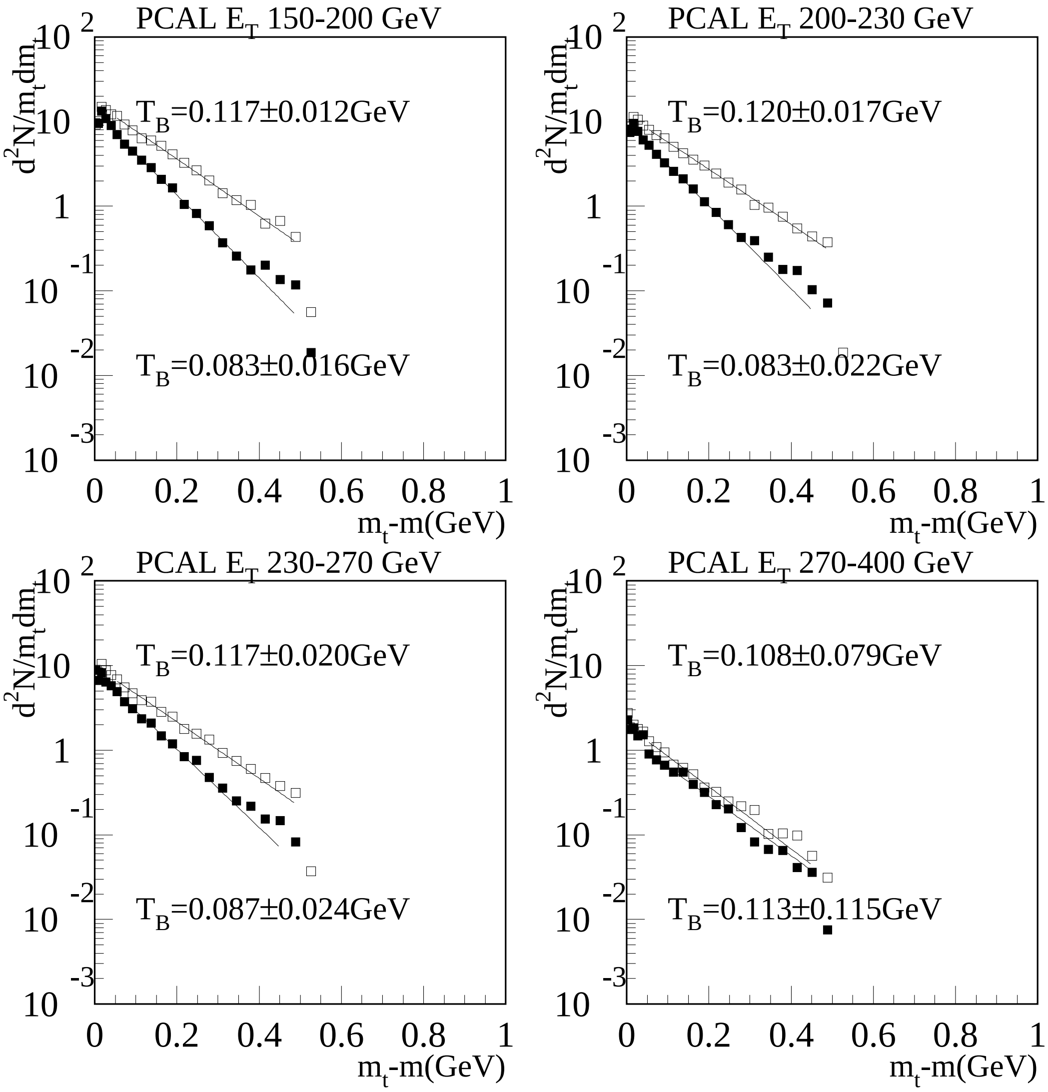

Figure 7.7: The azimuthal dependence of transverse spectra for protons at $3.0 < y < 3.1$. The four plots are at different centralities labeled by PCAL E_T. The solid and open symbols represent the spectra for the slices $3\pi/4 < \phi' < 5\pi/4$, and $-\pi/4 < \phi' < \pi/4$, respectively.

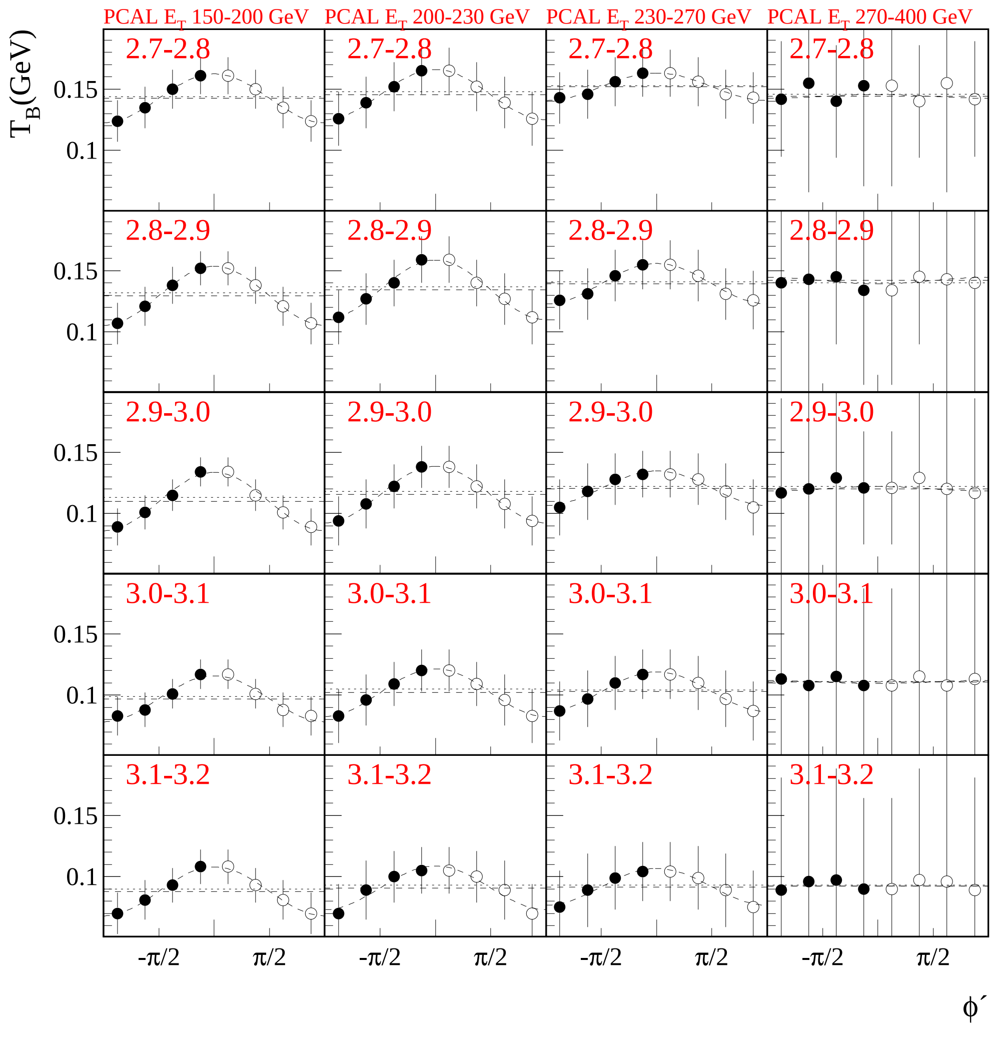

Figure 7.8: The azimuthal dependence of the inverse slope parameter T_B for protons in various centrality and rapidity bins. Symmetry with respect to $\phi' = 0$ is asummed and the open symbols are the reflected values. The horizontal dashed lines are the fitted averaged values $\langle T_B \rangle$ of a first order Fourier series and the dotted lines are the fitted values T_B of the ϕ integrated spectra.

and,

$$d^2N/dp'_x dp'_y \quad \propto \quad E^* e^{-E^*/T}, E^* = \gamma E - p_t \beta_x \gamma \cos(\phi') \qquad (7.11)$$

where E is the energy of particles in the rest frame of the emitting source.

The first parameterization is a simple and straightforward guess based on a thermal distribution with its center shifted from origin due to the directed flow. The second one results from a picture of a transversely boosted thermal source and will be discussed in Sec 7.4.1. The behavior of v_1 as a function of p_t for the above functions of different sets of parameters is shown in Fig. 7.10. Based on the observation for $v_1(p_t)$ of protons and charged pions, these parameterizations are only valid for protons whose v_1 has a strong dependence on p_t. Therefore, we only use the above two parameterizations to extrapolate $\langle p_x \rangle$ over the full acceptance for protons.

The fit procedure can be done by either a direct 2-d fit on $d^2N/dp'_x dp'_y$ at a fixed rapidity with two parameters or two separate one dimensional(1d) fits on dN/dp_t and $v_1(p_t)$ following with an evaluation of $\langle p_x \rangle$ using Eq. 7.9. These two approaches are found to be consistent, however the one with 1d fits is found to be better because of the following reasons:

- The fitting procedure is less affected by the limited p_t acceptance.
- It is easy to check the quality of fitting in 1d fits.
- It is possible to correct for the reaction plane resolution in advance in $v_1(p_t)$ before the fit. The $d^2N/dp'_x dp'_y$ without the correction for the reaction plane resolution corresponds to the proposed 2-d parameterization convoluted with the finite reaction plane resolution, a complicated formulation.

So we first fit the ϕ integrated transverse spectra dN/dp_t by a Boltzmann distribution to get the inverse slope parameter T_B, listed in Table. 7.1. To extract another parameter (e.g. p_x^0 in Eq. 7.10 or β_x in Eq. 7.11), we fit the measured first Fourier moment as a function of transverse momentum $v_1(p_t)$ with the numerical calculation of $v_1(p_t)$ from the parameterizations with $T = T_B$. The quality of the fit can be seen in Fig. 7.11. Finally we evaluate $\langle p_x \rangle$ by Eq. 7.9. In constructing dN/dp_t, the weight from the considerations of the geometrical acceptance and occupancy correction in the spectrometer is taken into account for each track (see Appendix D). Only the weight of the occupancy correction is needed to evaluate $v_1(p_t)$ because it is not affected by the weights of the geometrical acceptance correction which are the same for the tracks of equal p_t.

rapidity	T_B(GeV)	rapidity	T_B(GeV)
2.0-2.1	0.300±0.050	2.7-2.8	0.147±0.003
2.1-2.2	0.270±0.050	2.8-2.9	0.136±0.004
2.2-2.3	0.257±0.050	2.9-3.0	0.120±0.003
2.3-2.4	0.224±0.023	3.0-3.1	0.106±0.004
2.4-2.5	0.203±0.013	3.1-3.2	0.094±0.002
2.5-2.6	0.177±0.004	3.2-3.3	0.084±0.007
2.6-2.7	0.165±0.003	3.3-3.4	0.083±0.008

Table 7.1: The inverse slope parameters T_B of protons from the ϕ integrated transverse spectra.

The extracted values of $\langle p_x \rangle$ from two parameterizations are shown in Fig. 7.12 and the difference between the two parameterizations (filled and open points) can be used as an estimate of the systematic uncertainty. The contribution from the non-measured part of the spectra to $\langle p_x \rangle$ is relatively small at beam rapidity (less than 10%), where the acceptance in p_t is wide. At rapidity around $y = 2.6$ this contribution accounts for about 40% of the value of $\langle p_x \rangle$. The error bars shown do not include the uncertainty in the effective slope parameters used for the spectra extrapolation which is relatively 5% in the maximum.

Finally for proton we take the weighted mean of $\langle p_x \rangle$ obtained from these two parameterizations and evaluate the errors by including the spread of two results and the uncertainty of T_B. And for pions, we estimate that the incompleteness in p_t acceptance can introduce at most 20% error because of the decreasing T_B toward large rapidities, so that we evaluate the $\langle p_x \rangle$ of pions by their values within our acceptance and put the uncertainty into the associated error bars. The $\langle p_x \rangle$ is shown as a function of rapidity y and compared to the disentangled nucleon flow (Sec. 7.4.2) and the model predictions (Sec. 7.4.3) in Fig. 7.20.

7.3.3 Higher Harmonics in Azimuthal Distributions

Higher harmonics (v_2 and v_3) are also analyzed in the particle azimuthal distributions. The accuracy in the evaluation of the contribution of higher harmonics deteriorates with increasing harmonic order due to the limited reaction plane resolution (see Fig. 4.3). This results in larger relative errors(about 50% for v_2 and 100% for v_3). To estimate systematic errors we utilize the same

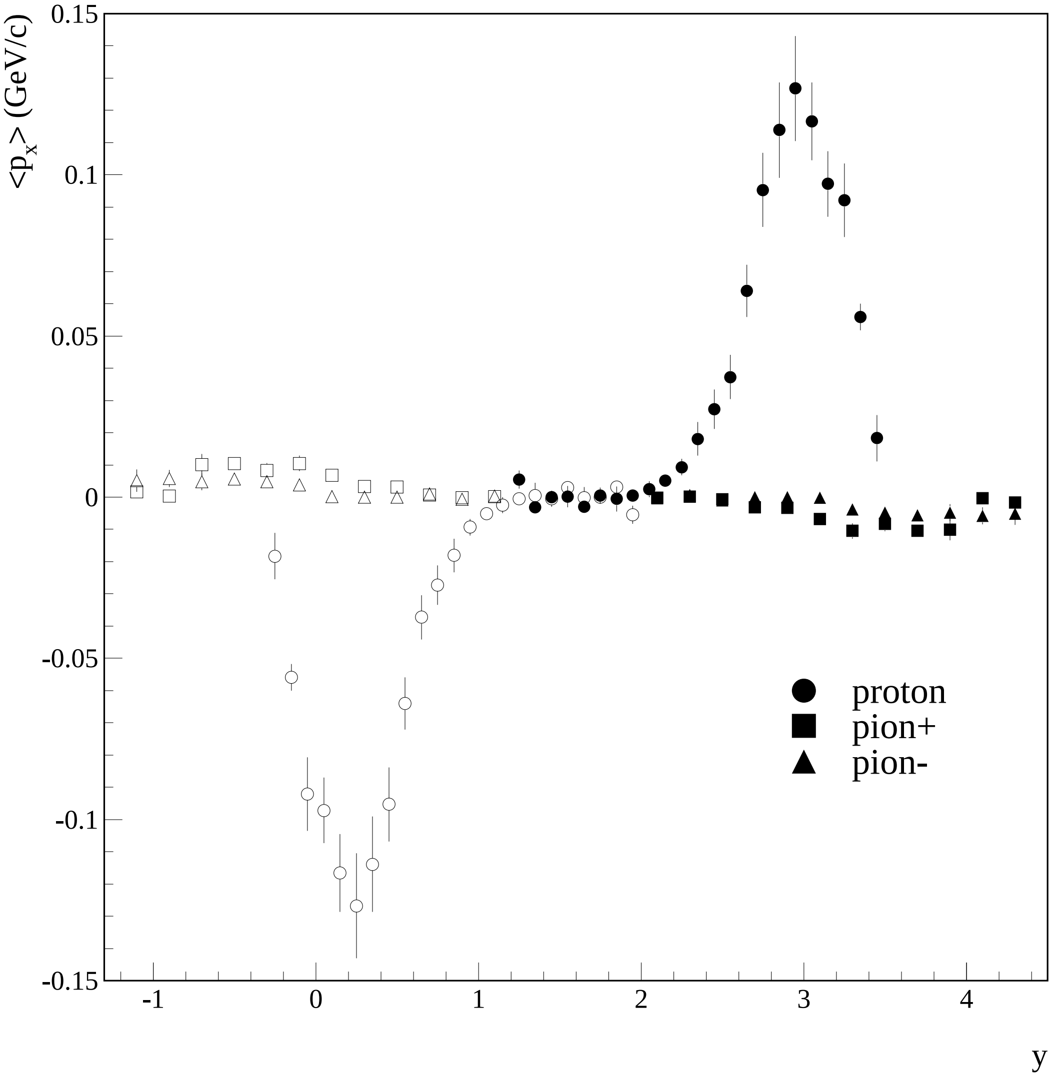

Figure 7.9: The mean transverse momentum component in the reaction plane $\langle p_x \rangle (y)$ of protons and charged pions. The average is evaluated in the experimental acceptance. The correction for the reaction plane resolution has been performed.

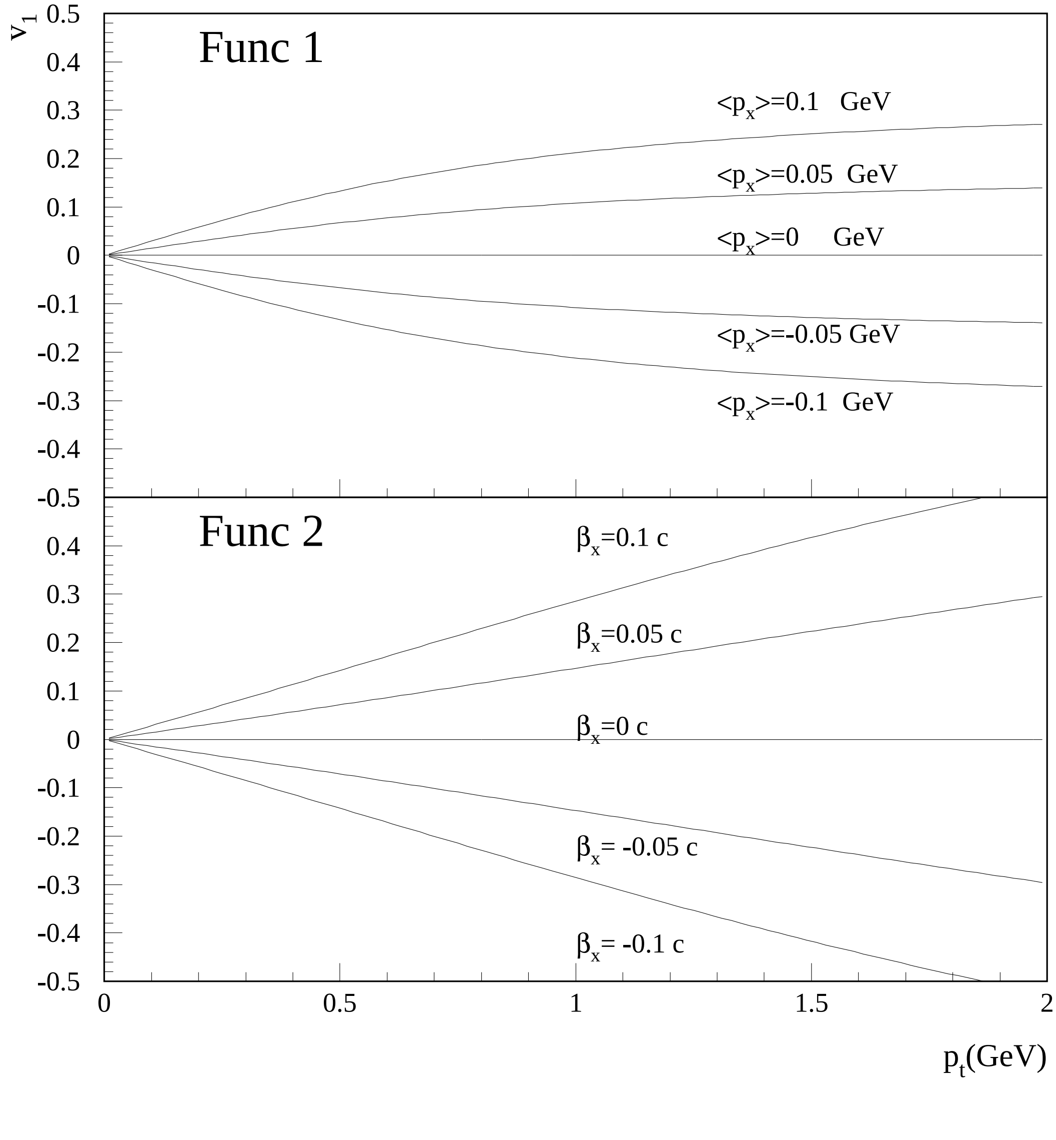

Figure 7.10: The $v_1(p_t)$ of the functional forms described in the text for different sets of parameters. "func1"("func2") corresponds to Eq. 7.10(7.11).

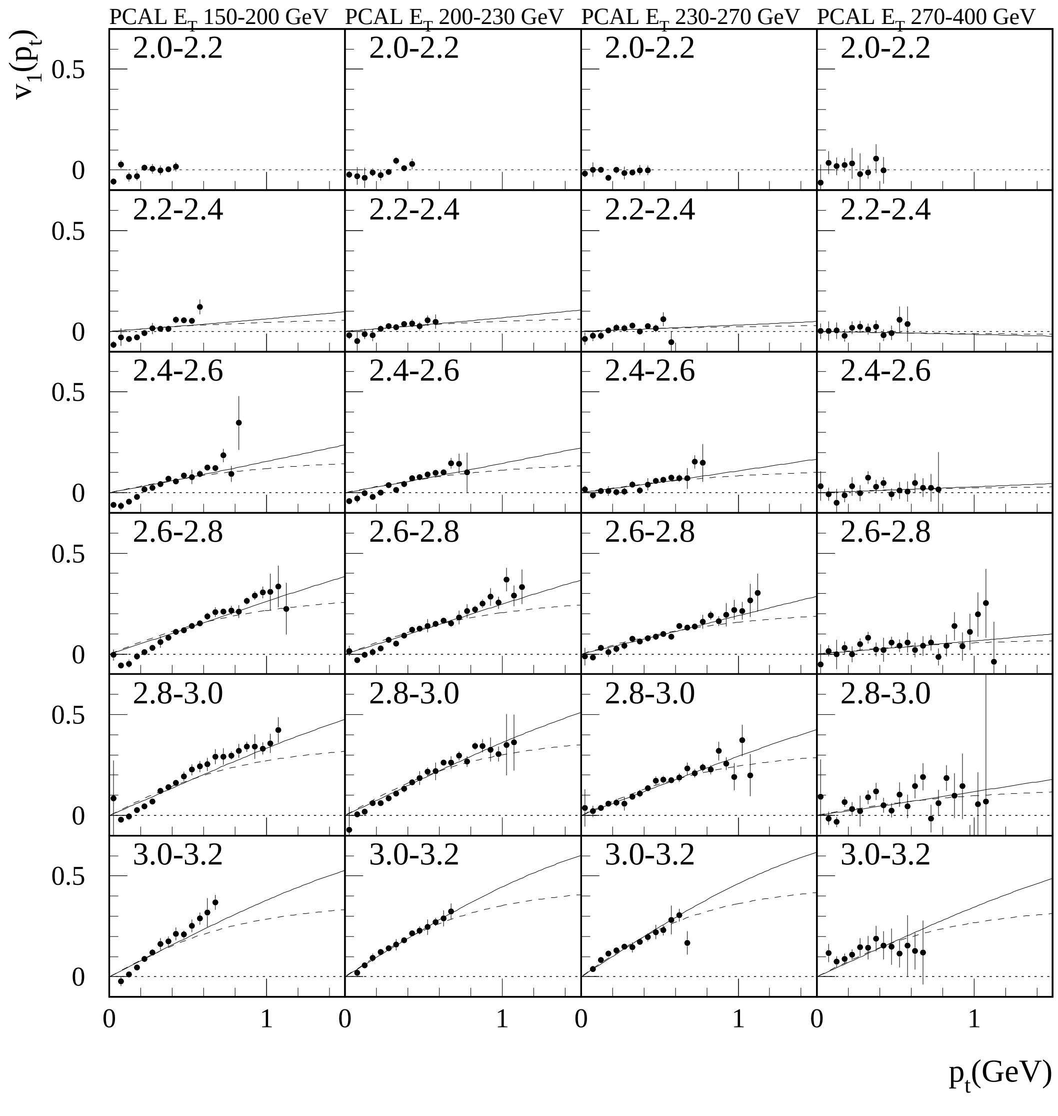

Figure 7.11: The fit of $v_1(p_t)$ of protons by two parameterizations. The dashed(solid) line represents a parameterization according to Eq. 7.10(7.11).

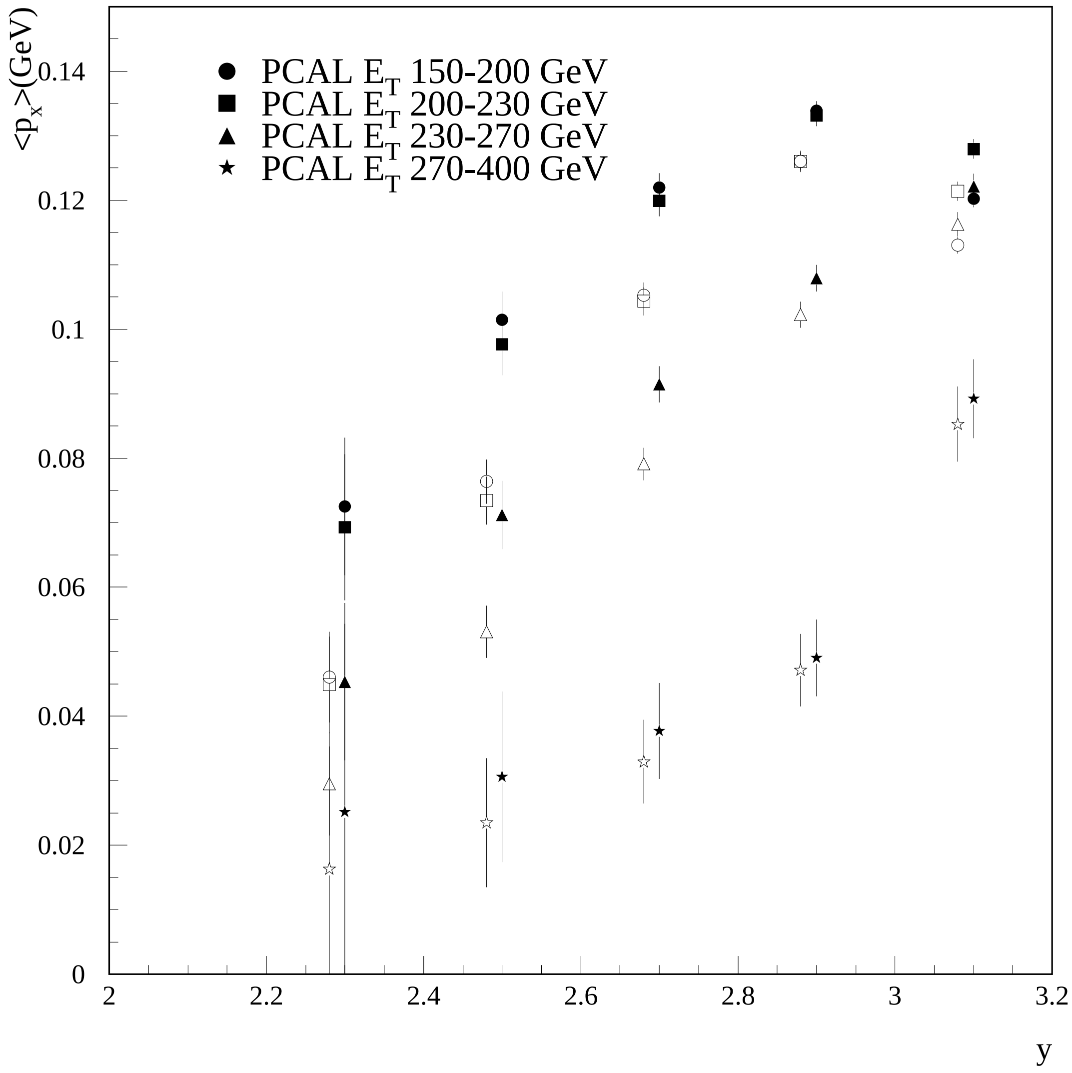

Figure 7.12: The extracted $\langle p_x \rangle(y)$ of protons in the fit of $v_1(p_t)$ by the assumed functional forms. The open(solid) symbols correspond to the values fitted by Eq. 7.10(7.11).

method as was used for v_1.

In the case of v_2 (Fig. 7.13–7.15), only protons have a clear nonzero signal while that of pions is consistent with zero. Possibly due to the limited p_t acceptance we do not observe a significant v_2 signal of protons in the rapidity region $y < 2.4$; however, toward the beam rapidity a clear signal is observed in the high p_t region where v_2 is larger for protons of higher p_t which has been seen in the spectra of pions at lower energies [21]. It should be noted that the orientation of the enhancement is in the direction of the reaction plane. A possible interpretation is that the geometry of the collision zone is of an upright almond shape where less matter lies along the x axis (defined as the direction of the reaction plane) than in the orthogonal direction. Particles which are emitted along the the x axis from the collision zone or of higher transverse momenta p_t will have less probability of getting re-scattering. Then an expansion of the collision zone without absorption will lead to more particles going into the reaction plane (x axis) than out of the reaction plane and those of higher p_t show larger azimuthal anisotropy. However, it should be noted that what we measured is always a time-integrated quantity. Therefore a measurement of positive v_2 does not show that the absorption by the nuclear spectator, which make v_2 become negative, no longer exists in the collision. Instead the in-plane expansion, happening in the later stage after the spectators fly away, turns out to be more important in the collisions at higher beam energies. We will discuss this effect further in the framework of RQMD in Chapter 8.

For protons and pions, at all rapidities and centralities of the collision, the signals of the third Fourier moment v_3 are consistent with zero within the experimental errors and are shown in Fig. 7.16-7.18.

7.4 Discussion

7.4.1 Boosted Thermalized Source *vs* Absorption

The p_t dependence of the v_1 of protons can be interpreted with a picture of a transversely boosted thermal source [35]. The invariant distribution of a static thermal source is described by the Boltzmann distribution,

$$\frac{1}{m_t}\frac{dN}{dm_t dy d\phi'} \propto E^* e^{-E^*/T}, \tag{7.12}$$

where T is the temperature of the source, and E^* is the particle energy in the source rest frame.

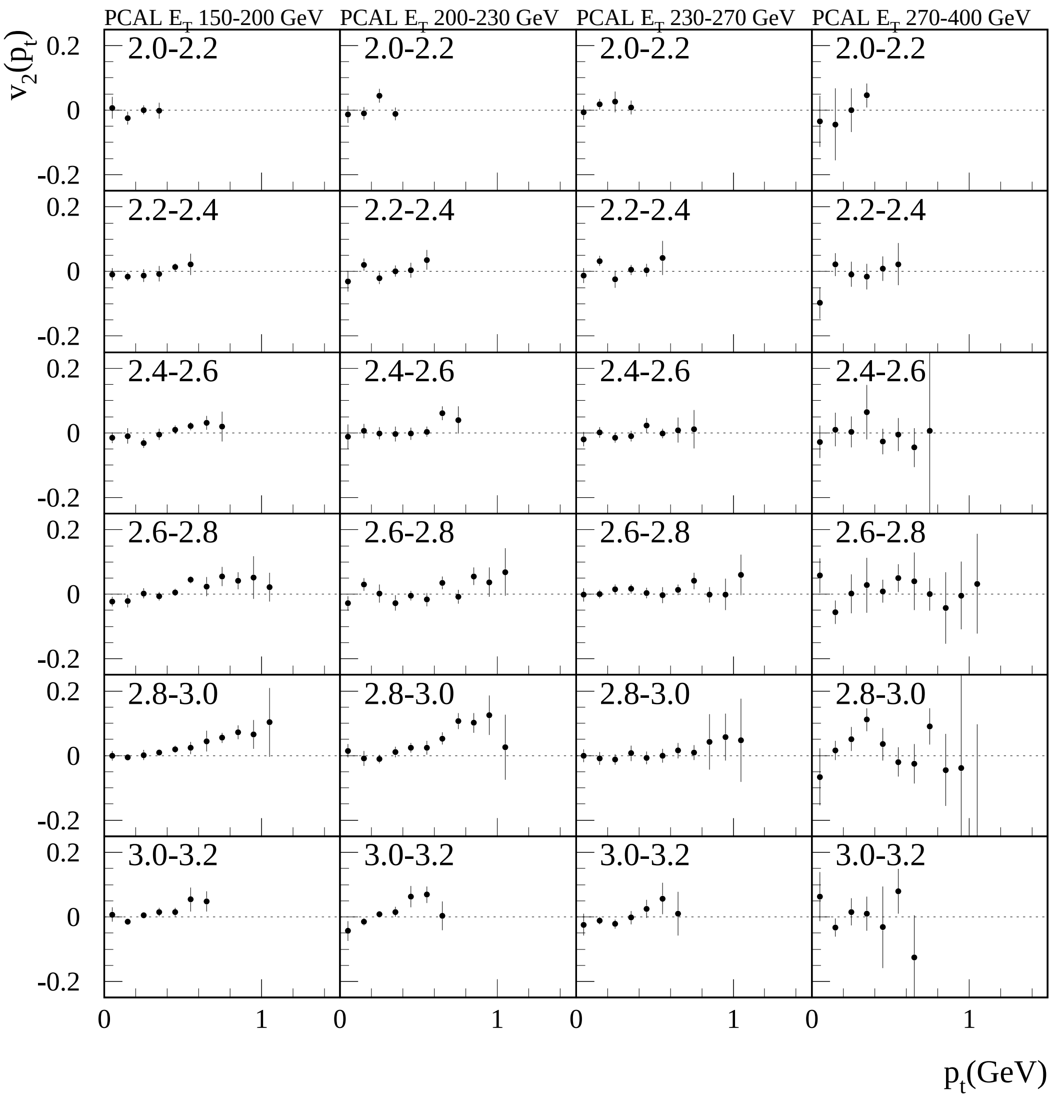

Figure 7.13: The $v_2(p_t)$ of protons for various rapidity bins starting with $1.6 < y < 2.0$ and for four centrality bins as labeled on top.

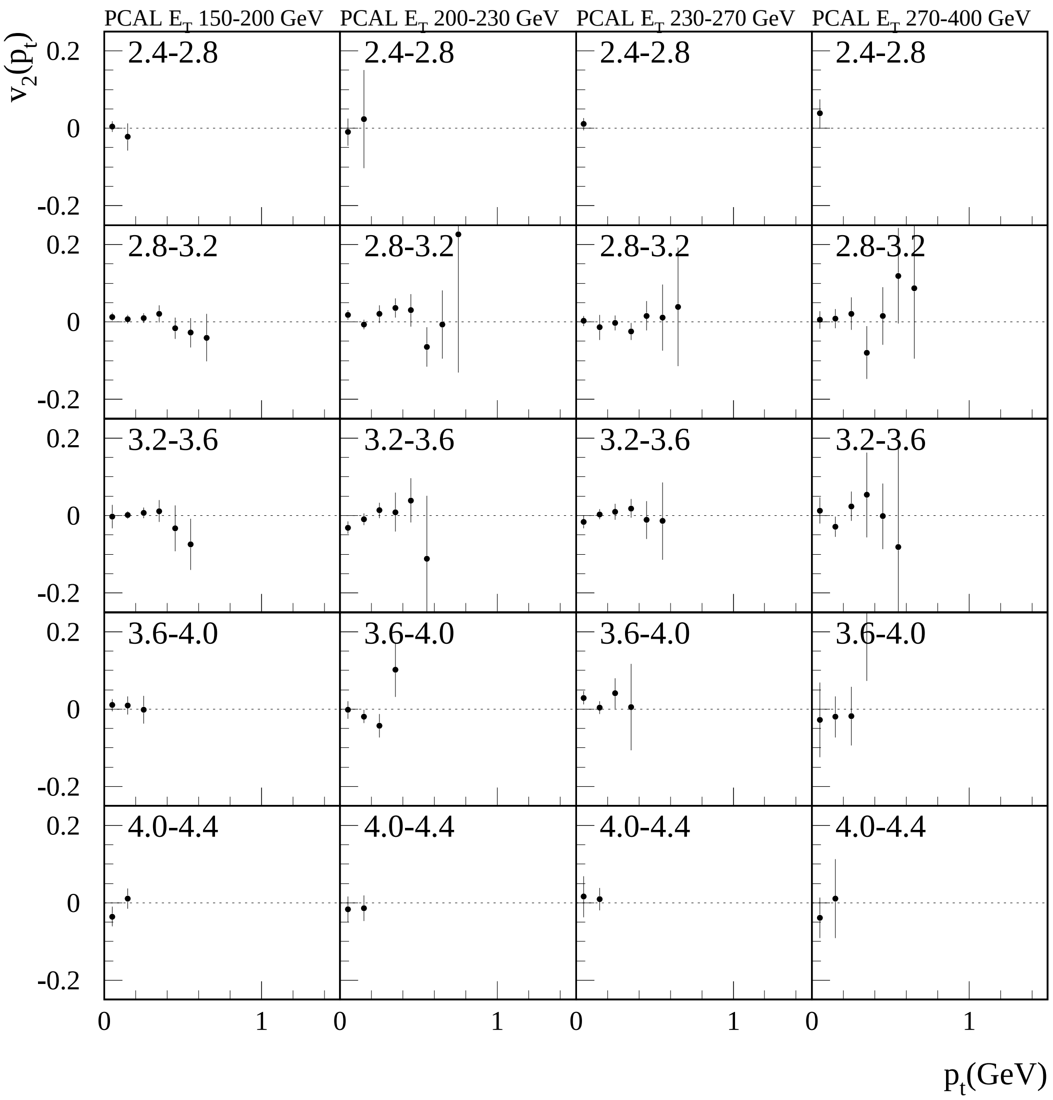

Figure 7.14: The $v_2(p_t)$ of positive pions for various rapidity bins starting with $2.4 < y < 2.8$ and for four centrality bins.

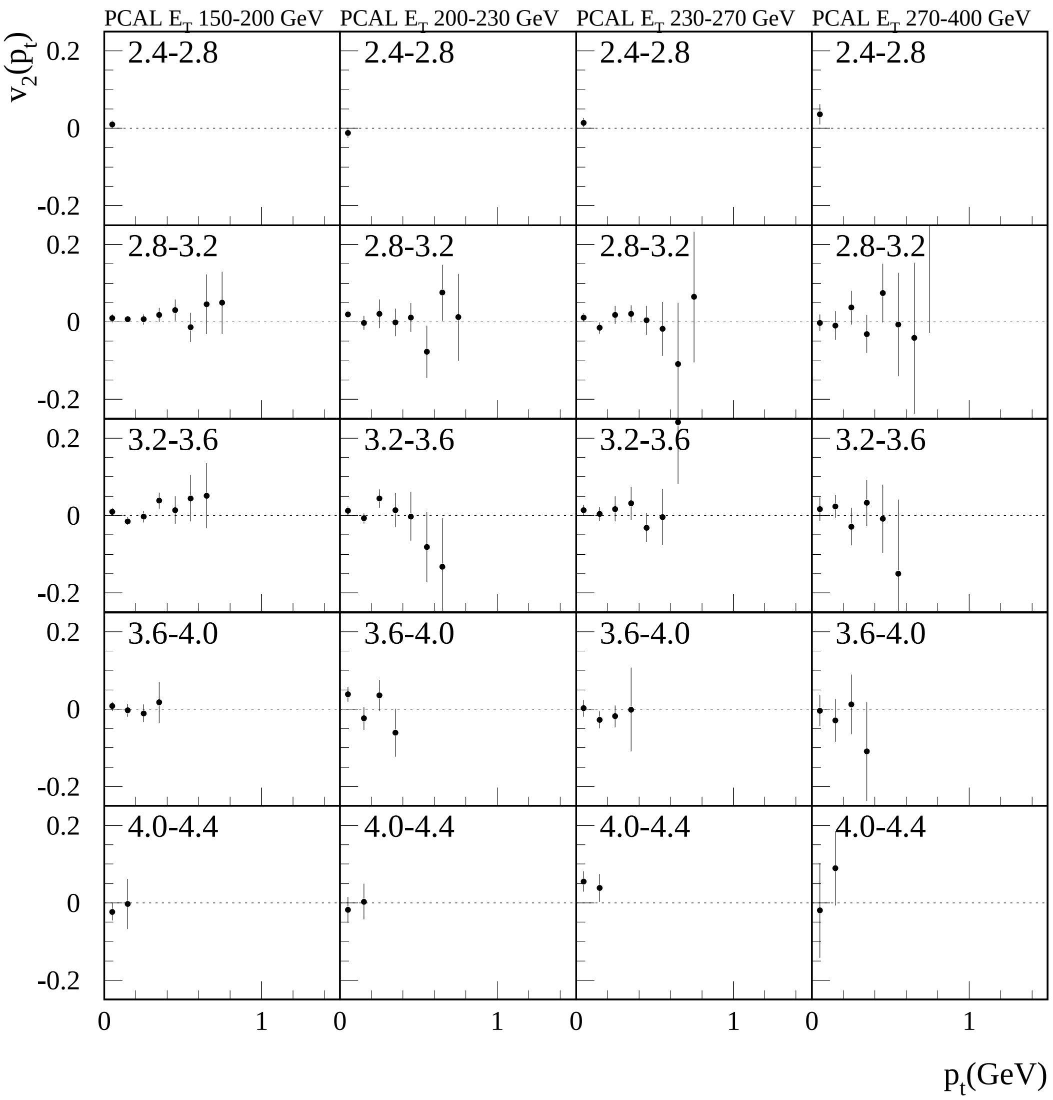

Figure 7.15: The $v_2(p_t)$ of negative pions for various rapidity bins starting with $2.4 < y < 2.8$ and for four centrality bins.

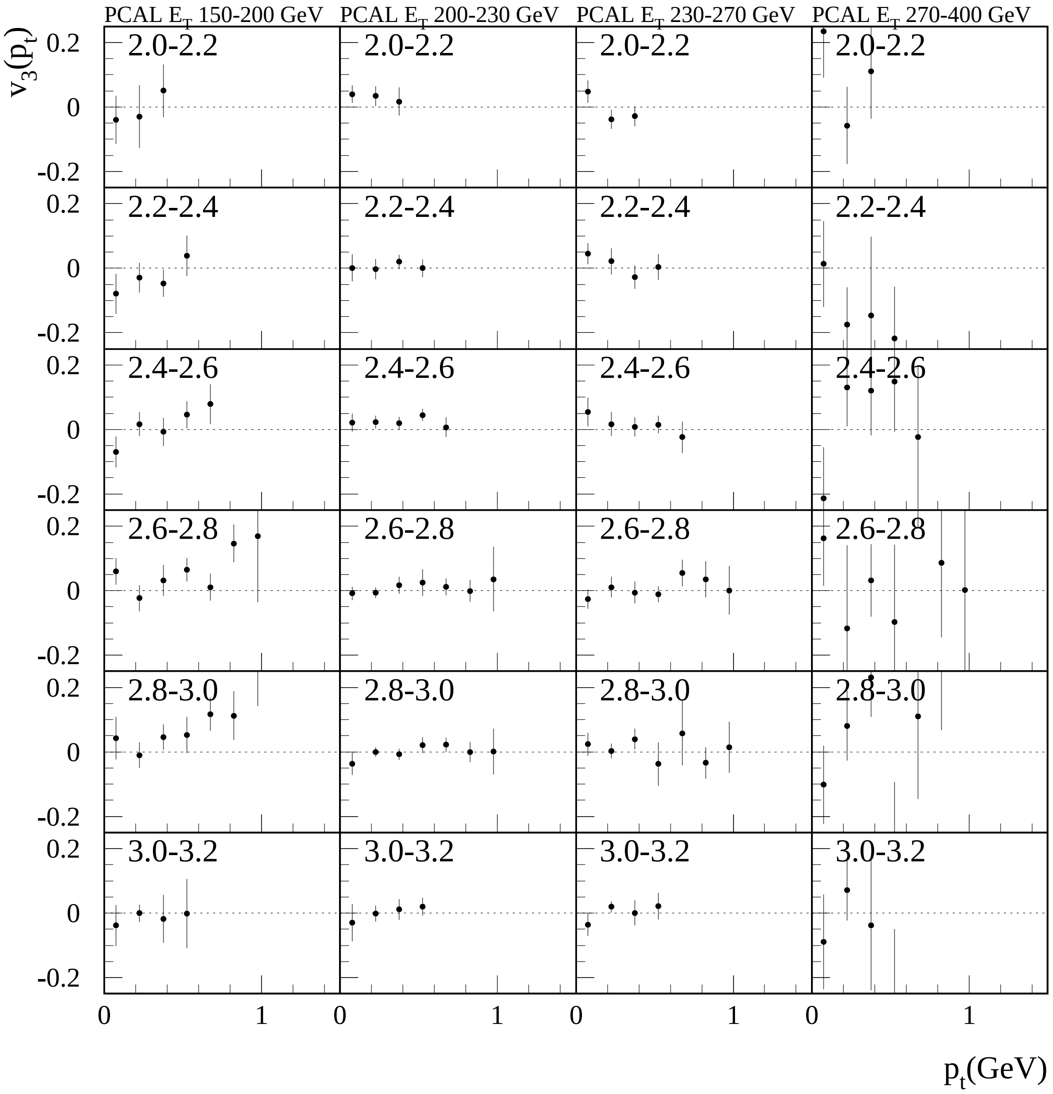

Figure 7.16: The $v_3(p_t)$ of protons for various rapidity bins starting with $1.6 < y < 2.0$ and for four centrality bins.

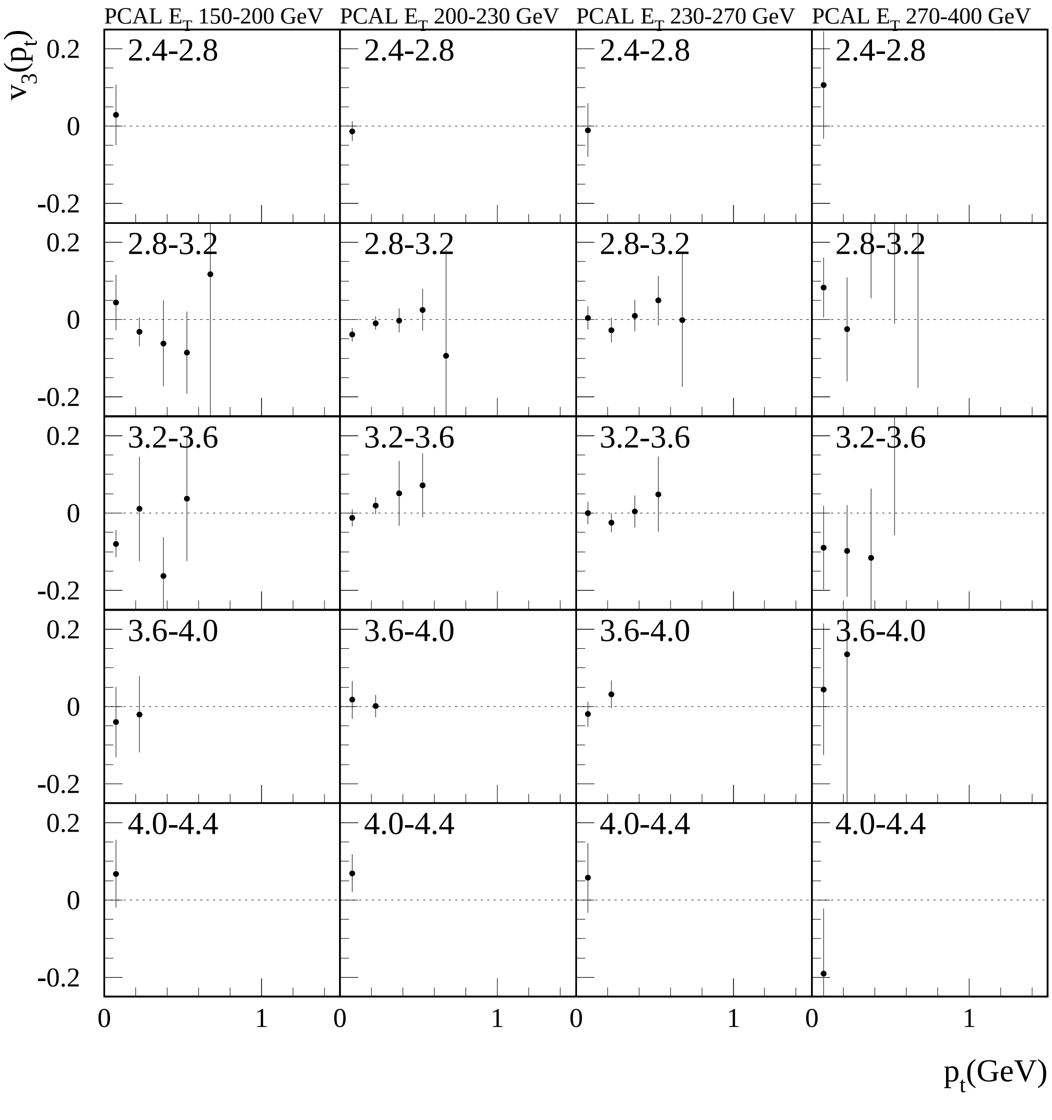

Figure 7.17: The $v_3(p_t)$ of positive pions for various rapidity bins starting with $2.4 < y < 2.8$ and for four centrality bins.

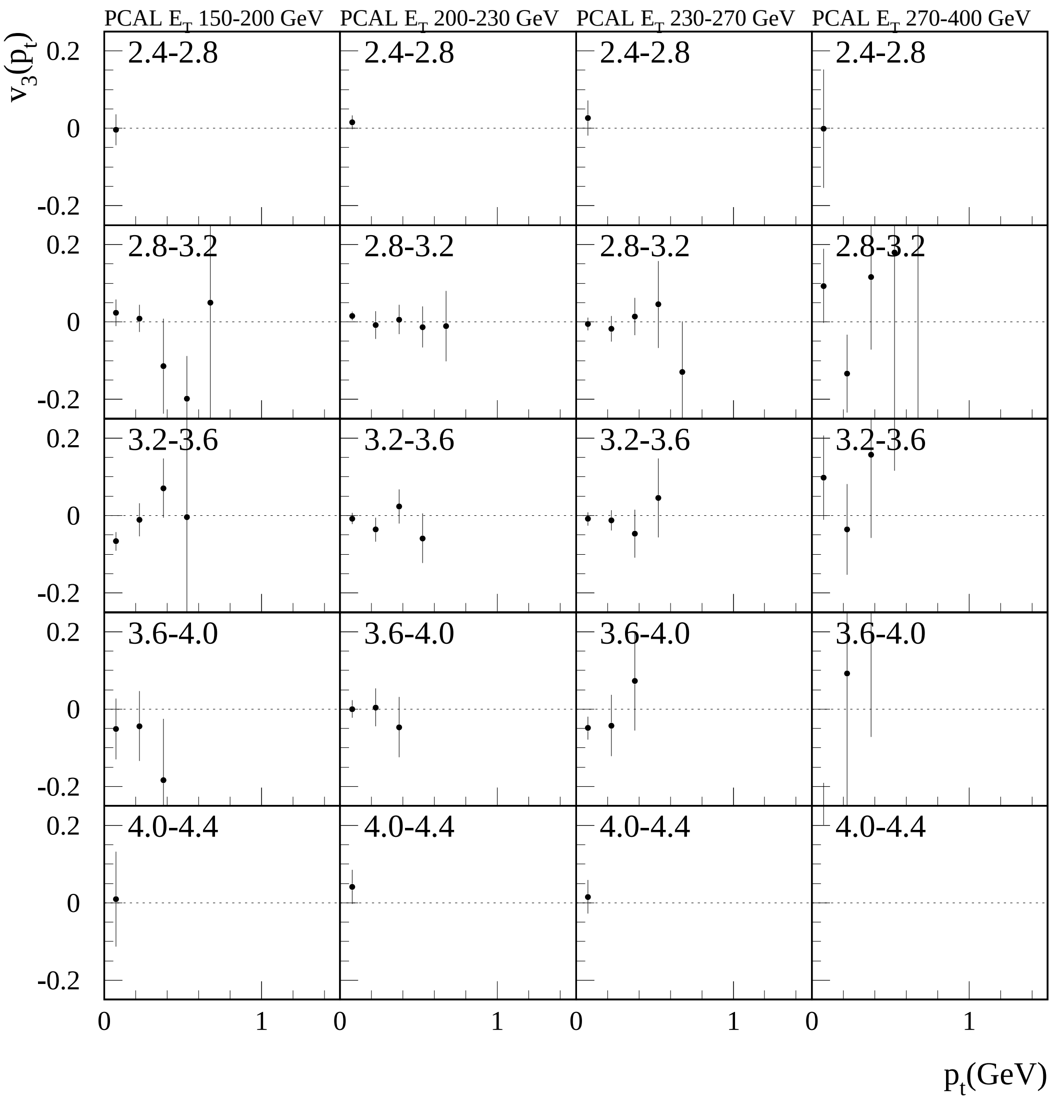

Figure 7.18: The $v_3(p_t)$ of negative pions for various rapidity bins starting with $2.4 < y < 2.8$ and for four centrality bins.

We assume that the source is transversely boosted by built-up pressure along the p_x axis with velocity β_x (which we would call anisotropic transverse velocity, to distinguish from the velocity β_t of isotropic transverse expansion). In order to get the value of E^* one can use the Lorentz transformations:

$$
\begin{aligned}
E^* &= \gamma_x(E - \beta_x p_x) && (7.13)\\
&= \gamma_x(E - p_t\beta_x\cos(\phi')) && (7.14)
\end{aligned}
$$

where $\gamma_x = 1/\sqrt{1-\beta_x^2}$ and the energy $E = m_t\cosh(y - y^*)$ is evaluated in a system moving longitudinally with the same velocity y^*.

If we assume $\beta_x \ll 1$, the invariant particle distribution becomes:

$$
\begin{aligned}
\frac{1}{m_t}\frac{dN}{dm_t dy d\phi'} &\propto E\exp(\frac{-E}{T})(1 - \frac{p_t\beta_x}{E}\cos(\phi') + \frac{p_t\beta_x}{T}\cos(\phi')) && (7.15)\\
&\propto (1 + 2v_1\cos(\phi')). && (7.16)
\end{aligned}
$$

It follows that

$$
v_1 \approx \frac{\beta_x}{2T}\left(1 - \frac{T}{E}\right)p_t. \quad (7.17)
$$

For protons with $E \gg T$, this picture leads to a linear dependence of v_1 on p_t with the slope of $\beta_x/2T$. If we take into account the effect of transverse (isotropic) expansion, the formula becomes more complicated [35], but the magnitude of directed flow (v_1) in the high p_t region is still proportional to β_x except that the slope depends now on the inverse slope parameter T_B, instead of the real temperature of the source T:

$$
v_1 \approx \frac{\beta_x}{2T_B}p_t. \quad (7.18)
$$

Fitting $v_1(p_t)$ for protons from Fig. 7.2 with T_B of the azimuthally integrated spectra, we extract the transverse boost velocity β_x of the proton source for different proton rapidities and collision centralities in Fig. 7.19. It is observed that the extracted source velocity β_x of protons increases towards beam rapidity and is largest in the mid-central bins. The average value of β_x is about 0.08 which is relatively small compared to radius-averaged transverse expansion velocity $\langle\beta_t\rangle \sim 0.3 - 0.4$ [14].

If we assume a thermal transverse spectra for dN/dp_t and Eq. 7.18 as an approximation for $v_1(p_t)$, there exists the following relationship between $\langle p_x\rangle$ and β_x:

$$
\begin{aligned}
\langle p_x \rangle &= \frac{\int \frac{dN}{dp_t}(v_1(p_t)\cdot p_t)dp_t}{\int \frac{dN}{dp_t}dp_t} && (7.19)\\
&\approx \frac{1}{N_0}\int [(p_t\, m_t\, \exp(-\frac{m_t}{T_B}))(\frac{\beta_x}{2T_B}p_t^2)]dp_t && (7.20)
\end{aligned}
$$

As we see in Fig. 7.20, the $\langle p_x \rangle$ decreases after $y = 3.0$ in the framework of a boosted thermal source, this is not due to the source velocity β_x which still keeps increasing but because of the decreasing of T_B.

For pions shown in Fig. 7.3–7.4, we observe that v_1 has almost no dependence on p_t. This means that the physics of the development of flow for pions is different from that of protons. One possible explanation of pions, a purely produced particle, would be the absorption by the nuclear spectators. Pion are produced isotropically in the center of mass system of the collision and those which move in the direction of nucleon flow will be absorbed by spectators moving in the same direction. The assumption of the independence of the absorption cross section on pion p_t would explain the observed v_1 behavior qualitatively. In more central collisions pions are absorbed less by the spectator nucleons and experience more re-scattering with participant nucleons. This picture supports more positive values of v_1, of the same sign as the nucleon flow, toward central collisions, as is seen in the data.

7.4.2 The Results of Disentangled Nucleon and Pion Flow

In terms of a parameterization of the experimentally measured phase space, the corresponding relationships between pseudo-rapidity (η) and rapidity (y) and the $\langle p_t \rangle(y)$ for both protons and pions are obtained (see Appendix C). Based on these, we map the nucleon and pion flow, which were extracted from the measured charged multiplicity flow ($v_1^{N_{ch}}(\eta)$) and transverse energy flow ($v_1^{E_t}(\eta)$) in Chapter 6, into rapidity space y and, assuming the flow signal weighted by the transverse energy E_t of the particle to be the same as that weighted by the transverse momentum p_t, we calculate $\langle p_x \rangle$ of nucleons and pions around mid-rapidity by,

$$
\langle p_x \rangle(y) = v_1(y)\cdot\langle p_t \rangle(y). \qquad (7.21)
$$

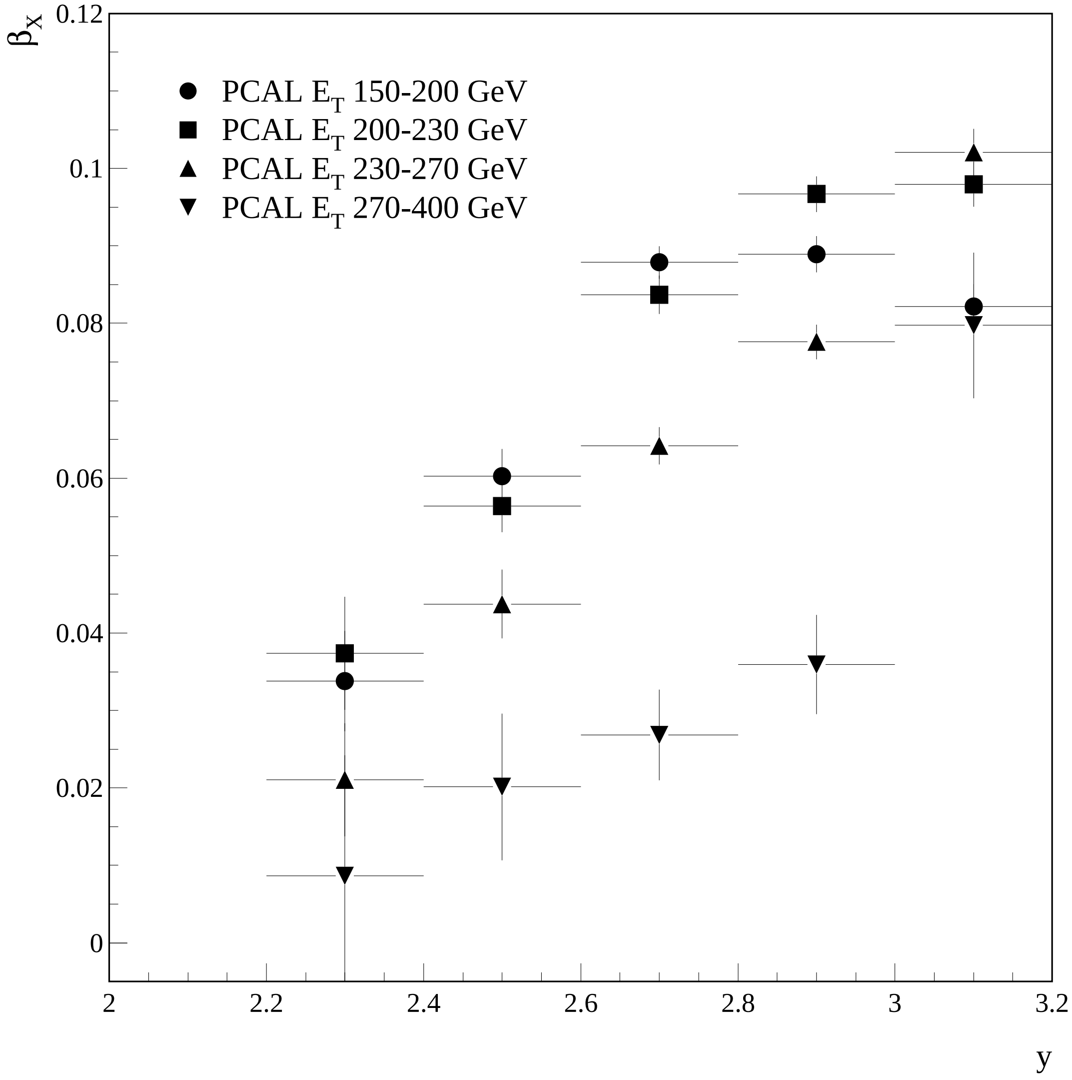

Figure 7.19: Transverse boost velocity β_x of the thermal source for different proton rapidities and centralities of the collision.

The results are shown in Fig 7.20. The horizontal error bars represent the widths of the rapidity region(Δy) contributing to the pseudo-rapidity range used to get corresponding v_1 for rapidity bins. Overall there is a good agreement between the results of the analysis in the spectrometer (at forward rapidities) and those derived from the flow of global variables (around mid-rapidity). However, it should be noted that the uncertainties in the rapidity region where these two measurements can be compared are rather large. Combining them together provides a complete measurement of $\langle p_x \rangle$ of protons(nucleons) as a function of rapidity with a **S**-shape curve similar to that observed at lower energies [16]. The prediction of a vanishing $\langle p_x \rangle(y)$ in the region of the width of about one unit rapidity around mid-rapidity as a result of a QGP phase [59] is not observed in our measurements.

7.4.3 Comparison with Cascade Models

In Fig. 7.20, overlayed with our measurements of $\langle p_x \rangle(y)$ at centrality of top 9-13%, are the predictions from the models RQMD and ARC. The centrality of the events from RQMD model is defined as closely as possible to what is performed in the data by making cuts in the transverse energy in a certain pseudo-rapidity region predicted by RQMD instead of in the impact parameters. However, ARC's results quote a cut on the top 10% centrality [38]; it is not clear whether an inclusive or exclusive cut was performed.

The RQMD model running in cascade mode(version 2.3) under-predicts the proton flow. The inclusion of the mean field potential(version 2.3), a potential as a function of baryon density acting on the nucleons only, enhances the proton directed flow; its predictions agree with the data at forward rapidities ($2.8 < y < 3.2$) and appears to underestimate it in the region closer to mid-rapidity. Turning on the mean field attenuates the "anti-flow" of pions and makes the magnitude becomes almost zero. As for the elliptical shape, RQMD with or without the mean field potential correctly predicts a "in-plane expansion" instead of "out-of-plane squeeze out"(see Fig. 6.4).

The ARC model [38] has been shown to describe flow data in the p = 1-2 GeV/c beam momentum range without the use of a mean field by preserving the scattering plane in each collision and allowing only repulsive scattering. At energies significantly above the pion production threshold, such a scheme would be inappropriate. At AGS, the beam energy is well above the pion production threshold and the author argue [38] that the initial collisions are mostly diffractive processes. Therefore the authors have extended the ARC mechanism to AGS energies by incorporating a 50/50 mixture of repulsive and attractive trajectories for collisions with $E_{CM} > 3m_\pi$, purely repulsive

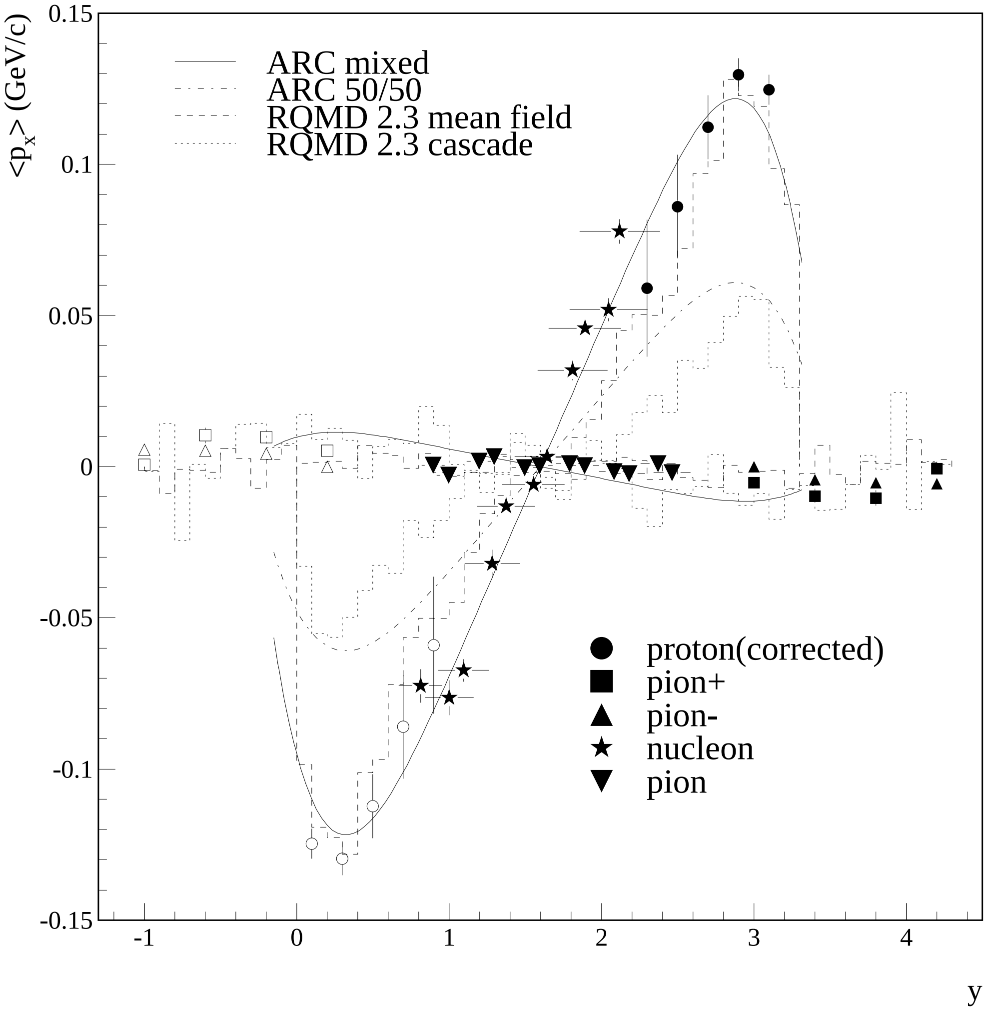

Figure 7.20: The fitted $\langle p_x \rangle(y)$ of protons including the reaction plane resolution correction. The model predictions from ARC and RQMD are shown as lines. The points around mid-rapidity ($y = 1.6$) are the derived nucleon and pion flow from charged multiplicities N_{ch} and transverse energy E_T (see text).

trajectories for $E_{CM} < 2m_\pi$, and a smooth interpolation between the two. These calculations with either 50/50 mixture at all energies or the energy dependent mixture of repulsive scattering are quoted from Ref. [38] and shown in Fig 7.20. The results of the energy independent mixture under-predicts the proton flow and are close to the results of RQMD in cascade mode. The other results with an energy dependent mixture agree with the data of proton directed flow. In Ref [38], the prediction of the second moment (the elliptic event shape) that "protons are ejected symmetrically out of the reaction plane near mid-rapidity" and "the pion distributions are symmetric around the beam axis" in the central 10% cut is qualitatively different from the positive values of v_2 observed in the flow signals of global variables.

As mentioned before, the flow signals $v_n(p_t)$ contain more informations than $\langle p_x \rangle$ and impose more stringent comparisons with theoretical models; the measurements of the first three Fourier moments at one rapidity and centrality bin for protons and charged pions are compared with the results from both modes in RQMD and are shown in Fig. 7.21. We find that, even though RQMD in the mean field mode reasonably produces the values of $\langle p_x \rangle$ of protons at $2.8 < y < 3.0$, the prediction of $v_1(p_t)$ does not agree with the data at all. As demonstrated in Eq. 7.9, the $\langle p_x \rangle$ is the integral of dN/dp_t weighted by $v_1(p_t)$ over the transverse momentum p_t. This implies that RQMD must have an incorrect prediction of the shape of the transverse spectra dN/dp_t. This was checked to be true. In Table 7.2, we list the inverse slope parameters (T_B) at different rapidities for the top 13-9% central events. The mean field potential brings in more repulsion so that it enhances the distributions at higher p_t and the slope parameter, but both modes of RQMD still significantly underestimate the measured values of T_B. The comparison for charged pions and higher moments (v_2, v_3) shows reasonable agreement within the errors of our data.

Therefore, pure cascade models, without an ad hoc treatment of the mean field potential in RQMD or the varying properties of trajectories in ARC, either under-predicts or overshoots the existing data. While they are closely related, the connection of these two approaches is still not clearly understood: one treats a baryon-density-dependent potential and the other has a energy dependent treatment of two body collision in the free space. Further detailed and systematic comparisons in $v_n(p_t)$ and flow shape of higher moments should in principle impose more stringent tests on the models and bring about a deeper understanding.

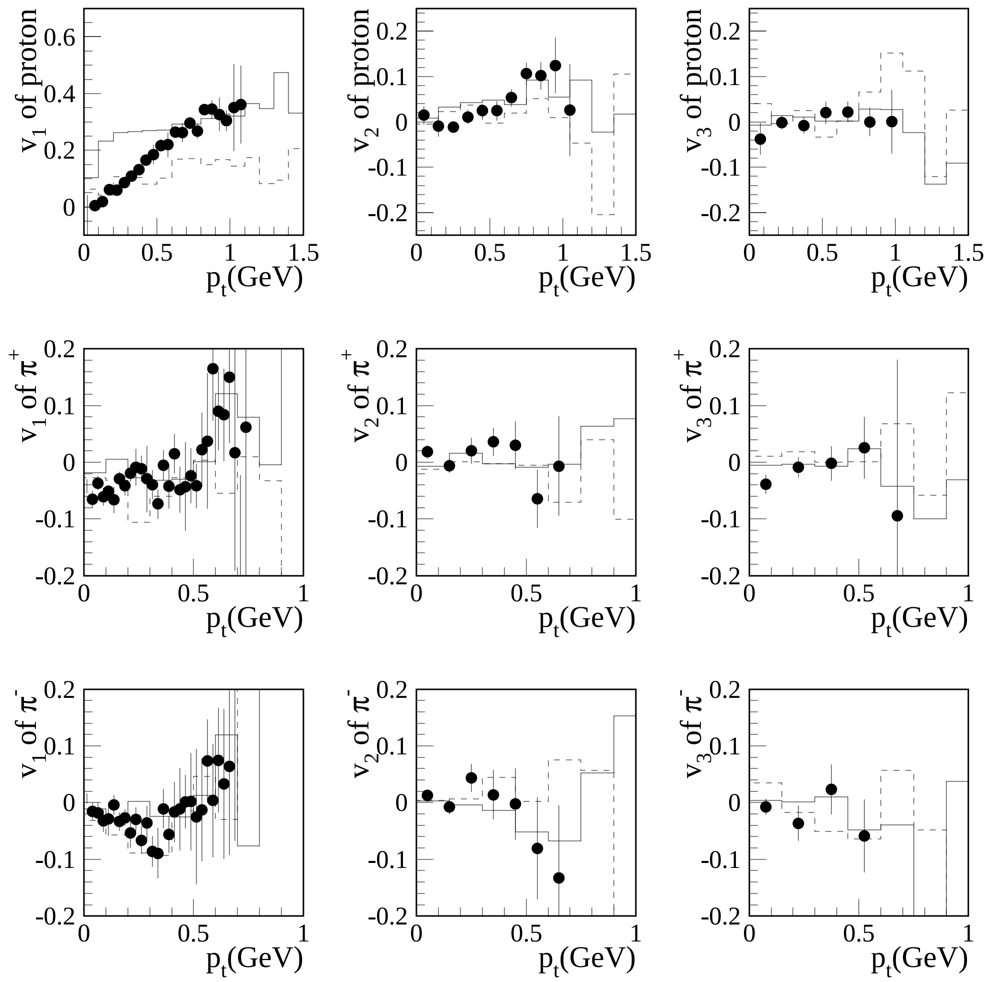

Figure 7.21: The comparison of v_1, v_2, v_3 expressed as a function of p_t for protons and charged pions with the predictions from both modes of RQMD(version 2.3), cascade mode(dashed lines) and mean field mode(solid lines). The centrality bin is the top 13-9% central events. The observed rapidity bin for proton(π^+, π^-) is $2.8 < y < 3.0$($2.8 < y < 3.2$, $3.2 < y < 3.6$).

proton				π^-			
rapidity	E877	RQMD^1	RQMD^2	rapidity	E877	RQMD^1	RQMD^2
2.0-2.2	0.280	0.157	0.189	1.6-2.0		0.134	0.128
2.2-2.4	0.240	0.150	0.172	2.0-2.4		0.123	0.126
2.4-2.6	0.180	0.137	0.150	2.4-2.8		0.118	0.116
2.6-2.8	0.150	0.122	0.133	2.8-3.2	0.085	0.099	0.097
2.8-3.0	0.130	0.107	0.110	3.2-3.6	0.072	0.085	0.084
3.0-3.2	0.100	0.100	0.093	3.6-4.0	0.075	0.061	0.062

Table 7.2: The inverse slope parameters T_B of protons and negative pions from the E877 measurements and RQMD. The units are in terms of GeV. The fitting errors of T_B are not shown and on the typical order of 0.01 GeV. The superscript 1(2) of RQMD represents the cascade(mean field) mode.

Chapter 8

Excitation Function of Azimuthally Anisotropic Flow

Preliminary data on the measured directed flow from E895 which runs at beam momenta at 2 and 4 GeV at the AGS is available [60]. Combining the BEVALAC data and our measurement, it would be informative to see how the excitation function of azimuthally anisotropic flow evolves through this region where the conditions for forming a QGP might be fulfilled. Especially interesting, the qualitative change of the elliptical flow from BEVALAC to AGS will reveal valuable information about the early pressure and the interplay of the expanding of participants and the spectators with an increase in beam energy [39]. We used the model RQMD (version 2.3 mean field mode [39]) as a benchmark to understand how the purely hadronic physics develops with increasing beam energy.

8.1 Directed Flow

There are various flow definitions in the excitation function and we list them in the following:

- <u>Radial Flow:</u>
  - **The radius-averaged radial flow velocity $\langle\beta_t\rangle$ at mid-rapidity(model dependent):** [14, 19]

$$\langle\beta_t\rangle \equiv \left(\int_0^R \beta_t(r) r dr\right)/(0.5R^2) \tag{8.1}$$

  - **The average radial flow velocity $\langle\beta_r\rangle$:** [40]

$$\langle\beta_r\rangle \equiv \frac{1}{N}\sum_i^N \frac{\vec{p_i}}{E_i}\cdot\frac{\vec{r_i}}{r_i} \tag{8.2}$$

- **The average transverse velocity $\langle p_t/m \rangle$ at mid-rapidity:** [39]

- Directed Flow:

  - **The slope of $\langle p_x \rangle$ at mid-rapidity:** [38]

$$F(flow) \equiv \frac{d\langle p_x/A \rangle}{dy}|_{y=y_{cm}} \tag{8.3}$$

  - **The slope of $\langle p_x \rangle$ at mid-rapidity normalized by projectile rapidity:** [47]

$$F(flow) \equiv \frac{d\langle p_x/A \rangle}{d(y/y_p)}|_{y=y_{cm}} \tag{8.4}$$

  - **The slope of $\langle p_x \rangle$ at mid-rapidity normalized by projectile rapidity in the center of mass frame:** [46]

$$F(flow) \equiv \frac{d\langle p_x/A \rangle}{d(y/(y_p - y_{cm}))}|_{y=y_{cm}} \tag{8.5}$$

  - **The maximum magnitude of $\langle p_x \rangle$:** [38]

$$F(flow) \equiv \langle p_x \rangle_{max} \tag{8.6}$$

  - **The rapidity-averaged $\langle p_x \rangle$ per baryon in the center of mass frame:** [44]

$$F(flow) \equiv \frac{1}{N} \int_{-y_{cm}}^{y_{cm}} \mathrm{d}y \ \langle p_x/N \rangle(y) \ \frac{\mathrm{d}N}{\mathrm{d}y} \ \mathrm{sign}(y) \tag{8.7}$$

Here we use the slope of $\langle p_x \rangle/A$ in terms of the rapidity normalized to the beam rapidity in the CM system (i.e. a normalized y-scale with target and projectile sitting at $+1.0$ and -1.0), Eq 8.5, as a definition of flow. In this definition, the normalization to the beam rapidity in principle compensates for the decrease of the slope stemming from the kinematic effect of increasing rapidity range with the increase of beam energy. There is the basic assumption of the flow curve to be a straight line around mid-rapidity in this definition. This is found to be reasonable in the experiments.

In evaluating the slope of our measurement at AGS, we take the average of the values of slopes by including different points in the fit as shown in Fig. 8.1. The excitation function of this flow parameter of the Au + Au system is shown in Fig. 8.2. As for the centrality, all data are taken from where the flow signals are largest corresponding to mid-central collisions and in RQMD the events of $b = 6$ fm are sampled.

It is observed that the magnitude of directed flow rises with increasing beam energy for $E_k < 2$ GeV and then drops above this beam energy. Our measurement at 10 GeV is of about the same magnitude as the preliminary value reported by E895 at 4 GeV [60] within errors. Whether this dropping of flow results from a more diffractive collision [38] or the appearance of a QGP which softens the EOS [44] or some other physics, it is worthwhile to be understood. It will be interesting to have detailed experimental measurements around this region to search for the existence of a "softest point" predicted by hydrodynamical calculations [44, 45]. If found, this would be a generic evidence of QGP.

8.2 Elliptic Flow

Our measurement of a positive second moment of azimuthal asymmetry in the transverse energy flow represents an elliptical shape with the major axis lying along the orientation of the reaction plane. This component is qualitatively different from the observation of "squeeze-out" at low energies [16, 21] where the emission is found to be perpendicular to the reaction plane. There has been a report from NA49 of a nonzero second moment at mid-pseudo-rapidity [37]. However the orientation is not known yet. We compile data and use RQMD as a benchmark to show the excitation function of the elliptic flow in Fig. 8.3. The choice of centrality cut is the same as that in the excitation function of the directed flow.

The values of v_2 at mid-rapidity are of the largest negative magnitude at $E = 0.5$ GeV, where the phenomena of "squeeze-out" is maximum, and then approach positive values with the increasing beam energy. The RQMD predictions show qualitatively the same trend.

We can look into the history of the development of the elliptic flow within the framework of RQMD for Au + Au at AGS energy via the variable $E_{dir} \propto E(\text{Energy}) \cdot v_2$ at mid-rapidity. As demonstrated in Fig. 8.4, in the first 5 fm/c of time in the center of mass system, "squeeze out" effect exists because of the surrounding spectators; then the elliptical flow changes into a expansion into the reaction plane after the spectators move away. The overall time-integrated value of E_{dir} turns out to be positive because of the relatively short period and the small strength of the "squeeze out" effect at this specific beam energy.

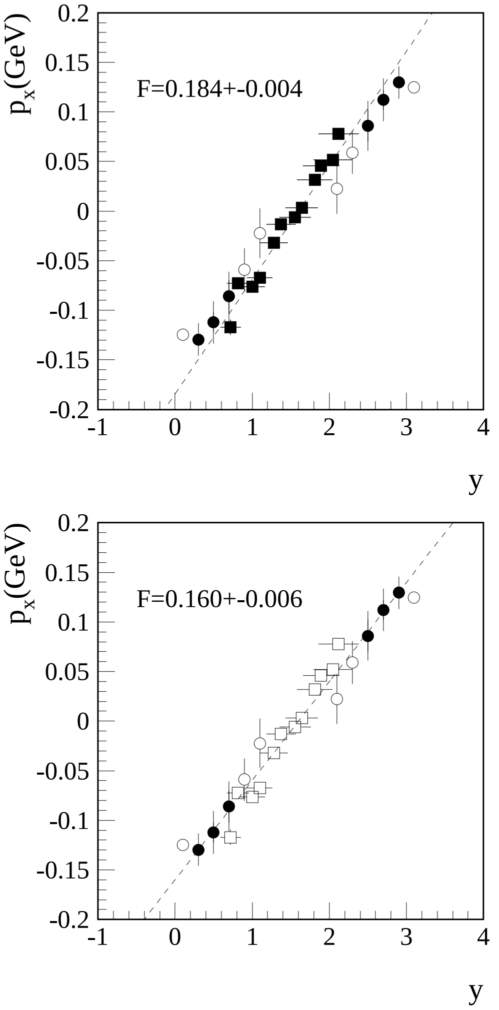

Figure 8.1: The flow variable F as a function of points in the fit. Only the solid points are used in the fit. The flow F is defined in the text. The circles represent the flow of identified protons and the squares are the disentangled and mapped nucleon flow.

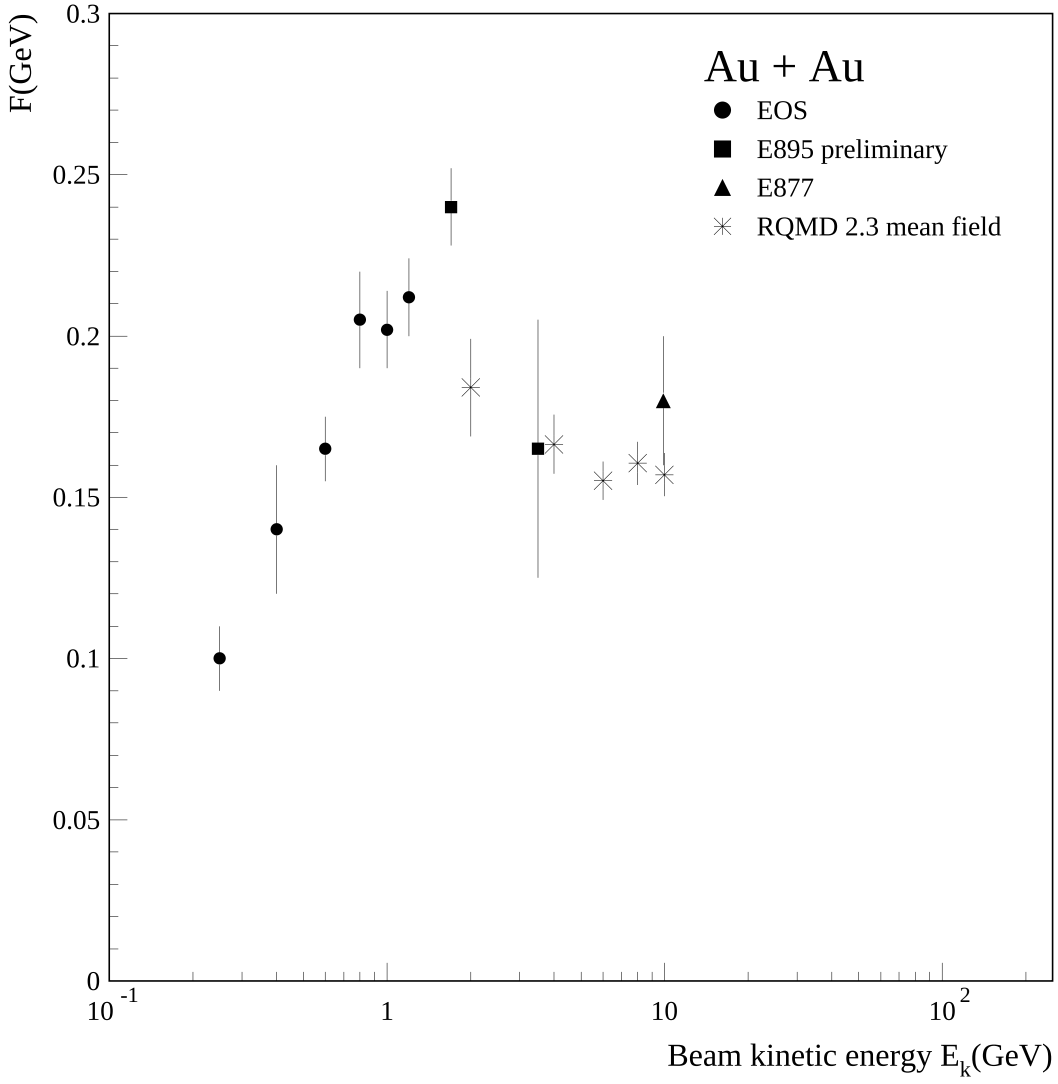

Figure 8.2: The excitation function of directed flow F(defined in the text) as a function of beam kinetic energy per nucleon(E_k). E_k is the beam energy minus the rest mass of nucleon. The data of EOS(E895) group is taken from Ref. [19]([60]).

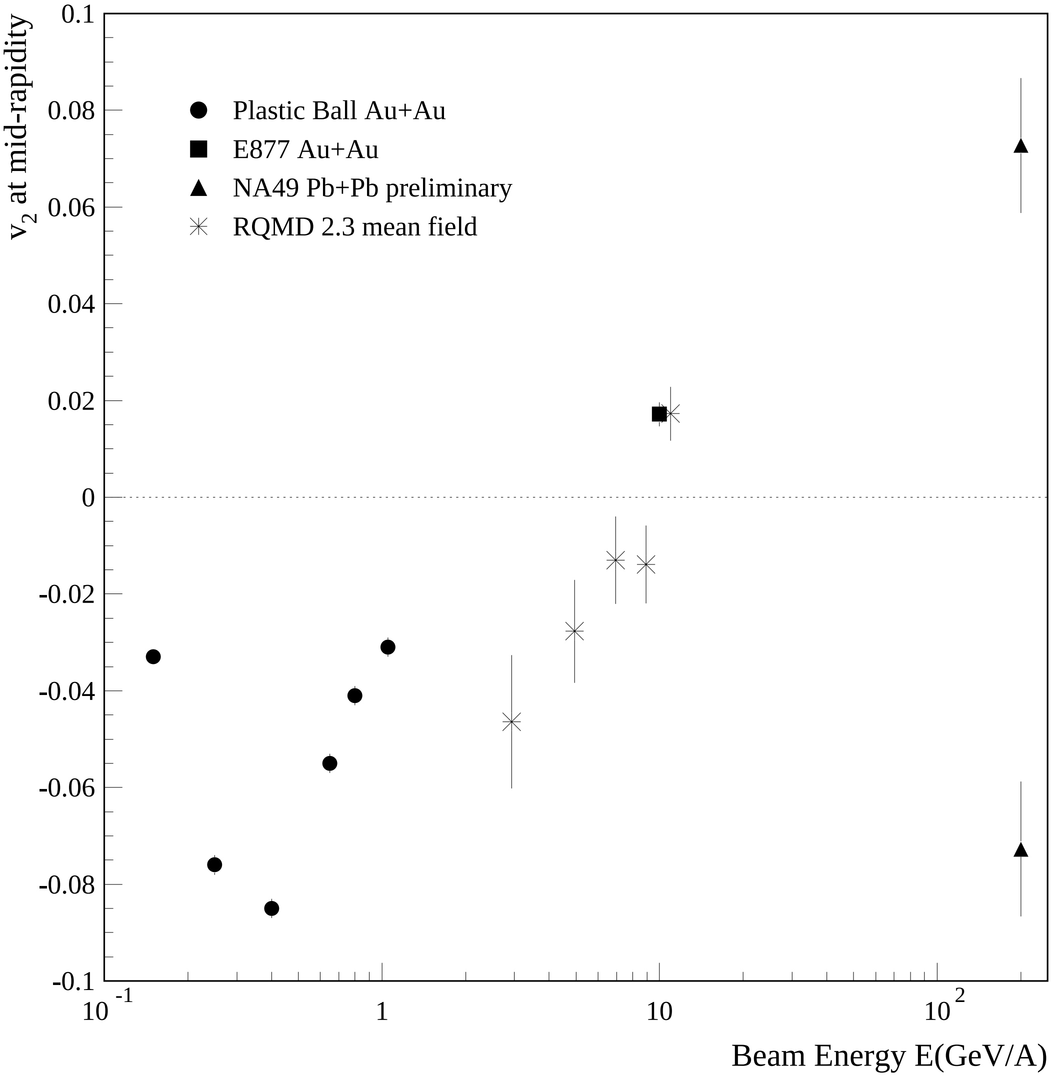

Figure 8.3: The excitation function of the second Fourier moment v_2 for protons, which characterizes the elliptic flow, at mid-rapidity as a function of beam energy per nucleon(E). The data of the Plastic Ball(NA49) group is taken from Ref. [16]([37]).

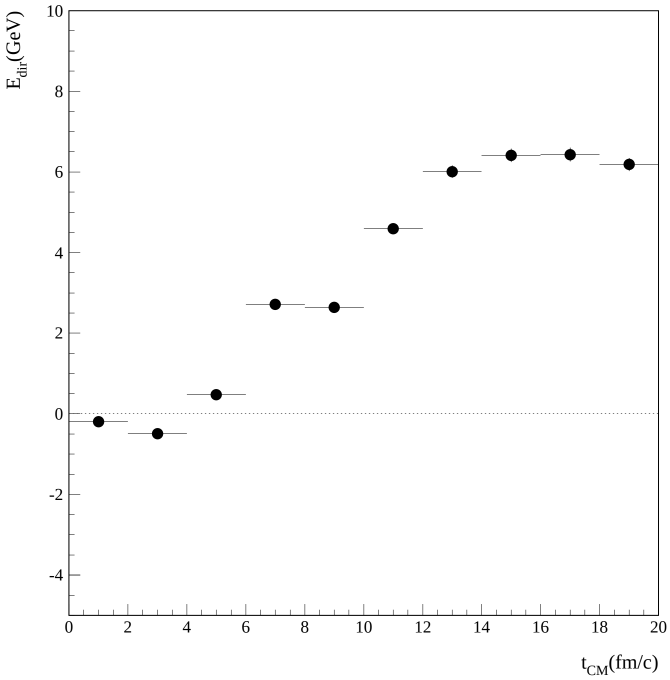

Figure 8.4: The evolution of elliptical flow in energy in RQMD as a function of time in the center of mass system for Au + Au at 11 GeV/c. E_dir is defined in the text. The centrality cut in the model is $5 < b < 7$ fm in impact parameter(b).

It is interesting to study the physics that causes the change of sign of the elliptical flow as a function of beam energy. Whether it is due to a relatively slower building up of pressure in term of passing-by of spectators, or less pressure from a QGP to diminish the absorption effect, is yet to be seen. The experimental efforts to locate the point of the disappearance of elliptical flow will be of importance.

Chapter 9

Conclusions and Final Remarks

In this thesis, the azimuthal distributions of transverse energy with respect to the reconstructed reaction plane is studied systematically as a function of pseudo-rapidity and centrality for 10.8 A GeV/c Au + Au collisions. The anisotropy is quantified by the Fourier moments of the azimuthal distribution and corrected for the finite reaction plane resolution. More detailed distribution of flow signals are revealed compared to previous works [31].

A pronounced component of the directed flow, i.e. the first moment, is observed. It crosses zero at mid-pseudorapidity and has opposite signs at forward and backward pseudorapidity. This is an approximate **S**-shape curve of a back-to-back correlation which is characteristic of directed flow. In addition a small and positive second moment, an elliptic component, is observed. The major axis is oriented in the reaction plane and there is no significant rapidity dependence. This component is of a different orientation from the phenomena of "squeeze-out" observed at lower energies. The centrality dependence of the azimuthally anisotropic flow consistently peaks at intermediate centralities and vanishes for very central and peripheral collisions.

The difference between the measurements of directed flow in E_T and N_{ch} is used to disentangle nucleon and pion flow around the mid-η region at one intermediate centrality bin. It is found that nucleons exhibit a relatively large directed flow, whereas the flow strength of pions is much less and in the opposite direction to that of the nucleons.

The flow signals of identified protons and charged pions are consistent with the observation in the measurement of global variables whose acceptance is complementary to that of the forward spectrometer. The triple differential distribution of particles with respect to the reaction plane are reconstructed. Three signals $v_n(p_t, y)$, $T_B(\phi, y)$, and $\langle p_x\rangle(y)$ extracted from it are presented. The linear p_t dependence of v_1 of protons is interpreted in the picture of a transverse boost thermal source; the source velocity β_x reaches about 0.1

around beam rapidity in mid-central collisions. The p_t and centrality dependence of pion flow suggest a interplay of absorption by spectator nucleons and re-scattering by participant nucleons.

RQMD(2.3 cascade) fails to reproduce the amplitude of the directed flow signal $\langle p_x \rangle$ for protons. Taking into account the mean field mechanism agrees better while the predicted pion flow is reduced. However, RQMD fails in the comparison of the values of $v_1(p_t)$ for protons and also the inverse slope parameters ($T_B(y)$) describing the transverse spectra. RQMD correctly predicts the observed positive second moment. On the other hand, with an appropriate choice of repulsive and inelastic trajectories, ARC agrees with the measurement of $\langle p_x \rangle$ but fails in reproducing the "in-plane expansion" of the elliptic flow.

The experimental flow analysis bears a significant influence on the theoretical study of heavy ion collisions. In transport models, too little pressure is produced from the cascade of a quasi-free hadron and resonance gas to describe the data. This makes necessary the inclusion of some mechanism to raise the pressure. For example, ARC [38] utilizes the repulsive orbits, RQMD [39], the quasi-potential and ART [40], the mean field potential. Theoretical works also show that the directed flow (or azimuthal asymmetry) is sensitive to the possible modification of effective mass and the interaction cross section in the dense nuclear medium [41]. It is important to check how physics other than flow properties are affected by these theoretical ad hoc mechanisms, e.g. the single particle spectra and radial flow etc, to see whether a consistent picture is given.

Especially interesting, H. Sorge [39] argued that elliptical flow (the second moment of azimuthal distribution) is sensitive to the pressure at the early stage of maximum compression and highest baryon density where the transition to QGP is most likely to happen. It is demonstrated in RQMD(version 2.3, mean field mode) that the development of this type of flow involves both early squeeze-out (of a negative second moment) by spectator absorption and later geometrical expansion (of a positive second moment) of the participant zone in the reaction plane. By studying the elliptical flow, which reflects the difference between the early and late pressures in terms of the moving away of spectators, and the average transverse flow $\langle p_t \rangle$, which reflects the scalar summation of them, the pressure at the early stage of maximum compression and highest baryon density can possibly be singled out, aiding to clarify the expansion scenario.

It is shown in the study of the excitation functions that the directed flow of protons decreases and the elliptic flow at mid-rapidity changes sign from BEVALAC to our measurements at AGS. The evolution of underlying physics with increasing beam energy needs to be understood. Theoretical treatments like the mean field potential, the diffractive trajectory and the inclusion of QGP phase in hydrodynamics should be scrutinized under the comparison with the more informative flow signals like $v_n(p_t)$.

Comparisons with theoretical models helps us learn that not only the simplified flow signal like $\langle p_x \rangle$ but also the detailed signals like $v_n(p_t)$ should be checked in the theoretical models. With the future available experimental data, one important and urgent further step will be to have a picture in order to make connections between experimental measurements such like $\langle p_x \rangle$, $v_n(p_t)$ etc and the fundamental physical quantities like temperature T, pressure P, flow velocity β_x etc. The simple model of a boosted thermal source in the interpretation of proton flow is a small step toward this direction. More theoretical effort on the cascade and especially hydrodynamical models are needed, and then we may learn if anything important is still missing in the experimental measurements. Another interesting and challenging question is how to put the two pieces of collective flow, the isotropic flow and the azimuthally anisotropic flow, into the same framework. The collective motions should originate from the same source. Hopefully with both experimental and theoretical efforts, the question of EOS of the nuclear matter in the ultra-relativistic heavy ion collision can be answered. Combined with the study of other signatures of QGP, we are optimistic to have a deep, complete view of this "big puzzle" in the future.

Bibliography

[1] T. W. Ludlam, E. H. Wegner, eds., Proc. Quark Matter '83, Nucl. Phys. **A418** (1984).

[2] L. S. Schröder, M. Gyulassy, eds., Proc. Quark Matter '86, Nucl. Phys. **A461** (1987).

[3] H. Satz, R. Stock, H. J. Specht, eds., Proc. Quark Matter '87, Z. Phys. **C38** (1988).

[4] G. Baym, P. Braun-Munzinger, S. Nagamiya, eds., Proc. Quark Matter '88, Nucl. Phys. **A498** (1989).

[5] J. P. Blaizot, *et. al.*, eds., Proc. Quark Matter '90, Nucl. Phys. **A525** (1991).

[6] T. C. Awes, *et. al.*, eds., Proc. Quark Matter '91, Nucl. Phys. **A544** (1992).

[7] E. Stenlund, *et. al.*, eds., Proc. Quark Matter '93, Nucl. Phys. **A566** (1994).

[8] A. M. Poskanzer, J .W. Harris, L. S. Schroeder, eds., Proc. Quark Matter '95, Nucl. Phys. **A590** (1995).

[9] P. Braun-Munzinger, H. J. Specht, R. Stock, H. Stöcker, eds., Proc. Quark Matter '96, Nucl. Phys. **A610** (1996).

[10] C. A. Pruneau *et al.* eds., Proc. Heavy Ion Physics at AGS '96, Weyne State University.

[11] K. Kajantie and L. McLerran, Ann. Rev. Nucl. Part. Sci. **37**, 293 (1987).

[12] B. Müller, Rep. Prog. Phys. **58** 611 (1995).

[13] J. Stachel and G .Young, Ann. Rev. Nucl. Part. Sci. **42**, 537 (1992).

[14] P. Braun-Munzinger, J. Stachel, J. P. Wessels, and N. Xu, Phys. Lett. **B344**, 43 (1995), and Phys. Lett. **B365**, 1 (1996).

[15] W. Scheid, H. Müller, and W. Greiner, Phys. Rev. Lett. **32**, 741 (1974).

[16] H. A. Gustaffson *et. al.*, Phys. Rev. Lett. **52**, 1590 (1984),
H. H. Gutbrod *et. al.*, Phys. Lett. **B216**, 267 (1989),
H. H. Gutbrod *et. al.*, Phys. Rev. **C42**, 640 (1990).

[17] P. J. Siemens and J. O. Rasmussen, Phys. Rev. Lett. **42**, 880(1979).

[18] G. D. Westfall *et. al.*, Phys. Rev. Lett. **37**, 1202(1976).

[19] H. G. Ritter *et. al.*, the EOS collaboration, Nucl. Phys. **A583**, 491c (1995),
M. D. Partlan *et. al.*, the EOS collaboration, Phys. Rev. Lett. **75**, 2100 (1995),
M. A. Lisa *et. al.*, the EOS collaboration, Phys. Rev. Lett. **75**, 2662 (1995).

[20] S. Wang *et. al.*, the EOS collaboration, Phys. Rev. Lett. **76**, 3911 (1995).

[21] L. B. Venema *et al.*, the Kaos collaboration, Phys. Rev. Lett. **71**, 336 (1993),
D. Brill *et al.*, the Kaos collaboration, Phys. Rev. Lett. **71**, 835 (1993).

[22] Y. Leifels, for the FOPI collaboration, Proc. HIPAGS96,
N. Herrmann, for the FOPI collaboration, Proc. QM96,
V. Ramillien *et al.*, FOPI collaboration, Nucl. Phys. **A587** 802 (1995).

[23] E. Schnedermann, J. Sollfrank, and U. Heinz, Phys. Rev. **C48**, 2462 (1993),
E. Schnedermann, and U. Heinz, Phys. Rev. **C50**, 1675 (1994).

[24] F. Daffin, K. Haglin, and W. Bauer, Phys. Rev. **C54**, 1375 (1996).

[25] J. Kapusta, and D. Strottman, Phys. Lett. **B106**, 33 (1981).

[26] J. Cugnon, J. Knoll, C. Riedel, and Y. Yariv, Phys. Lett. **B109**, 167 (1982).

[27] M. Gyulassy, K. A. Frankel, and H. Stöcker, Phys. Lett. **B110**, 185 (1982).

[28] P. Danielewicz, and M. Gyulassy, Phys. Lett. **B129**, 283 (1983).

[29] P. Danielewicz, and G. Odyniec, Phys. Lett. **B157**, 146 (1985).

[30] J. Ollitrault, Phys. Rev. **D46**, 229 (1992), and **D48**, 1132 (1993).

[31] J. Barrette *et al.*, E877 Collaboration, Phys. Rev. Lett. **73**, 2532 (1994).

[32] W.-C. Chang, for the E877 collaboration, Proc. HIPAGS96,
T. K. Hemmick, for the E877 collaboration, Proc. QM96.

[33] J. Barrette *et al.*, E877 Collaboration, Phys. Rev. **C55**, 1420 (1997).

[34] S. Voloshin and Y. Zhang, Z. Physik **C70**, 665 (1996).

[35] S. Voloshin,"Transverse Radial Expansion and Directed Flow", Phys. Rev. **C** Rapid communication, April 1.

[36] S. Voloshin, E877 Note # HD-96/08/15 and E877 Note # HD-96/08/27.

[37] T. Wienold, for the NA49 collaboration, Proc. QM96.

[38] D. E. Kahana, Proc. HIPAGS96 and references therein.

[39] H. Sorge, Proc. HIPAGS96 and references therein; preprint nucl-th/9610026.

[40] B.-A. Li, and C.-M. Ko, Proc. HIPAGS96 and references therein.

[41] G.-Q. Li and C.-M. Ko, Nucl. Phys. **A594**, 460 (1995).

[42] L. V. Bravina *et al.*, Nucl. Phys. **A566**, 461c (1994), and Phys. Rev. **C50**, 2161 (1994).

[43] E. Shuryak and O. V. Zhirov, Phys. Lett. **89**, 253 (1979).

[44] D. H. Rischke, Proc. QM96.

[45] C. M. Hung and E. V. Shuryak, Phys. Rev. Lett. **75**, 4003 (1995).

[46] G. Rai, for the E895 collaboration, talk given in HIPAGS96.

[47] J Chance *et. al.*, the EOS collaboration, nucl-ex/9607008.

[48] S. A. Bass *et. al.*, Proc. QM96.

[49] L. S. Waters, PhD thesis, SUNY at Stony Brook (1990).

[50] J. Simon-Gillo, PhD thesis, Texas A&M Univ. (1992).

[51] M. S. Muthuswamy, PhD thesis, SUNY at Stony Brook (1992).

[52] Z. Zhang, PhD thesis, Univ. of Pittsburgh (1993).

[53] B. Hong, PhD thesis, SUNY at Stony Brook (1995).

[54] J. Dee, PhD thesis, SUNY at Stony Brook (1995).

[55] Y. Zhang, PhD thesis, SUNY at Stony Brook (1995).

[56] C. Zou, PhD thesis, SUNY at Stony Brook (1996).

[57] T. Piazza, PhD thesis, SUNY at Stony Brook (1997).

[58] J. Barrette *et al.*, E877 Collaboration, Nucl. Phys. **A590**,(1995) 259c and references therein.

[59] L. Bravina, L. P. Csernai, P. Levai, D. Strottman Phys. Rev. **C50** (1994) 2161.

[60] M. Gilkes, private communication.

[61] J. Stachel, P. Braun-Munzinger, Phys. Lett. **B216**, 1 (1989); Nucl. Phys. **A498**, 577c (1989).

[62] T. Alber *et al.*, NA49 Collaboration, Phys. Rev. Lett. **75**, 3814 (1995)

[63] J. Stachel, private communication.

[64] K. Shigaki, PhD thesis, Univ. of Tokyo (1995).

Appendix A

The Fourier Moments

The general concept of Fourier moments is that the first moment causes a overall shift of a 2-d distribution off the origin and the second moment generates an elliptical shape. It would be useful to establish the relationships between the Fourier moments and geometrical quantities, like the distance of the center from the origin and the eccentricity. We provide a mathematical derivation and a graphical demonstration for the even terms of Fourier moments ($\cos(n\phi)$).

Let us start with the zeroth moment of the Fourier series of an azimuthal distribution which represents a circular distribution in the polar coordinate with the radius characterizing the density. This could be expressed in term of a radius function $r(\phi)$ or the Cartesian coordinate x_0, and y_0 as,

$$\frac{dN}{d\phi} = r(\phi) = r_0 = \sqrt{x_0^2 + y_0^2}. \tag{A.1}$$

If there exists only the perturbation of the first moment v_1, up to the order of v_1^2 accuracy, then

$$\begin{aligned}
\frac{dN}{d\phi} &= r_0(1 + 2v_1 \cos\phi) && \text{(A.2)}\\
&\simeq r_0(1 + 4v_1 \cos\phi)^{1/2} && \text{(A.3)}\\
&\simeq (r_0^2 + 4v_1 r_0^2 \cos\phi)^{1/2} && \text{(A.4)}\\
&\simeq (x_0^2 + y_0^2 + 4v_1 r_0 x_0)^{1/2} && \text{(A.5)}\\
&\simeq \left([x_0 + 2v_1 r_0]^2 + y_0^2\right)^{1/2} && \text{(A.6)}
\end{aligned}$$

which can be viewed as an approximation of a shift of the center along x axis by $2v_1 r_0$ with the requirement of the shift being much less than r_0, i.e. $v_1 \ll 1$.

The widely used mean transverse momentum projected in the direction of the reaction plane, $\langle p_x \rangle$, can be evaluated

$$\langle p_x \rangle = \frac{\int \frac{d^2N}{dp_t d\phi}(p_t \cos\phi) dp_t d\phi}{\int \frac{d^2N}{dp_t d\phi} dp_t d\phi} \tag{A.7}$$

$$= \langle p_t v_1(p_t) \rangle \tag{A.8}$$

and the average in Eq. A.8 is over the transverse momentum p_t.

The case of second moment can be done in the similar way,

$$\frac{dN}{d\phi} = r_0(1 + 2v_2 \cos 2\phi) \tag{A.9}$$

$$\simeq r_0(1 + 4v_2 \cos 2\phi)^{1/2} \tag{A.10}$$

$$\simeq (r_0^2 + 4v_2 r_0^2(\cos^2\phi - \sin^2\phi))^{1/2} \tag{A.11}$$

$$\simeq (x_0^2 + y_0^2 + 4v_2 x_0^2 - 4v_2 y_0^2)^{1/2} \tag{A.12}$$

$$\simeq \left([(1 + 2v_2)x_0]^2 + [(1 - 2v_2)y_0]^2\right)^{1/2} \tag{A.13}$$

which is a simultaneous scaling of the x and y axes and represents an elliptical shape.

In NA49's report of an elliptical event shape, the flow signal is defined as [37],

$$p'_x = \lambda_x \cdot p_x = (1 + \epsilon) \cdot p_x \tag{A.14}$$

$$p'_y = \lambda_y \cdot p_y = (1 - \epsilon) \cdot p_y \tag{A.15}$$

$$R_p = (\frac{\lambda_y}{\lambda_x})^2 \tag{A.16}$$

where a manual distortion of an originally circular distribution is implemented.

With the assumption of $\lambda_x > \lambda_y$ (the major axis lying in the x axis) and $\epsilon \ll 1$, the relationship between R_p and v_2, the second even Fourier moments in the transverse momentum distribution $dp_t/d\phi$, is derived in the following up to the first order of ϵ in approximation.

$$\phi' = \arctan(\frac{p'_y}{p'_x}) \tag{A.17}$$

$$= \phi + \Delta\phi \tag{A.18}$$

$$\tan\phi' = \frac{p'_y}{p'_x} = \frac{1 - \epsilon}{1 + \epsilon} \tan\phi \tag{A.19}$$

$$
\begin{aligned}
&= \tan(\phi + \Delta\phi) && \text{(A.20)}\\
&= \tan\phi + \Delta\phi \sec^2\phi && \text{(A.21)}\\
\Delta\phi &= -\epsilon \sin 2\phi && \text{(A.22)}
\end{aligned}
$$

and,

$$
\begin{aligned}
p_t' &= \sqrt{(\lambda_x\, p_x)^2 + (\lambda_y\, p_y)^2} && \text{(A.23)}\\
&= (1 + \epsilon \cos 2\phi) p_t, && \text{(A.24)}
\end{aligned}
$$

so that

$$
\begin{aligned}
\frac{dp_t'}{d\phi'} &= \frac{1 + \epsilon \cos 2\phi}{1 - 2\epsilon \cos 2\phi} \frac{dp_t}{d\phi} && \text{(A.25)}\\
&\propto (1 + 3\epsilon \cos 2\phi) && \text{(A.26)}\\
2\, v_2 &= 3\epsilon && \text{(A.27)}\\
R_p &= (\frac{1 + \frac{3}{2} v_2}{1 - \frac{3}{2} v_2})^2. && \text{(A.28)}
\end{aligned}
$$

As for the third moment,

$$
\begin{aligned}
\frac{dN}{d\phi} &= r_0(1 + 2v_3 \cos 3\phi) && \text{(A.29)}\\
&\simeq r_0(1 + 4v_3 \cos 3\phi)^{1/2} && \text{(A.30)}\\
&\simeq (r_0^2 + 4v_3 r_0^2(\cos^3\phi - 3\sin^2\phi\cos\phi))^{1/2} && \text{(A.31)}\\
&\simeq (x_0^2 + y_0^2 + 4\frac{v_3}{r_0} x_0^3 - 3\frac{v_3}{r_0} y_0^2 x_0)^{1/2} && \text{(A.32)}\\
&\simeq \left([(1 + 2v_3 \frac{x_0}{r_0}) x_0]^2 + [(1 - \frac{3}{2} v_3 \frac{x_0}{r_0}) y_0]^2\right)^{1/2} && \text{(A.33)}
\end{aligned}
$$

which is the scaling of the coordinates, but the scaling factors depend on the position of x_0. The validity of the approximation is that $v_3 x_0/r_0 \ll 1$ is satisfied.

In principle, this interpretation can be extended to higher moments. We show graphical results in Fig. A.1, A.2, A.3, and A.4 up to the $4th$ moments. Observation of these figures shows that the first moment effectively shifts the center of distribution and changes the circular shape simultaneously. The other higher moments only deform the overall shape symmetrically.

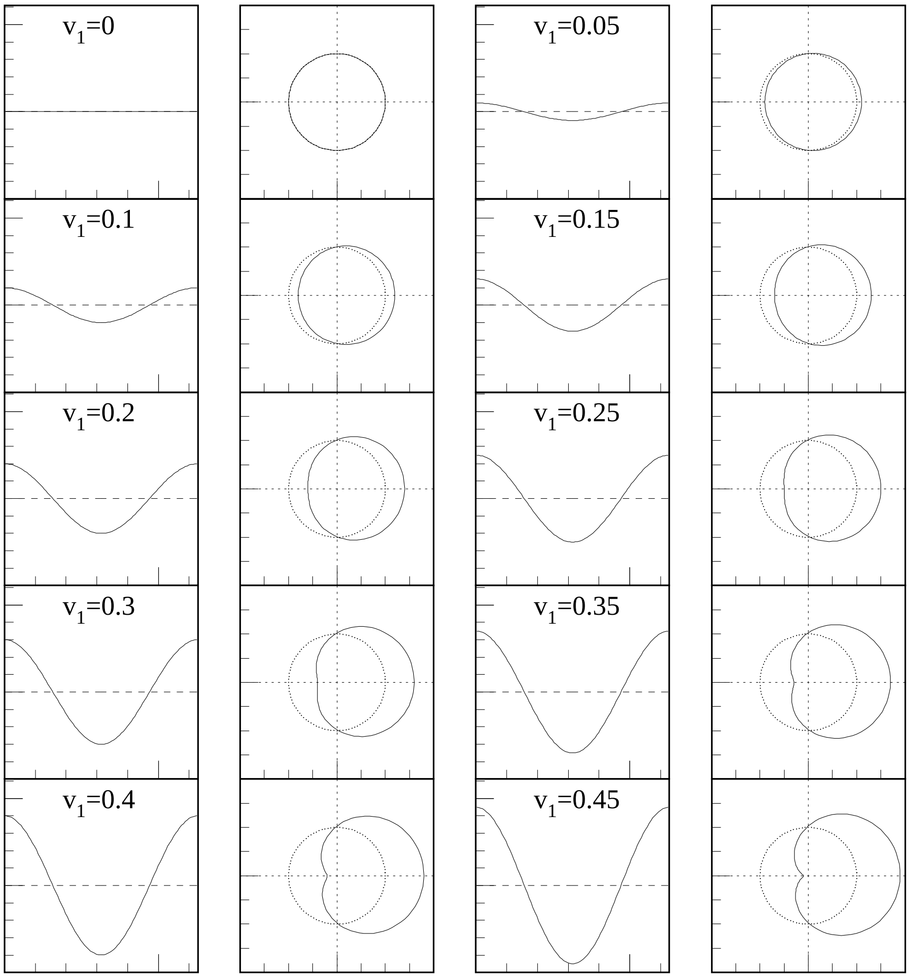

Figure A.1: The azimuthal distribution and representation in polar coordinate of $dN/d\phi = (1 + 2v_1 \cos\phi)$, with v_1 from 0 to 0.45 in steps of 0.05

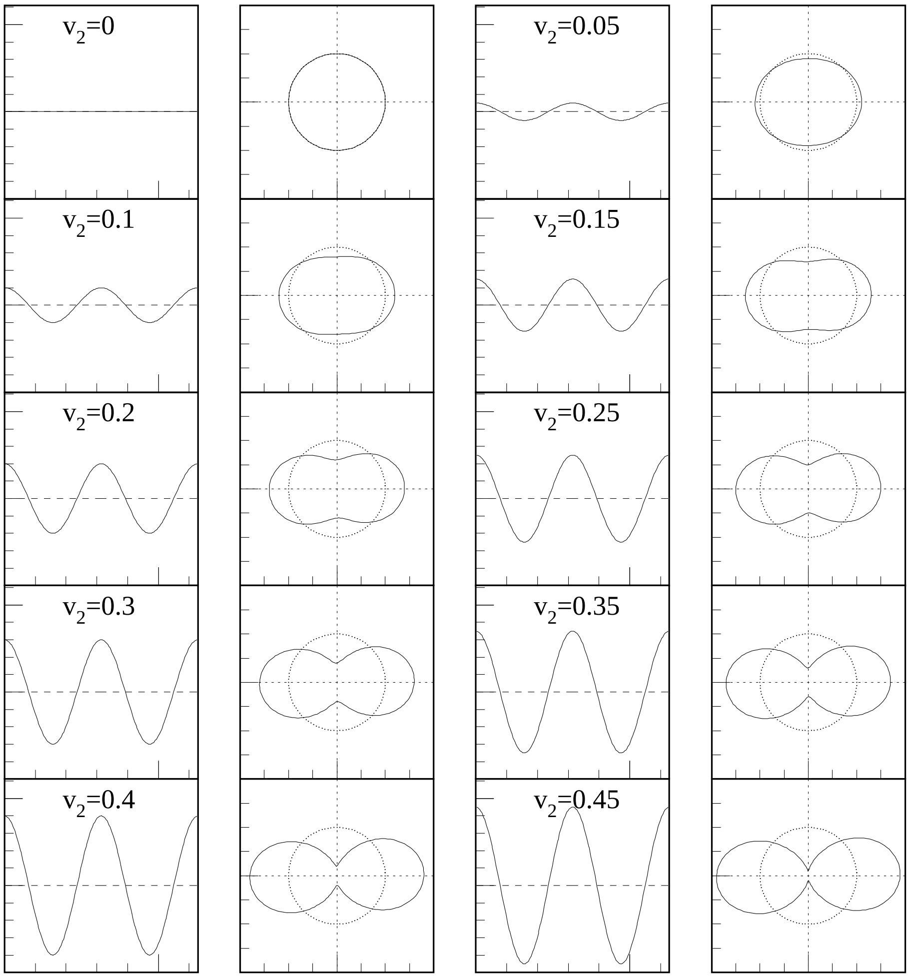

Figure A.2: The azimuthal distribution and representation in polar coordinate of $dN/d\phi = (1 + 2v_2 \cos 2\phi)$, with v_2 from 0 to 0.45 in steps of 0.05

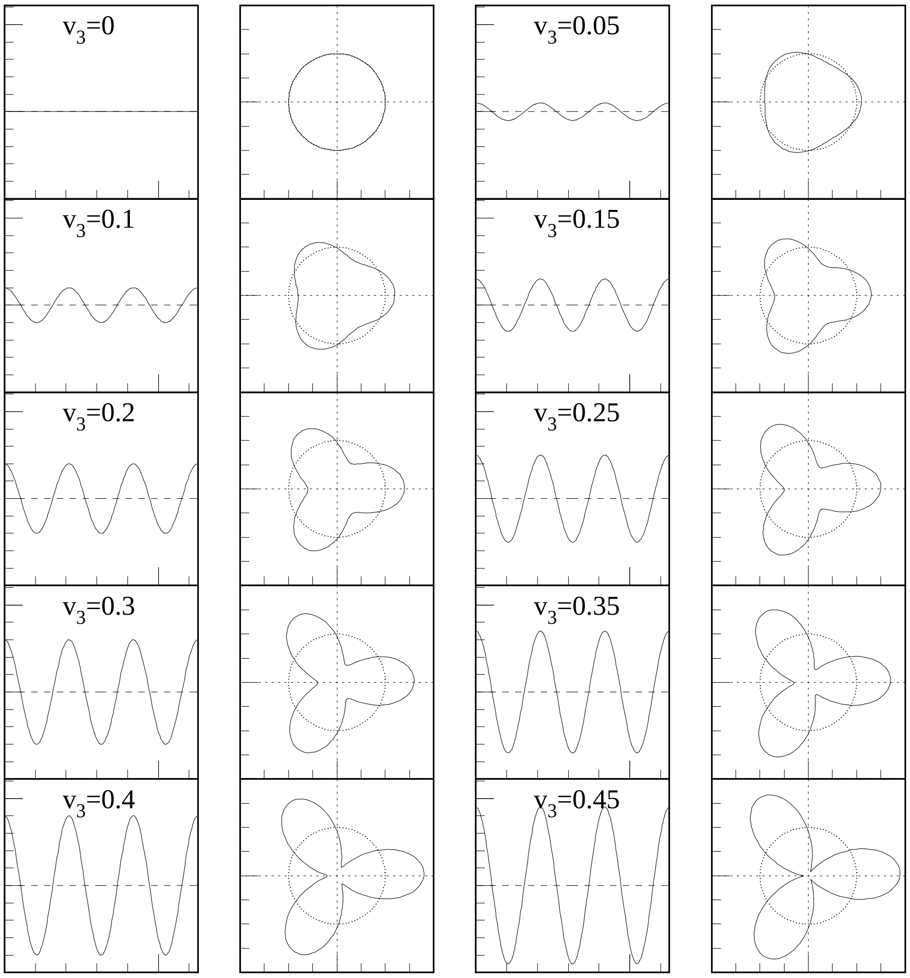

Figure A.3: The azimuthal distribution and representation in polar coordinate of $dN/d\phi = (1 + 2v_3 \cos 3\phi)$, with v_3 from 0 to 0.45 in steps of 0.05

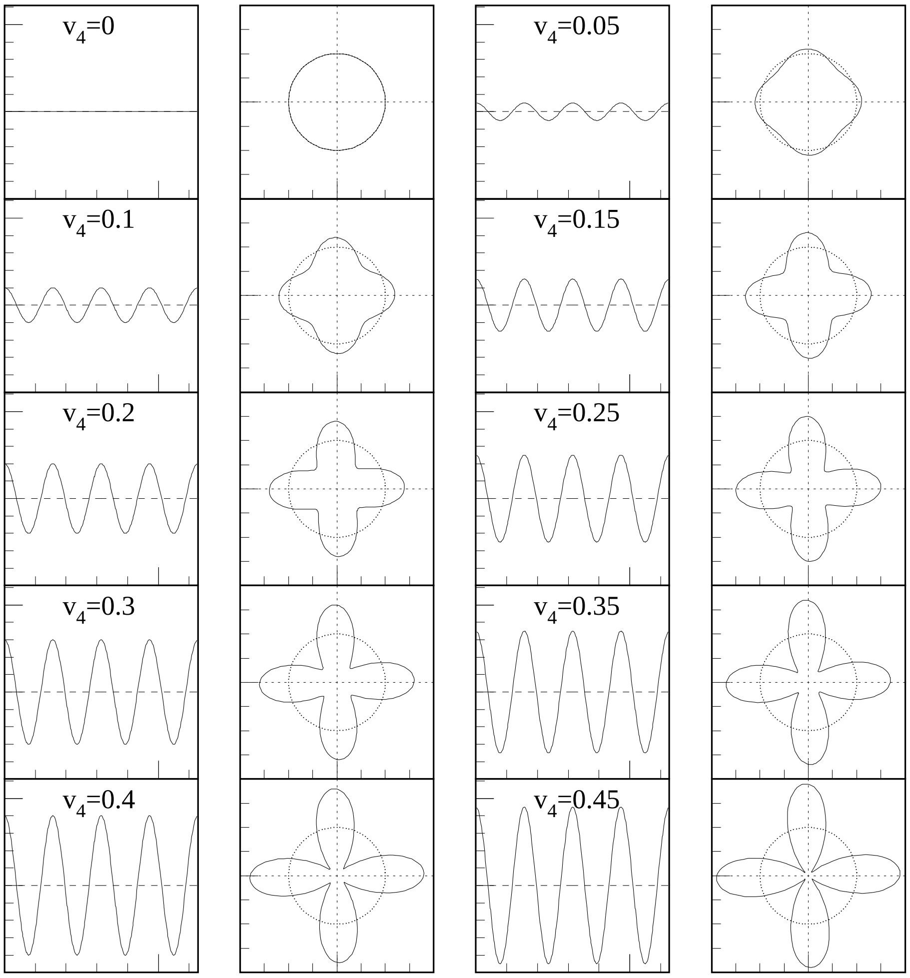

Figure A.4: The azimuthal distribution and representation in polar coordinate of $dN/d\phi = (1 + 2v_4 \cos 4\phi)$, with v_4 from 0 to 0.45 in steps of 0.05

Appendix B

The Fireball Model

A simple hydrodynamic model with two free parameters (s_0 and σ_y) [61] gives a reasonable description of the global distributions of charged multiplicities and transverse energy of Au + Au collision measured by E877 in Fig. B.1. It is used as a quick event generator to process through the GEANT simulation in the calibration of the PCAL.

In this model, the velocity and excitation energy of the formed fireball are determined by the overlapping sharp-cut collision geometry and the stopping fraction S. Full stopping is assumed in the central collision and the stopping fraction S (the ratio of number of fully stopped nucleons to the total number of nucleons in the participant zone) is parameterized as a profile function of the mass number of colliding nuclei($A_{T,P}$), impact parameter(b) and the parameter s_0 as

$$\begin{aligned} S(\text{stoppingfraction}) &= \min(1, s_0 \cdot A_T^{1/3} \cdot \sqrt{1 - \frac{b^2}{(R_P + R_T)^2}}) && \text{(B.1)} \\ R_{T,P}(\text{radius}) &= 1.2\text{fm} \cdot A_{T,P}^{1/3}. && \text{(B.2)} \end{aligned}$$

The relationship between stopping fraction, impact parameter, and centrality experimentally defined by the transverse energy production into the acceptance of PCAL calorimeter for different targets for Au beam are shown in Fig. B.2.

In the rest frame of the fireball, the longitudinal and transverse momentum distributions are decoupled instead of an isotropic thermal source. The emitting particles are sampled by the Monte-Carlo method according to the factorized probability distribution of a Gaussian rapidity distribution and a thermal transverse momentum spectrum,

$$f(y, p_T) \propto \exp(-\frac{y - y_f}{2\sigma_y^2})\sqrt{m_t}\exp(-\frac{m_t}{T}). \qquad \text{(B.3)}$$

The width of rapidity distribution (σ_y) is the one parameter tuned to fit the data and the freeze-out temperature T is fixed to be 0.15 GeV.

The emitted particles include only the constituent nucleons of the fireball and pions. The order of emitting species of particles is as follows: protons are sampled first to conserve the total charge of the participant ,then neutrons, to conserve the baryon number, and finally three species of pions are equally possible to be emitted until we have exhausted the available excitation energy.

The width of the high-energy tails of the E_T distributions reflects the fluctuations of energy density in the most central collision. We implement the consideration of the intrinsic deformed shape of the nuclei and random relative orientation of deformed nuclei in the model. The transverse energy distribution of Au + U is reproduced by using the same set of parameters which describes the collision of Au + Au. So the extra fluctuations of the high E_T tail in Au + U collision compared to Au + Au collision can be understood as the increase of target mass and the deformed geometry with the same scheme of stopping and particle emission. The prediction of U + U at AGS energy by this model is shown in Fig. B.3 and found out to be 1.2 times larger in the mean (350/300) and 1.6 larger in the width (50/30) of produced E_T in the most central collisions. This long tail may be effective in forming the nuclear matter of high energy and baryon density. At CERN energies, the high E_T tail of Pb + Pb collision can also be well reproduced by another set of parameters, shown in Fig. B.4.

Overall this simple phenomenological model is shown to describe the general global distributions at both AGS and CERN energies and is useful in understanding the fluctuations of produced E_T in central collisions. This might mean that these global features are not very sensitive to the details of dynamics. The advantage of its quickness in generating events makes it a good tool in simulation work.

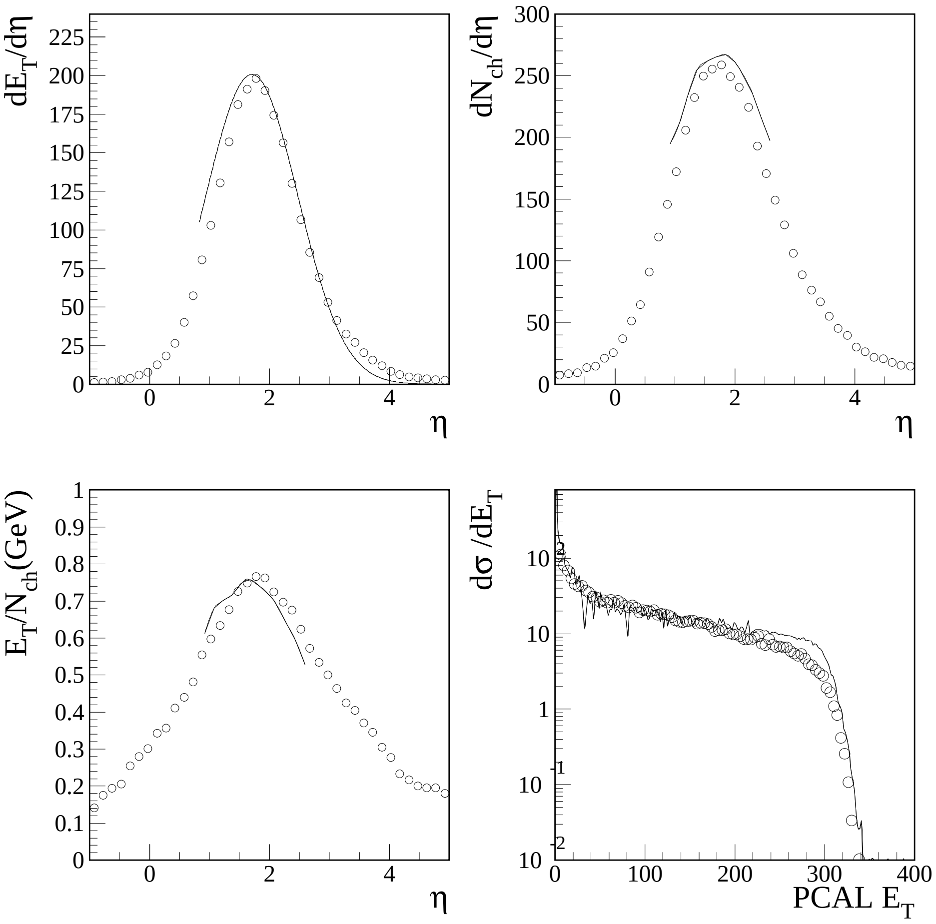

Figure B.1: With the set of parameters ($s_0 = 0.23$, $\sigma_y = 0.7$), the fireball model(open circle) reproduces the pseudo-rapidity distribution of transverse energy E_T, charged multiplicity N_{ch} and transverse energy per charged particle and the transverse energy distribution represented by lines.

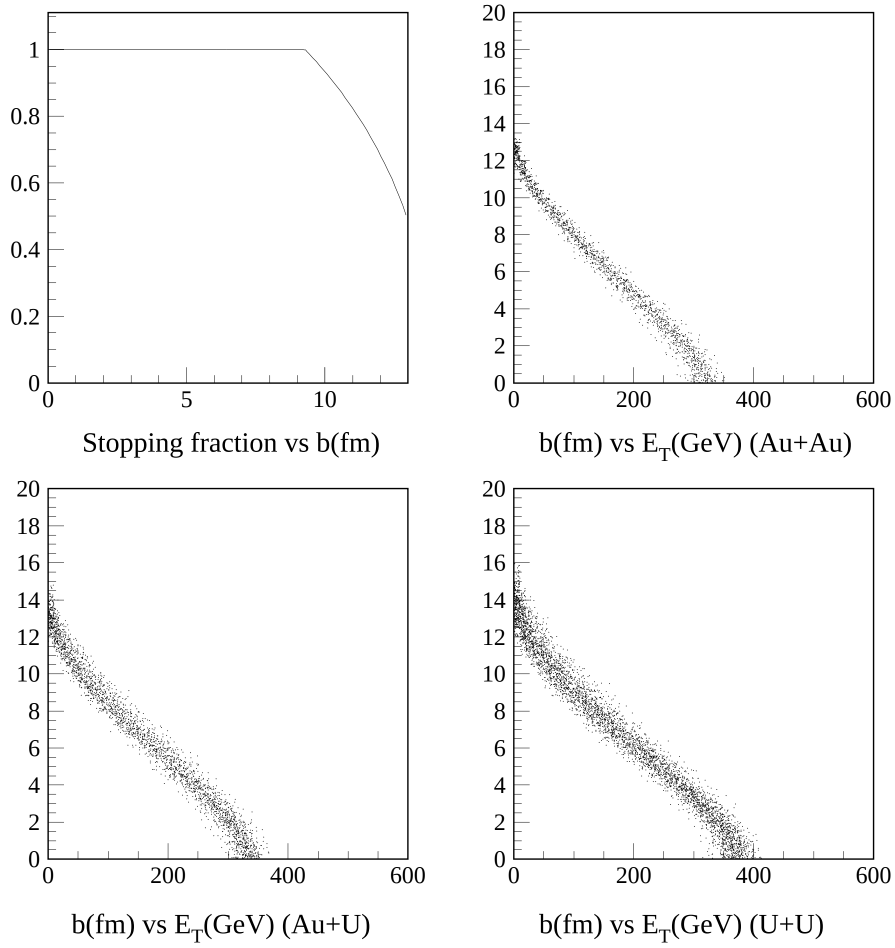

Figure B.2: The stopping fraction S is plotted as a function of impact parameter b and the correlation between b and produced transverse energy within the η acceptance of PCAL ($0.8 < \eta < 4.3$) are shown for different combinations of colliding nuclei.

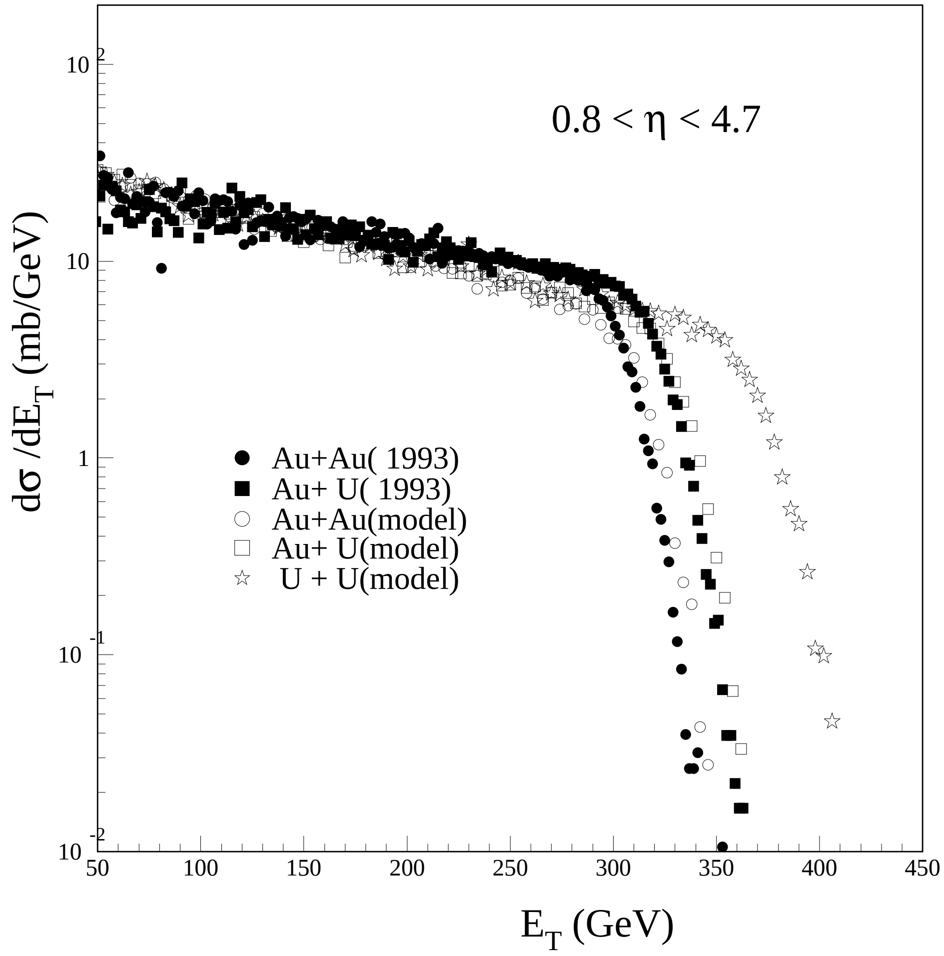

Figure B.3: The measurements and model calculations of transverse energy distributions of different colliding systems at AGS 10.8 A GeV.

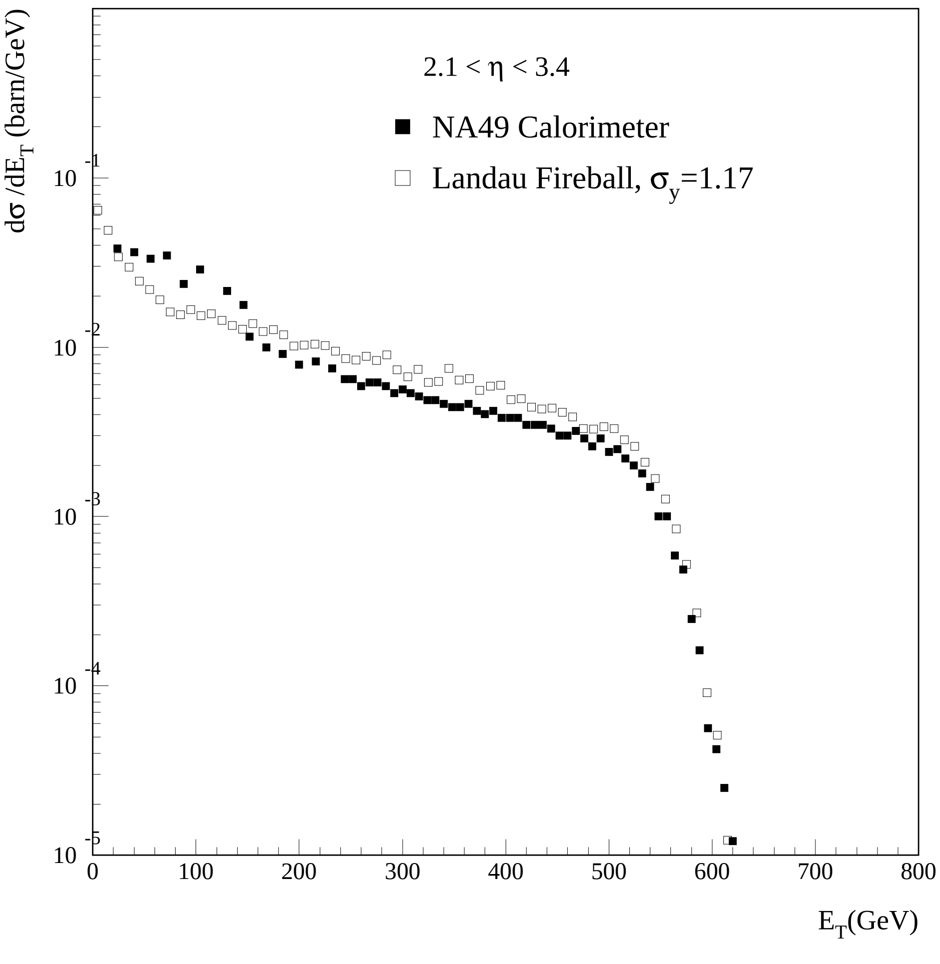

Figure B.4: The NA49 measurement [62] and model calculations of the transverse energy distribution of Pb + Pb collisions at CERN 160 A GeV.

Appendix C

The Parameterization of Phase Space

Phase space can be parameterized as a function of the inverse slope parameter $T_B(y)$ and rapidity distribution dN/dy which is determined by the measured p_t spectrum.

$$\frac{d^2N}{p_t dp_t dy} = \frac{d^2N}{m_t dm_t dy} = (N_0(y)\frac{m_t}{m}\exp(\frac{m}{T_B}))\exp(-\frac{m_t}{T_B}) \tag{C.1}$$

where the normalization $N_0(y)$ can be expressed in term of T_B and dN/dy by the following equations,

$$\begin{aligned} \frac{dN}{dy} &= \int_m^\infty \frac{d^2N}{dm_t dy} dm_t \\ &= N_0 m T_B (1 + 2\frac{T_B}{m} + 2\frac{T_B^2}{m^2}) \end{aligned} \tag{C.2}$$

$$N_0 = \frac{\frac{dN}{dy}}{mT_B(1 + 2\frac{T_B}{m} + 2\frac{T_B^2}{m^2})} \tag{C.3}$$

For the pseudo-rapidity distribution,

$$\frac{dN}{d\eta} = \int_m^\infty \frac{d^2N}{dp_t d\eta} dp_t \tag{C.4}$$

$$= \int_m^\infty \frac{d^2N}{dp_t dy}\frac{dy}{d\eta} dp_t \tag{C.5}$$

$$\frac{dE_T}{d\eta} = \int_m^\infty \frac{d^2N}{dp_t dy}\frac{dy}{d\eta} E_T dp_t. \tag{C.6}$$

The Jacobian of the transformation $dy/d\eta$:

$$y = 0.5 \cdot \ln(\frac{E+P_z}{E-P_z}) \tag{C.7}$$

$$\eta = 0.5 \cdot \ln(\frac{P+P_z}{P-P_z}) \tag{C.8}$$

$$y = \ln(\frac{\sqrt{p_t^2 \cosh^2 y + m^2} + p_t \sinh y}{m_t}) \tag{C.9}$$

$$\frac{dy}{d\eta} = \frac{\frac{p_t^2 \cosh\eta \sinh\eta}{\sqrt{p_t^2 \cosh^2 y + m^2}} + p_t \cosh\eta}{\sqrt{p_t^2 \cosh^2 y + m^2} + p_t \sinh\eta}. \tag{C.10}$$

The weighting transverse energy E_T is different for nucleons and pions [55]. For pions,

$$E_T = E \sin\theta = E\frac{p_t}{P} = \frac{m_t \cosh y}{\sqrt{m_t^2 \cosh^2 y - m^2}}\, p_t. \tag{C.11}$$

For nucleons, which only lose kinetic energy in the calorimetry,

$$E_T = (E-m)\sin\theta = \sqrt{\frac{m_t \cosh y - m}{m_t \cosh y + m}}\, p_t. \tag{C.12}$$

In Fig. C.1, based on the measurement by E877 and E866 for Au + Au , $T_B(y)$ and dN/dy of protons and negative pions for the top 4% centrality could be parameterized as [63]

$$\text{proton}, T_B(y) = 0.26\text{GeV} \cdot \exp(-\frac{(y-1.6)^2}{2\cdot(1.06)^2}) \tag{C.13}$$

$$\frac{dN}{dy} = 67 \cdot \exp(-\frac{(y-1.6)^2}{2\cdot(0.89)^2}) \tag{C.14}$$

$$\text{negative pion}, T_B(y) = 0.15\text{GeV} \cdot \exp(-\frac{(y-1.6)^2}{2\cdot(1.70)^2}) \tag{C.15}$$

$$\frac{dN}{dy} = 76 \cdot \exp(-\frac{(y-1.6)^2}{2\cdot(0.88)^2}). \tag{C.16}$$

By taking the above parameterization, the pseudo-rapidity distribution of charged multiplicity and transverse energy is calculated and compared with measurements by E877 in Fig. C.2. And the calculated relationships between pseudo-rapidity(η) and rapidity(y) and the mean transverse momentum as a function of rapidity for protons and pions are shown in Fig. C.3. They are used in mapping the disentangled nucleon and pion flow in pseudo-rapidity(η) into the rapidity space to get the $\langle p_x \rangle$ described in Chapter. 7.

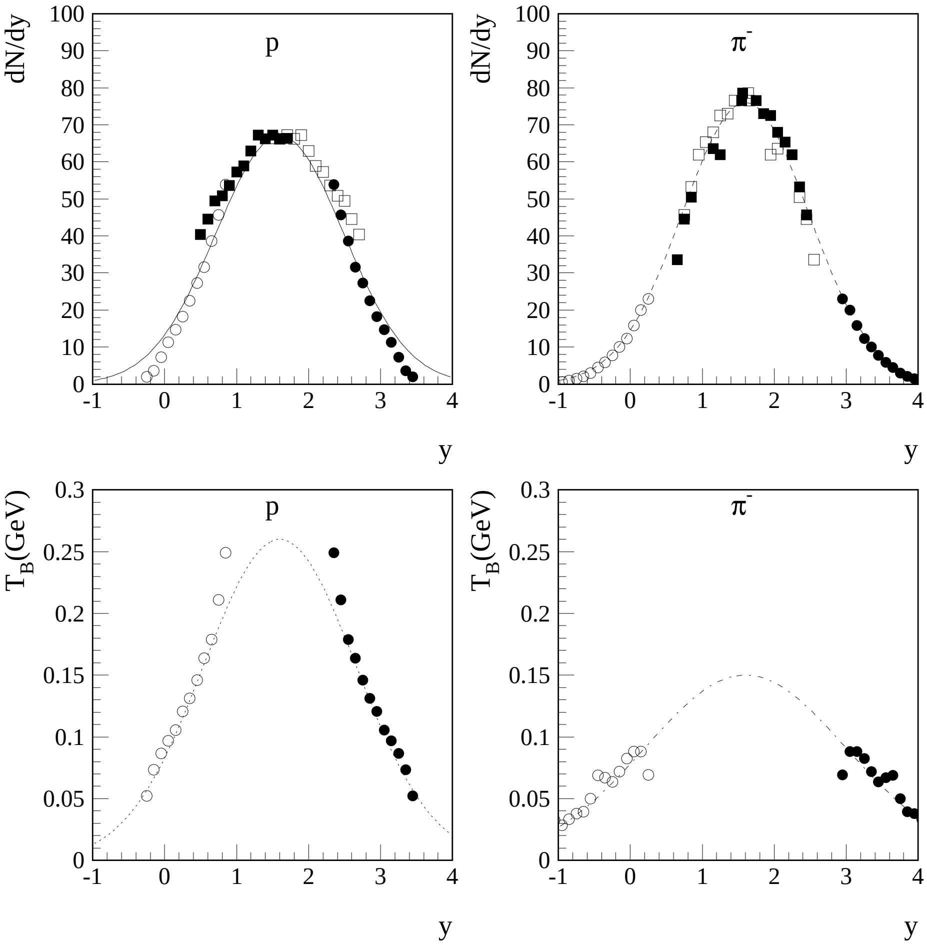

Figure C.1: The parameterization(curve) is plotted with the measurements by E866(square) and E877(circle). The open symbols are reflections about mid-rapidity.

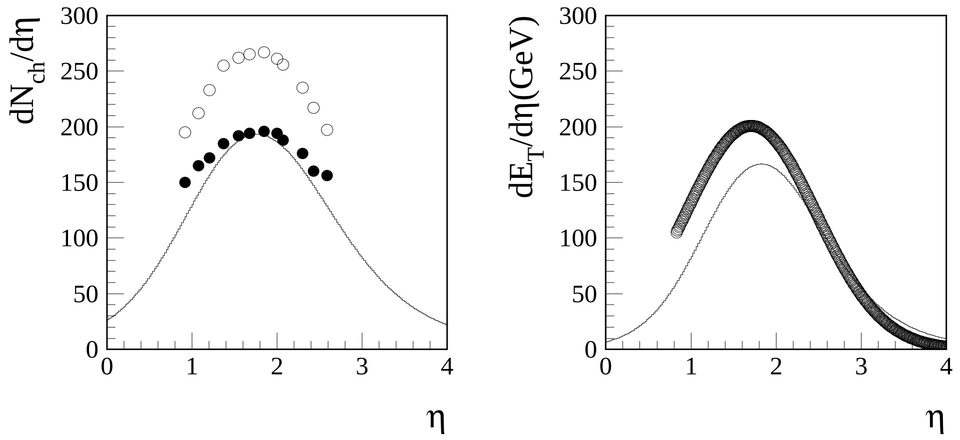

Figure C.2: The pseudo-rapidity distribution(curve) of charged multiplicity(left) and transverse energy(right) is calculated and compared with the E877 measurements

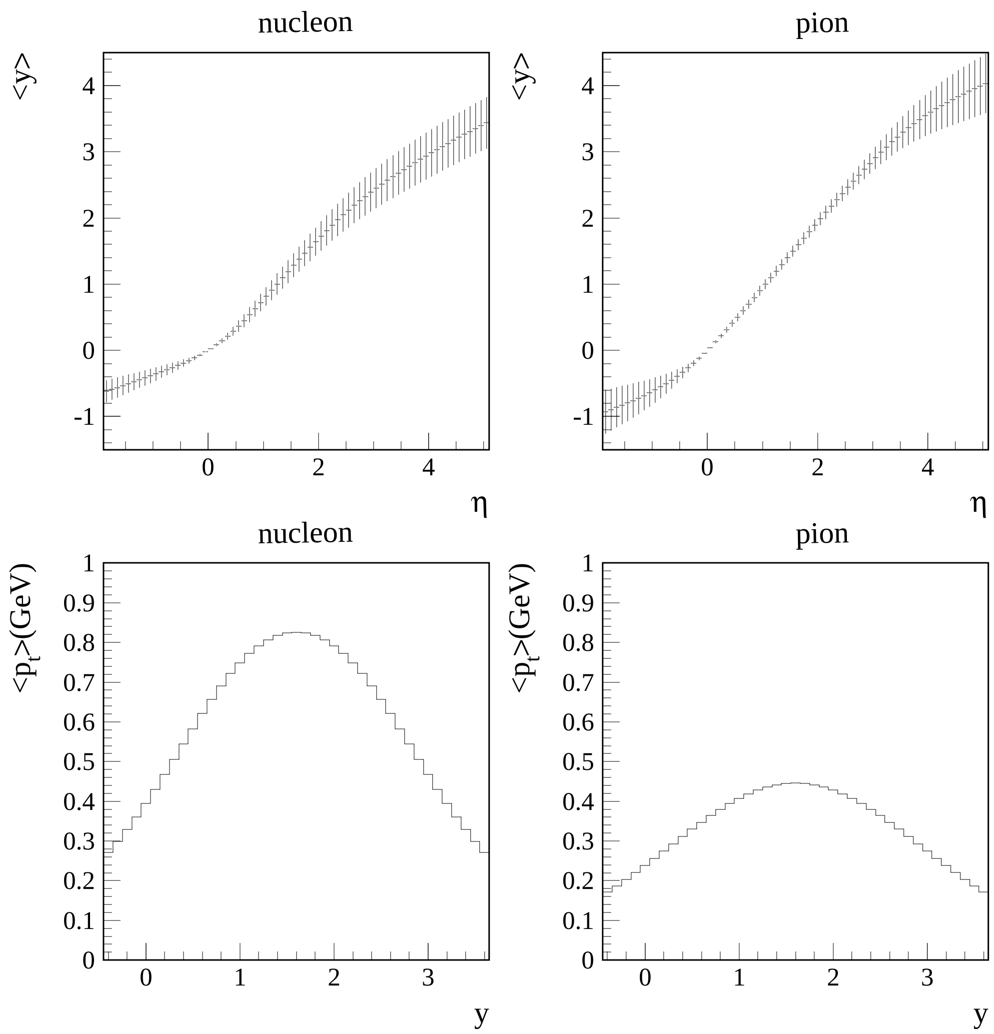

Figure C.3: The calculated mean rapidity($\langle y \rangle$) as a function of pseudo-rapidity (η) and the mean transverse momentum as a function of rapidity for protons and pions.

Appendix D

Particle Identification and Occupancy Correction

D.1 Particle Identification

Before making any particle identification we apply the following selection criteria to the tracks found in the spectrometer:

1. "software" collimator geometrical acceptance cut:
   `(px/pz.lt.-0.140 .and. px/pz.gt.0.007`
   `.and. py/pz.lt.-0.008 .and. py/pz.gt.0.010)`,

2. p_y information is required (vertical information from at least one of drift chambers)

3. Y position matching in DC2, DC3, and TOFU:
   `(((abs(py/pz*5380000.-dc2y).lt.6000.) .or.`
   `(abs(py/pz*11600000.-dc3y).lt.4000.))) .and.`
   `(abs(py/pz*12290000.-tofy).lt.30000)`,

4. TOFU pulse height cut:
   `(tofph.gt.0.85 .and. tofph.lt.(1.3+0.025*(toft-path)))`,

5. single track pointing to one TOFU slat,

6. track does not go through drift chamber dead regions,

7. TOFU slats considered as "non-reliable" are removed from the analysis.

8. p_x cut (`px.lt.0`). To avoid interactions with the edges of collimator.

where

`px, py, pz`	:	the momentum components of tracks
`dc2y`	:	the measured y positions of tracks on DC2
`dc3y`	:	the measured y positions of tracks on DC3
`tofy`	:	the measured y positions of tracks on TOFU
`tofph`	:	the pulse height of tracks on TOFU
`toft`	:	the time of flight of tracks measured by TOFU
`path`	:	path length of tracks from the target to TOFU

Particle identification is made in accordance to the value of calculated mass squared m^2 for good tracks. In the experiment, there are three measurables related to a particle: momentum (p), time of flight (TOF), and flight path length (L). From them, we calculate the mass squared as

$$m^2 = p^2(\frac{1}{\beta^2} - 1) = p^2((\frac{TOF}{L})^2 - 1), \tag{D.1}$$

where β is the particle velocity.

According to [64] the resolution in reconstructed mass-squared consists of two parts, the momentum resolution of the tracking system and the time resolution of the time of flight system. This is true under the assumption of constant time of flight resolution. In this case the mass squared resolution could be written as a function of momentum:

$$\begin{aligned} \sigma^2_{m^2} &= 4m_0^2(\frac{\sigma_p}{p})^2 + \frac{4p^4}{\beta^2}(\frac{\sigma_{TOF}}{L})^2 \\ &= c_1^2(4m_0^4p^2) + c_2^2(4m_0^4(1 + \frac{m_0^2}{p^2})) + c_3^2(4p^2(m_0^2 + p^2)), \end{aligned} \tag{D.2}$$

where

$\sigma^2_{m^2}$	:	the resolution of reconstructed mass squared
m_0	:	assumed known mass of the particle
p	:	measured momentum of the particle
σ_p	:	momentum resolution
σ_{TOF}	:	time of flight resolution
L	:	flight path length

Field	A Field		B Field	
particle	p	π	p	π
c_1	0.0087	0.0611	0.0087	0.0611
c_2	0.0390	0.1093	0.0390	0.1093
c_3	0.00189	0.00183	0.00189	0.00183

Table D.1: The parameters of particle identification in 93 data

and c_1, c_2, c_3 are coefficients representing the angular resolution, multiple scattering and time of flight resolution respectively.

Fits of the m^2 distribution around the peak in each momentum slice by a Gaussian distribution provides the mean value of m_0^2 and the width $\sigma_{m^2}^2$ as a function of momentum p. The width is then fitted with the formula (D.2). The obtained values of c_1, c_2, c_3 for proton and charged pions are shown in the Table D.1 for different magnetic field polarities.

Particle identification is performed by selecting hits within some range proportional to σ_{m^2} about the mean value of m^2 in each momentum slice. In the order to get a clean identification and to eliminate contamination of e^+, e^- in the low momentum region and misidentified tracks from charged pion samples, we impose a stringent cut of $1.5\,\sigma$ around m_0^2. The fitted mean of m^2 fluctuates around $m^2 = m_0^2$, we use a polynomial to parameterize it as a function of p. In order to avoid possible mixing of particles in the high momentum region, we require a high momentum cut to clean the possible misidentification,
`(p.lt.11)` for protons to prevent contamination from deuterons, and
`(p.lt.6)` for pions to prevent kaons or protons.

The particle identification in $p - m^2$ and $1/p - TOF$ plots is shown in Fig. D.1. The experimental acceptance of the spectrometer in two different configurations of the magnetic field (A,B) can be seen in Fig. D.2.

D.2 Occupancy Correction

It is known that the efficiency of the reconstruction of two tracks close in DC2 and/or DC3 (with relative separation less than 1 cm and 2 cm, respectively) is relatively low. The number of lost tracks in this case is proportional to the total number of tracks in the spectrometer, or to the spectrometer occupancy.

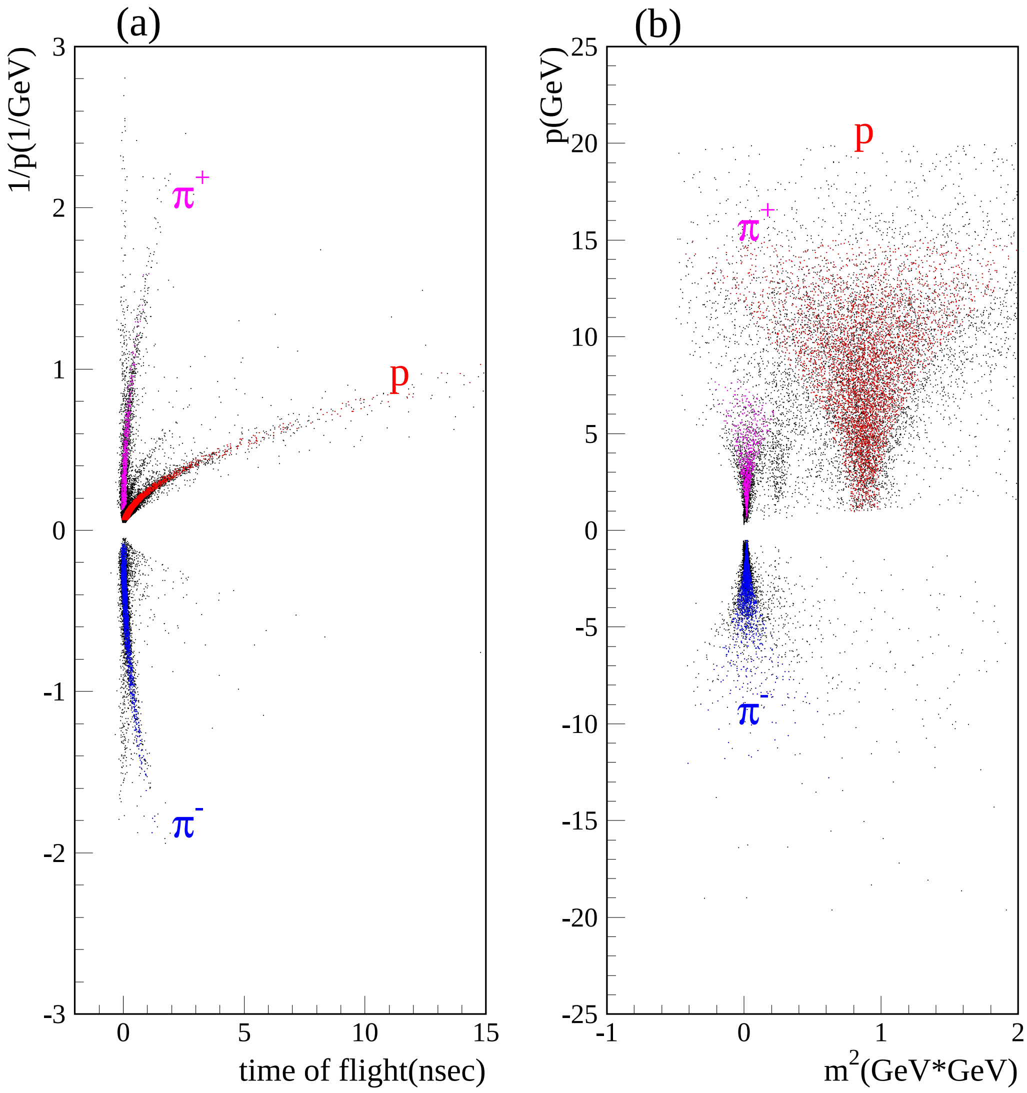

Figure D.1: (a) Particle identification in a $1/p$ versus time-of-flight plot. (b) Particle identification in a p versus m^2 plot.

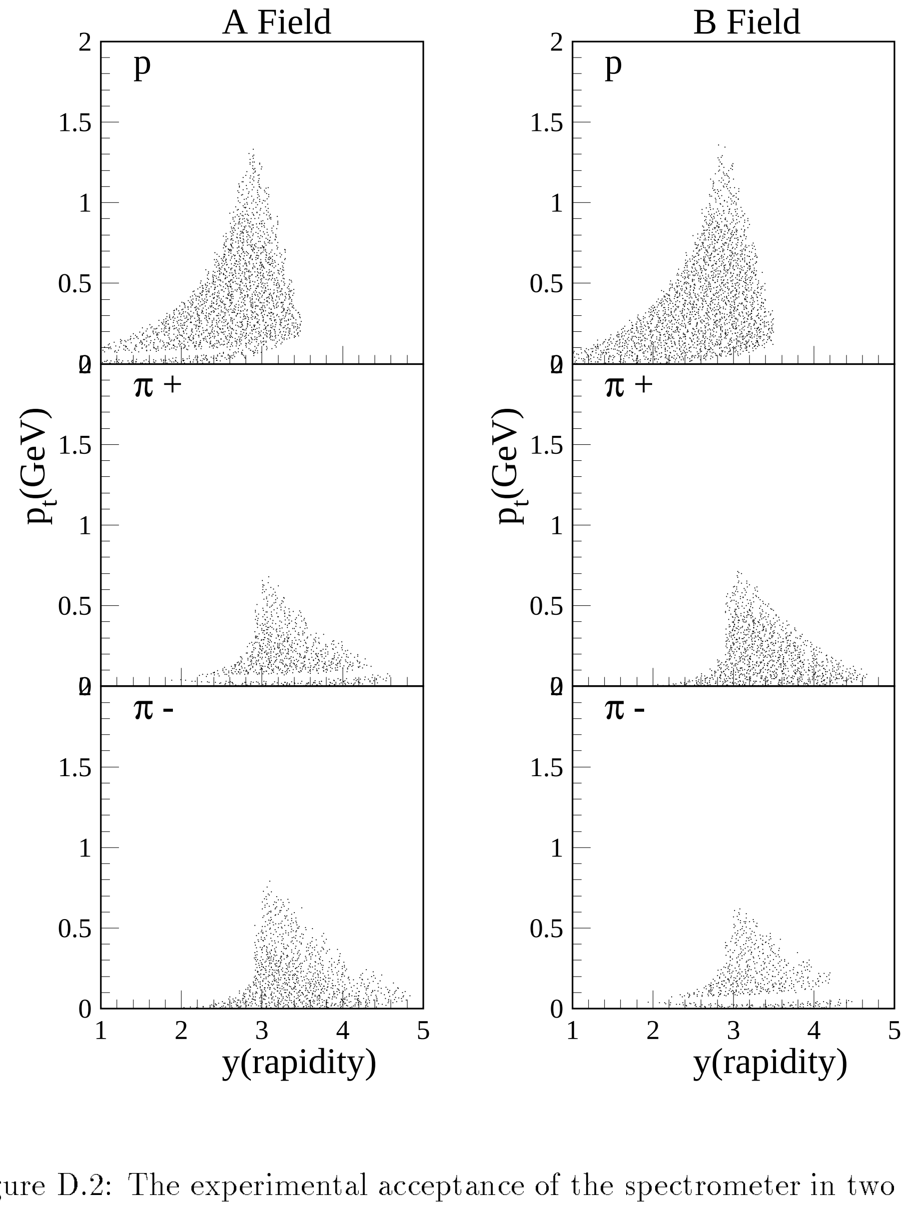

Figure D.2: The experimental acceptance of the spectrometer in two configurations of the magnetic fields.

The correction for these lost tracks is called "the occupancy correction". The mean number of tracks in the spectrometer depends on the centrality and on the reaction plane angle. The dependence is shown in Fig. D.3 and D.4. The occupancy is higher for events with the reaction plane orientation into the spectrometer (which lies on the plane of $x < 0$ corresponding to $\Psi_1 = \pi$), and consequently the efficiency of tracking is lower with more lost tracks (Fig. D.5). This effect of underestimating the number of real tracks tends to decrease the azimuthal anisotropy and thus underestimate the strength of the real flow signal. The estimate of maximum possible bias in the first moment v_1 due to the tracking efficiency dependence on occupancy is about 2%.

We apply the prescription of occupancy correction described in Ref [36] by assigning extra weight equal to 1.5 to any track each time it has another track found in the vicinity of minimum separation (DC2: 1 cm, DC3: 2 cm). This procedure has the advantage of getting the weight of occupancy correction, which may have various dependences on the centrality, reaction plane orientation etc, directly from the experimental data.

In Fig. D.6, we show the dependencies of the occupancy correction for identified protons on the transverse momentum p_t , the centrality of events, the orientation of the reaction plane and rapidity. The weights of pion tracks show similar dependency, however they are less than those of protons.

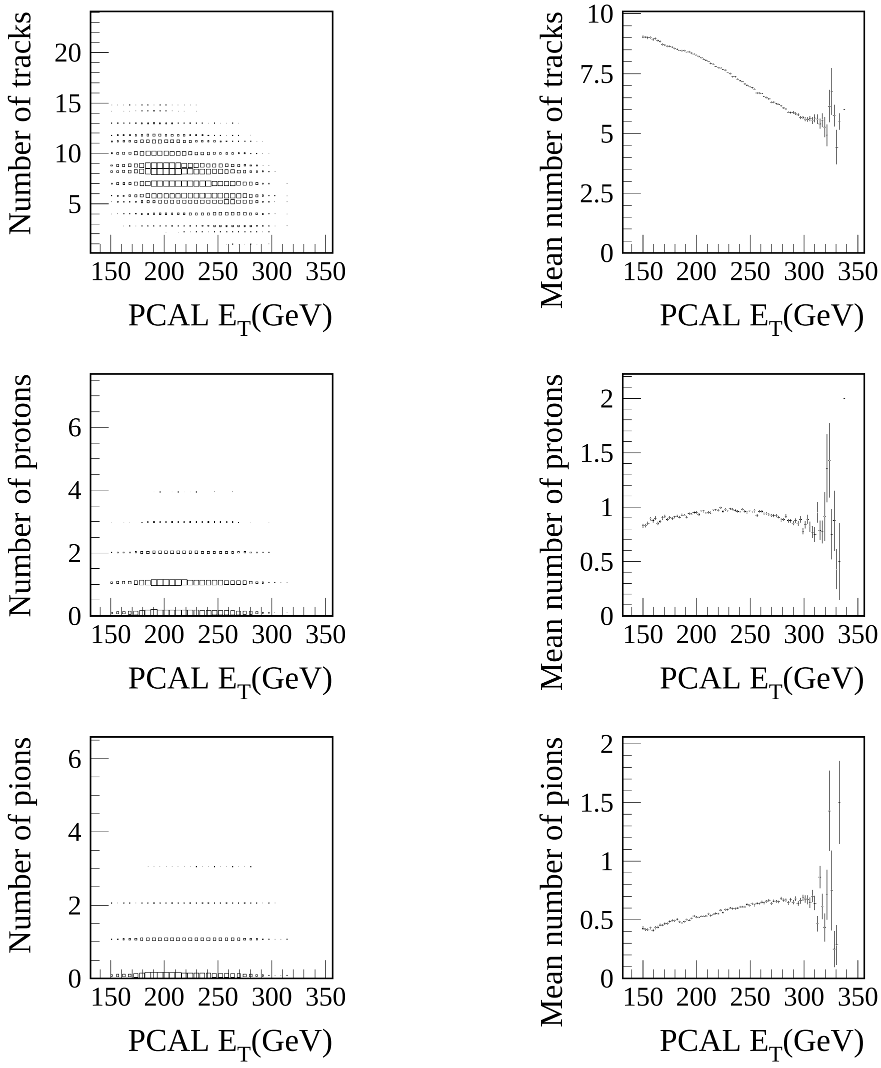

Figure D.3: The dependence of number of tracks, identified protons and pions, on the centrality (PCAL E_T).

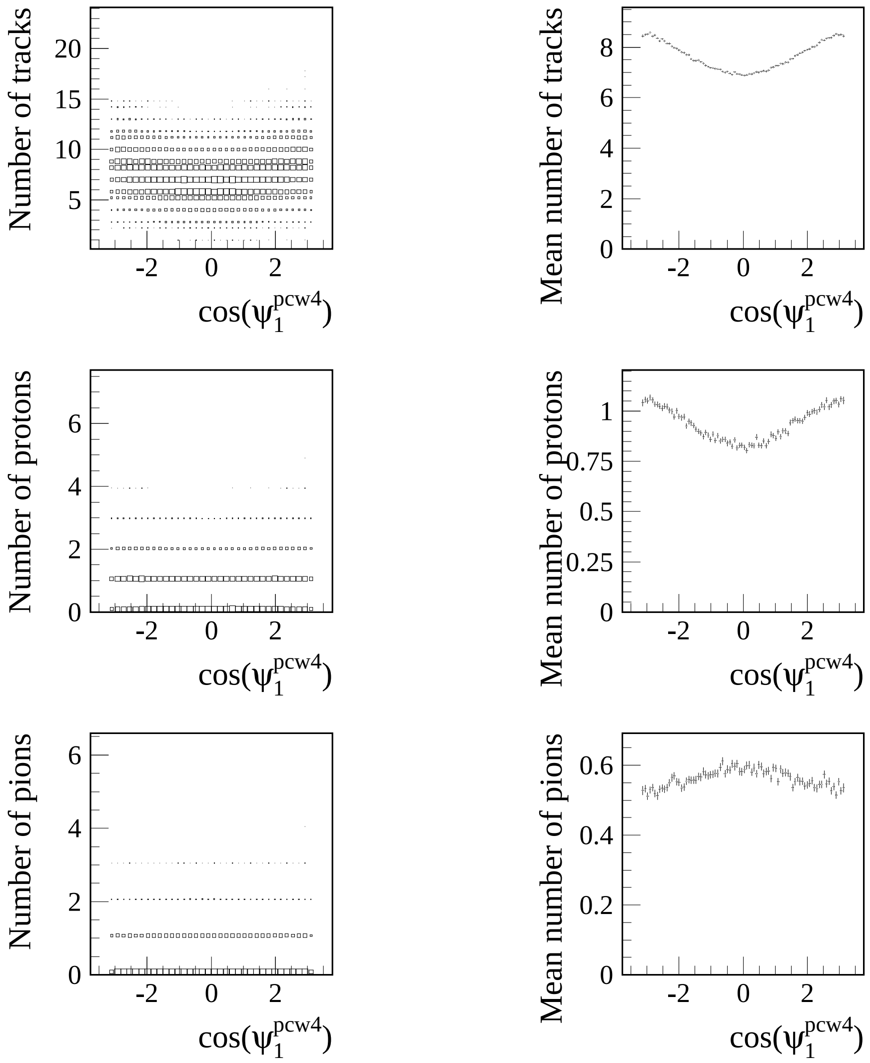

Figure D.4: The dependence of number of tracks, identified protons and pions, on the reaction plane orientation (Ψ_1^{PCW4}). When $\Psi_1^{\mathrm{PCW4}} = \pi$, the reaction plane points into the acceptance of the spectrometer.

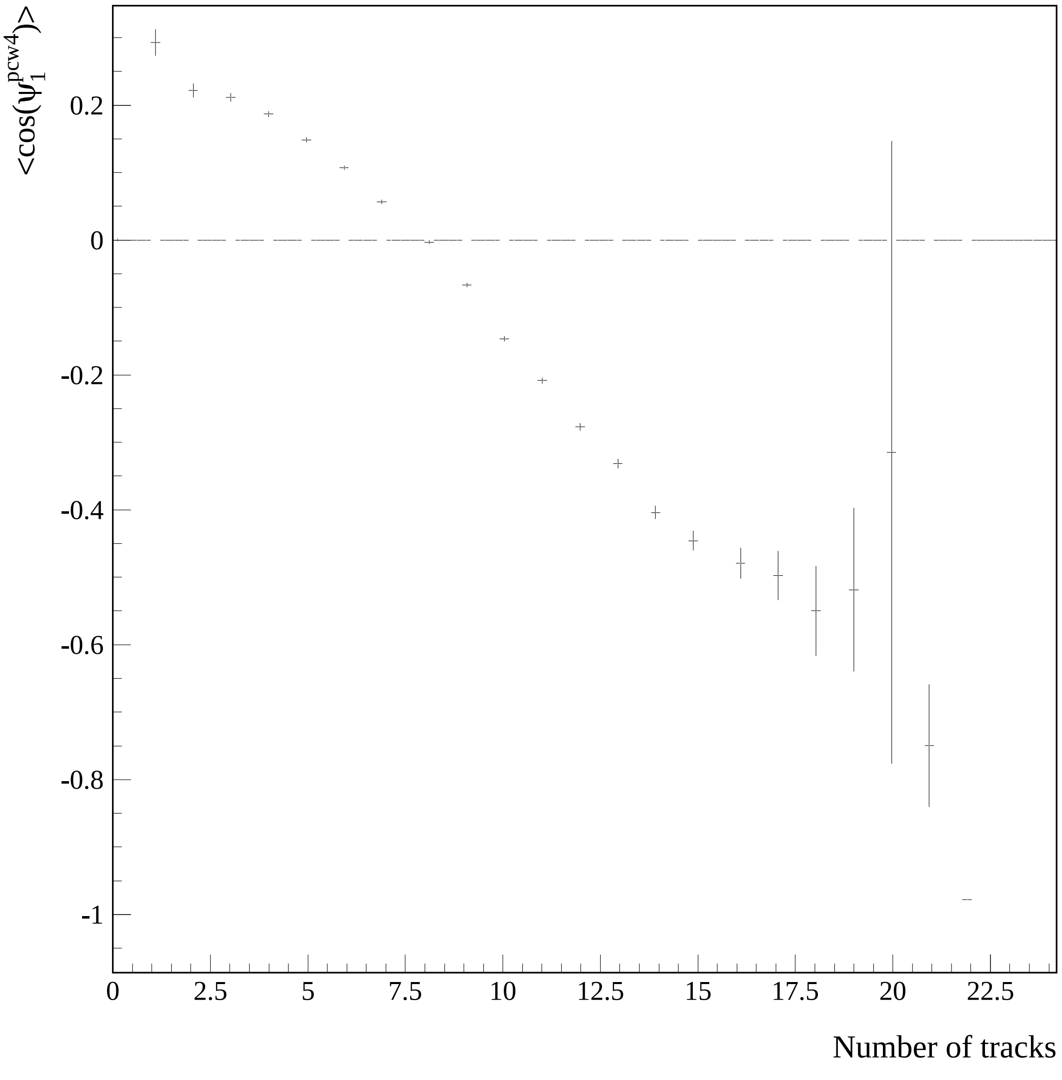

Figure D.5: The $\cos(\Psi_1^{PCW4})$ as a function of number of tracks. That the last few points on the high multiplicity tail are off the linear extrapolation signifies the inefficiency in the tracking in the high multiplicities when the reaction plane points into the acceptance of the spectrometer.

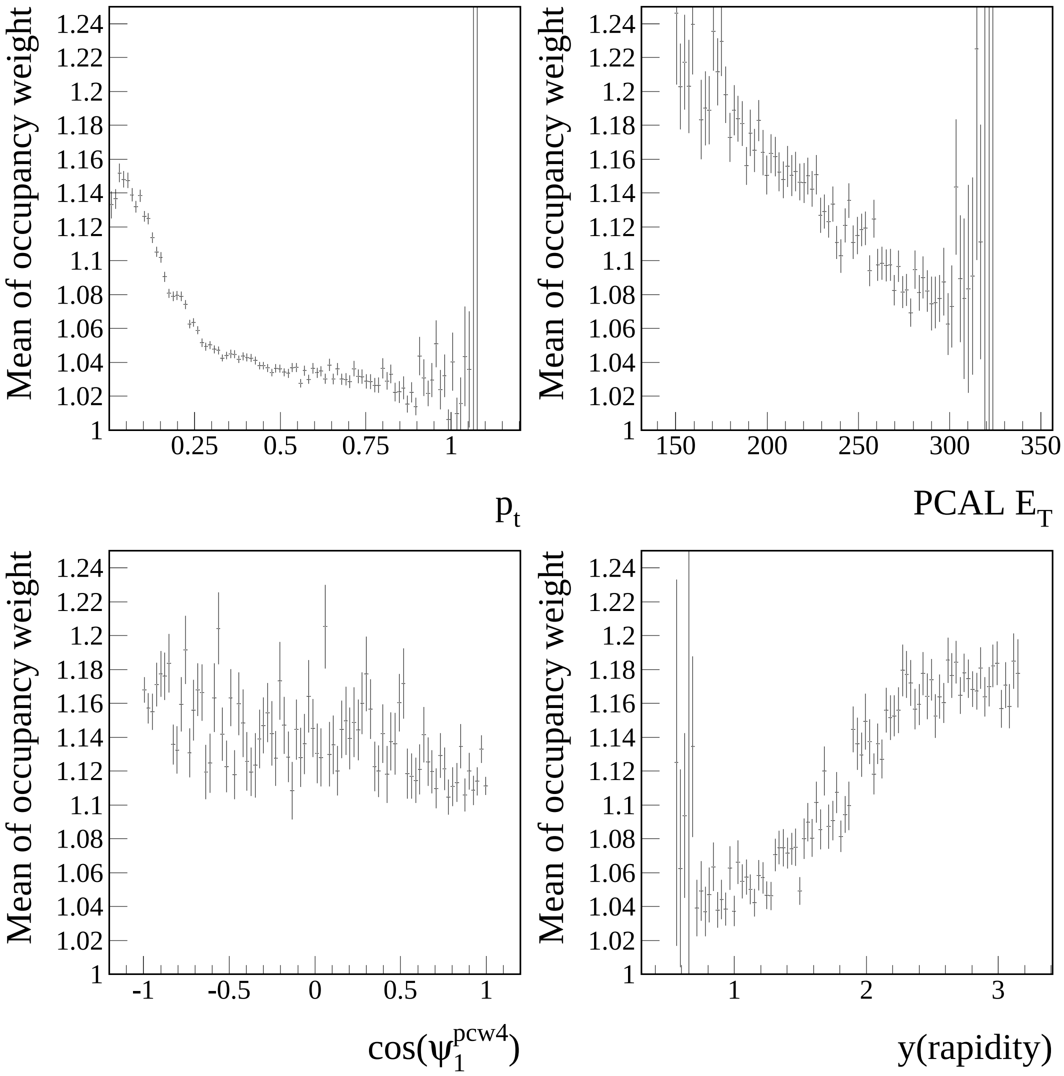

Figure D.6: The dependence of the mean weight of identified protons due to occupancy on p_t, centrality (PCAL E_T), the reaction plane orientation (cos(PCW4)) and the particle rapidity.